



저작자표시-비영리-변경금지 2.0 대한민국

이용자는 아래의 조건을 따르는 경우에 한하여 자유롭게

- 이 저작물을 복제, 배포, 전송, 전시, 공연 및 방송할 수 있습니다.

다음과 같은 조건을 따라야 합니다:



저작자표시. 귀하는 원저작자를 표시하여야 합니다.



비영리. 귀하는 이 저작물을 영리 목적으로 이용할 수 없습니다.



변경금지. 귀하는 이 저작물을 개작, 변형 또는 가공할 수 없습니다.

- 귀하는, 이 저작물의 재이용이나 배포의 경우, 이 저작물에 적용된 이용허락조건을 명확하게 나타내어야 합니다.
- 저작권자로부터 별도의 허가를 받으면 이러한 조건들은 적용되지 않습니다.

저작권법에 따른 이용자의 권리는 위의 내용에 의하여 영향을 받지 않습니다.

이것은 [이용허락규약\(Legal Code\)](#)을 이해하기 쉽게 요약한 것입니다.

[Disclaimer](#)

공학박사학위논문

**고분자전해질형 연료전지 모델을 통한
기체확산층의 구조적 특성이 물 관리와
성능에 미치는 영향에 관한 연구**

**Study on the Effects of Structural Characteristics of
Gas Diffusion Layer on Water Management and Cell
Performance with PEM Fuel Cell Model**

2015 년 2 월

서울대학교 대학원

기계항공공학부

박 재 만

고분자 전해질형 연료전지 모델을 통한 기체 확산층의 구조적 특성이 물 관리와 성능에 미치는 영향에 관한 연구

Study on the Effects of Structural Characteristics of Gas Diffusion Layer on Water Management and Cell Performance with PEM Fuel Cell Model

지도교수 민 경 덕

이 논문을 공학박사 학위논문으로 제출함

2014년 10월

서울대학교 대학원

기계항공공학부

박 재 만

박재만의 공학박사 학위논문을 인준함

2014년 12월

위원장 김 민 수 (인)

부위원장 민 경 덕 (인)

위 원 차 석 원 (인)

위 원 송 한 호 (인)

위 원 이 은 숙 (인)

To my parents

Abstract

Study on the Effects of Structural Characteristics of Gas Diffusion Layer on Water Management and Cell Performance with PEM Fuel Cell Model

Jaeman Park

Department of Mechanical and Aerospace Engineering
The Graduate School
Seoul National University

The gas diffusion layer (GDL) is a key component of a proton exchange membrane (PEM) fuel cell due to its role as a path for fuel, air, and water. Since the GDL determines the mass balance in the PEM fuel cell, investigation of the optimal structural characteristics of the GDL with improved water management is important for the quality performance of the PEM fuel cell. Many attempts to understand the structural characteristics of the GDL have been reported in both experimental and numerical studies. However, the previous studies have not explained how the structural characteristics of the GDL directly affect the PEM fuel cell performance. In this study, a PEM fuel cell model, which models the structural characteristics, is developed and the various the GDL structural characteristics are analyzed and validated.

Initially in this study, a dynamic, non-isothermal, and quasi-three-dimensional PEM fuel cell model that models the structural characteristic of the GDL is developed. The model is implemented using the MATLAB[®]/Simulink[®] interface. The model has merits of a simplified structure with the possibility of capturing local characteristics. To investigate the structural effects of the GDL, control volumes are discretized into

nine control volumes and two-phase mass transport is assumed. The model predicts liquid water transport and species diffusion throughout the GDL and the effects on water management and fuel cell performance.

Secondly, the effects of pore size variation in the substrate of the GDL on water management and cell performance are investigated. Two GDL samples with different pore sizes are evaluated by the porosity, pore size, thickness, and internal contact angle so as to understand the basic structural characteristic of the GDL. The GDL structural parameters are incorporated with the basic characteristics into the developed model. Cell performance is predicted relative to the two-phase mass transport inside the GDL. It is found that the large macro-pores in the substrate formed the MPL penetration and MPL part coarsely, while, the small macro-pores in the substrate formed MPL penetration and MPL part densely. The water management capability of the GDL varies with these differences with respect to water retention and removal characteristics. The cell performance is also affected by the operating conditions of relative humidity and current load.

Thirdly, the in-plane structural effects of the GDL on water management and cell performance are investigated. The basic concept of in-plane structure design of the GDL is a combination of two the different types of gas diffusion layers (GDL's), which have either water retention or removal capability. Four combinations of GDL structures are simulated and analyzed. It is shown that the combined GDL's have different local water management capability, and affect the uniformity of mass transport throughout the cell. In particular, the improved variation of mass transport throughout the cell resulted in a uniform current density distribution in the cell. Consequent experimental results verify that the combined GDL exhibits enhanced cell performance as well as improved voltage instability.

Finally, the effects of through-plane structure design of the GDL are studied. Once the liquid water is transferred from the MPL penetration to the substrate, the liquid water transports to the channel with an averaged capillary pressure gradient of the substrate. To enhance the liquid water transport in the substrate, the capillary pressure gradient should be increased continuously from the adjacent MPL penetration to the

channel. By simulation, it is observed that the continuously increased pore size in the control volumes of the substrate increased the capillary pressure gradient, and improved water management capability. Based on the concept, a GDL with a pore size gradient structure is fabricated, and is validated by experimental work. The experimental results show that the pore size gradient structure has improved mass transport at the high current load region.

This research includes both experimental and simulation investigation on various structural characteristics of the GDL and its effects on water management and fuel cell performance. The measured properties of the GDL are incorporated in the model and the model predicts the effects of the variations in the GDL structure, and those effects are then verified by the experimental work. Through the interaction between experimental and simulation work, it is possible to understand the effects of the GDL structure on mass transport behavior, and to suggest the ideal GDL structure.

Keywords: Proton exchange membrane (PEM) fuel cell, Gas diffusion layer (GDL), Simulation, Water management, Liquid water saturation, Structural characteristics

Student Number: 2009-20682

Contents

Abstract	vii
List of Figures	xv
List of Tables	xx
Nomenclature	xxi
Chapter 1. Introduction	1
1.1 Background and Motivation	1
1.1.1 Polymer electrolyte membrane fuel cell.....	1
1.1.2 Gas diffusion layer	2
1.1.3 Major issues in the gas diffusion layer.....	3
1.2 Literature Review	9
1.2.1 Design of structural characteristics of the GDL.....	9
1.2.2 Studies on GDL characteristics	10
1.2.2.1 Experimental studies	11
1.2.2.2 Numerical studies.....	15
1.3 Objectives	19
Chapter 2. Model descriptions and Experimental setup	22
2.1 Model descriptions	22

2.1.1 Assumptions	23
2.1.2 Discretization	23
2.1.3 Conservation equations	24
2.1.3.1 Energy conservation	24
2.1.3.2 Species conservation	26
2.1.4 Heat transfer	27
2.1.5 Species mass transport and Reaction rates	28
2.1.6 Water transport between the GDL and MEA	29
2.1.7 Liquid water transport	31
2.1.8 Electrochemical model	33
2.1.9 Pressure drop	35
2.2 Experimental setup	41
2.2.1 Fuel cell and test station	41
2.2.2 Experimental condition	41
2.2.3 Water permeability test	42
2.2.4 Surface contact angle measurement	43
2.2.5 Mercury Porosimetry	43
2.2.6 Scanning electron microscope (SEM)	43
Chapter 3. Effect of the pore size variation in the substrate on water management and cell performance	49
3.1 Structural parameters of the GDL	49
3.2 Design of the GDL	51
3.3 Experimental results	53
3.3.1 Analysis with scanning electron microscope	53
3.3.2 Analysis with porosimetry	54
3.3.3 Analysis with water permeability and surface contact angle measurement	56

3.3.4 Analysis with steady-state performance	58
3.3.5 Analysis with transient response of voltage	59
3.4 Simulation results.....	74
3.4.1 Validation	74
3.4.2 Analysis with simulation results.....	74
Chapter 4. Effect of in-plane structure design of the GDL on water management and cell performance	88
4.1 Design of the GDL.....	90
4.2 Analysis with simulation results.....	92
4.3 Verification of the effect of in-plane structure design with experimental results ...	104
Chapter 5. Effect of through-plane structure design of the GDL on water management and cell performance	112
5.1 Design of the GDL.....	114
5.2 Analysis with simulation results.....	117
5.3 Verification of the effect of through-plane structure design with experimental results	125
5.3.1 Analysis with scanning electron microscope.....	125
5.3.2 Analysis with porosimetry.....	126
5.3.3 Steady-state performance	127
5.3.4 Transient voltage response	127
5.4 Suggestion of the ideal GDL structure design.....	135

Chapter 6. Conclusions	141
Bibliography	144
국 문 초 록.....	155

List of Figures

Figure 1.1 Forecast of the future market sales of vehicles [4]	5
Figure 1.2 A schematic diagram of the PEM fuel cell in the cross-sectional direction [5]	6
Figure 1.3 A schematic diagram of the GDL structure.....	7
Figure 1.4 Trade-off relationship between water removal and retention abilities of the GDL [12]	8
Figure 1.5 Methodology of the study	21
Figure 2.1 Schematic diagram of one-dimensional model with cross-sectional direction.....	36
Figure 2.2 Schematic diagram of the GDL control volumes.....	37
Figure 2.3 Illustration of the stream-wise and the cross-sectional discretization of a PEM fuel cell (not drawn to scale).....	38
Figure 2.4 Experimental apparatus for testing the 25 cm ² PEM fuel cell	45
Figure 2.5 Experimental apparatus for measuring water permeability of the GDL..	46
Figure 2.6 Experimental process for measuring surface contact angle of the GDL..	47
Figure 2.7 Mercury porosimetry	48
Figure 3.1 Surface SEM images of S8L2 and S2L8	62
Figure 3.2 Cross-sectional images of S8L2 and S2L8: (a) S8L2 and (b) S2L8	63

Figure 3.3 Schematic diagram cross-sectional structure of the GDL.....	64
Figure 3.4 Pore size distribution of S8L2 and S2L8	65
Figure 3.5 Pore size distribution of substrate only sample of S8L2 and S2L8	66
Figure 3.6 Steady-state performance of the S8L2 and S2L8: (a) at RH 100%, (b) at 50%, and (c) at 30%	67
Figure 3.7 Comparison of steady-state performance of S8L2 and S2L8 at various humidification: (a) S8L2 and (b) S2L8	68
Figure 3.8 Comparison of standard deviation of voltage of S8L2 and S2L8: (a) at RH 100%, (b) at RH 50%, and (c) at RH 30%	69
Figure 3.9 Comparison of transient response of S8L2 and S2L8: (a) at RH 100%, (b) at RH 50%, and (c) at RH 30%	70
Figure 3.10 Validation of simulation results of S8L2 and S2L8: (a) at RH 100% and (b) RH 50%	79
Figure 3.11 Overvoltages of S8L2 and S2L8: (a) at RH 100% and (b) at RH 50% ..	80
Figure 3.12 Liquid water saturation along the GDL thickness of S8L2 and S2L8 at 1.6 A/cm ² : (a) at RH 100% and (b) at RH 50%	81
Figure 3.13 Oxygen concentration of S8L2 and S2L8 along the GDL thickness	82
Figure 3.14 Oxygen concentration of S8L2 and S2L8 according to current density	83
Figure 3.15 Distribution of oxygen mole fraction of S8L2 and S2L8 at RH 100%: (a) S8L2 and (b) S2L8.....	84

Figure 3.16 Water concentration of S8L2 and S2L8 along the anode GDL, MEA, and cathode GDL.....	85
Figure 3.17 Distribution of membrane water content of S8L2 and S2L8 at RH 50%: (a) S8L2 an (b) S2L8.....	86
Figure 3.18 Capillary pressure gradient of S8L2 and S2L8 along the substrate at RH 100%.....	87
Figure 4.1 Design of four combinations of the GDL: (a) 1-4 of S8L2 20% and S2L8 80%, (b) 2-3 of S8L2 40% and S2L8 60%, (c) 3-2 of S8L2 60% and S2L8 40%, and (d) 4-1 of S8L2 80% and S2L8 20%	91
Figure 4.2 Voltage and overvoltages of combinations of the GDL at 1.6 A/cm ² : (a) at RH 100% and (b) at RH 50%	97
Figure 4.3 Liquid water saturation of combinations of the GDL at 1.6 A/cm ² : (a) at RH 100% and (b) at RH 50%	98
Figure 4.4 Distributions of membrane water content at RH 50%: (a) combinations of 1-4, (b) combinations of 2-3, (c) combinations of 3-2, and (d) combinations of 4-1	99
Figure 4.5 Distributions of oxygen mole fraction at RH 100%: (a) combinations of 1-4, (b) combinations of 2-3, (c) combinations of 3-2, and (d) combinations of 4-1	100
Figure 4.6 Distributions of current density at RH 50%: (a) combinations of 1-4, (b) combinations of 2-3, (c) combinations of 3-2, and (d) combinations of 4- 1	101

Figure 4.7 Distributions of current density at RH 100%: (a) combinations of 1-4, (b) combinations of 2-3, (c) combinations of 3-2, and (d) combinations of 4-1	102
Figure 4.8 Standard deviation of current density distribution of combinations of the GDL.....	103
Figure 4.9 Experimental setup of combination of 2-3.....	107
Figure 4.10 Steady-state performance of 2-3 and validation of simulation results .	108
Figure 4.11 Comparison of steady-state performance of S8L2, S2L8, and 2-3: (a) at RH 100%, (b) at RH 50%, and (c) at RH 30%	109
Figure 4.12 Comparison of standard deviation of voltage of S8L2, S2L8, and 2-3: (a) at RH 100%, (b) at RH 50%, and (c) at RH 30%.....	110
Figure 4.13 Comparison of transient response of S8L2, S2L8, and 2-3: (a) at RH 100%, (b) at RH 50%, and (c) at RH 30%	111
Figure 5.1 Design concept of the PG.....	115
Figure 5.2 Steady-state performance and validation of NPG, and simulation results of PG: (a) at RH 100% and (b) RH 50%	119
Figure 5.3 Overvoltages of PG and NPG: (a) at RH 100% and (b) at RH 50%.....	120
Figure 5.4 Liquid water saturation along the GDL thickness of PG and NPG at 1.6 A/cm ² : (a) at RH 100% and (b) at RH 50%	121
Figure 5.5 Capillary pressure gradient of PG and NPG along the substrate at RH 100%.....	122
Figure 5.6 Oxygen concentration of PG and NPG along the GDL thickness	123

Figure 5.7 Oxygen concentration of PG and NPG according to current density	124
Figure 5.8 Surface images of PG and NPG: (a) NPG, (b) small macro-pores of PG near the MPL, and (c) large macro-pores of PG near the channel	129
Figure 5.9 Surface image of PG and NPG: (a) PG and (b) NPG	130
Figure 5.10 Pore size distribution of PG and NPG	131
Figure 5.11 Steady-state performance of the PG and NPG: (a) at RH 100% and (b) at 50%	132
Figure 5.12 Standard deviation of voltage of PG and NPG: (a) at RH 100% and (b) at RH 50%	133
Figure 5.13 Transient response of PG and NPG: (a) at RH 100% and (b) at RH 50%	134
Figure 5.14 Illustration of the concept of the ideal GDL structure	137
Figure 5.15 Voltage and overvoltages at 1.6 A/cm ² according to GDL structure design: (a) at RH 100% and (b) at RH 50%	138
Figure 5.16 Liquid water saturation of the ideal GDL and 2-3 combination at 1.6 A/cm ² : (a) at RH 100% and (b) at RH 50%	139
Figure 5.17 Standard deviation of current density distribution of combinations of GDL.....	140

List of Tables

Table 2.1 Geometric PEM fuel cell model parameter values	39
Table 2.2 General PEM fuel cell model parameter value	40
Table 3.1 Basic GDL characteristics of S8L2 and S2L8	52
Table 3.2 Thickness of each the GDL part of S8L2 and S2L8	71
Table 3.3 Porosity and local porosities of S8L2 and S2L8	72
Table 3.4 Contact angles of S8L2 and S2L8	73
Table 5.1 Structural parameters of the GDL: PG and NPG.....	116

Nomenclature

a	water activity [-]
A	surface area [m ²]
C	solid specific heat capacity [kJ kg ⁻¹ K ⁻¹]
\bar{C}	species molar concentration (H ₂ , H ₂ O, N ₂ , O ₂) [kmol m ⁻³]
C_V	gas constant-volume specific heat capacity [kJ kg ⁻¹ K ⁻¹]
d_p	diameter of pore [m]
\bar{D}	diffusion coefficient [m ² s ⁻¹]
D_H	hydraulic diameter [m]
E_a	activation energy [kJ kmol ⁻¹]
F	Faraday's constant [96,485 C mol ⁻¹]
f	friction factor [-]
\bar{g}_m	mass transport coefficient [m s ⁻¹]
g	gravitational acceleration [m s ⁻²]
h	enthalpy [kJ kmol ⁻¹], convective heat transfer coefficient [kW m ⁻² K ⁻¹]
h_f	head loss [-]
ΔH	enthalpy of formation [kJ mol ⁻¹]
i_0	exchange current density [A m ⁻²]
I	electrical current [A]
$\bar{j}^{(l)}$	mass flux of liquid phase [kg m ⁻² s ⁻¹]
k_r	relative permeability [-]
K	permeability [m ²]
k_f	fluid conduction heat transfer coefficient [kW m ⁻¹ K ⁻¹]
k_s	solid conduction heat transfer coefficient [kW m ⁻¹ K ⁻¹]
L	length [m]
n	number of participating electrons in the reaction [-]
n_d	osmotic drag coefficient [-]
N	total number of moles [kmol]

\dot{N}	molar flow rate [kmol s ⁻¹]
Nu_D	Nusselt number [-]
M_m	membrane dry equivalent weight [kg kmol ⁻¹]
P	pressure [kPa]
\dot{Q}	heat transfer [kW]
R	fuel cell external/load resistance [Ω]
Re	Reynolds number [-]
\bar{R}	species reaction rate (H ₂ , H ₂ O, N ₂ , O ₂) [kmol s ⁻¹]
\bar{R}_{dif}	diffusion resistance [m ³ s ⁻¹]
s	liquid water saturation [-]
Sh	Sherwood number [-]
t	time [s], thickness [m]
T	temperature [K]
V	voltage [V]
v	fluid velocity [m s ⁻¹]
Ψ	volume [m ³]
\bar{X}	species mole fraction (H ₂ , H ₂ O, N ₂ , O ₂) [-]

Greek letters

$\bar{\Phi}$	species diffusion flux between the GDL and bulk gases (H ₂ , H ₂ O, N ₂ , O ₂) [kmol s ⁻¹]
$\Theta_{\text{H}_2\text{O}}$	water osmotic flux through the MEA [kmol s ⁻¹]
$\Psi_{\text{H}_2\text{O}}$	water diffusion flux between the GDL and MEA [kmol s ⁻¹]
α	transfer coefficient [-]
ε	porosity of the GDL [-]
η	surface overpotential [V]
θ_c	contact angle [°]
κ	ionic conductivity [S m ⁻¹]
λ	membrane hydration [-]
$\lambda^{(k)}$	mobility of phase k [-]
ν	kinematic viscosity [m ² s ⁻¹]

ρ	density [kg m^{-3}]
σ	electrode conductivity [S m^{-1}]
τ	surface tension [N m^{-1}]

Superscripts and subscripts

act	activation polarization
c	capillary
GDL	gas diffusion layer
g	bulk gas control volume; gas phase
in	Into control volume
k	liquid or gas phase
l	liquid phase
m	membrane
MEA	membrane electrode assembly
ohm	ohmic polarization
out	out of control volume
ref	reference condition
s	solid control volume
sat	water saturation
w	water
0	standard condition

Acronym

AFC	alkaline fuel cell
APS	air process system
BOP	balance of plant
CCD	charge-coupled device
FPS	fuel process system
GDL	gas diffusion layer
LBM	lattice Boltzmann model

LPM	liter per minute
MCFC	molten carbonate fuel cell
MEA	membrane electrode assembly
MPL	micro porous layer
NPG	non-pore size gradient
ODE	ordinary differential equation
PAFC	phosphoric acid fuel cell
PEM	proton exchange membrane or polymer electrolyte membrane
PG	pore size gradient
PNM	pore network model
PTFE	poly-tetrafluoroethylene
RH	relative humidity
SEM	scanning electronic microscope
SOFC	solid oxide fuel cell
TWMS	thermal & water management system

Chapter 1. Introduction

1.1 Background and Motivation

1.1.1 Polymer electrolyte membrane fuel cell

The modern world depends on the use of fossil fuels: air pollution problems including global warming and climate change, and the fossil fuel depletion are not to be overlooked. There are many alternative, renewable energy technologies to overcome the situation. Especially, fuel cells are drawing attention in transportation and stationary applications because of their high-efficiency and the absence of pollutants, such as; CO₂, NO_x, SO_x, and particulate emissions [1].

Fuel cells can be classified by their electrolyte; phosphoric acid fuel cell (PAFC), polymer electrolyte membrane (PEM) fuel cell, alkaline fuel cell (AFC), molten carbonate fuel cell (MCFC) and solid-oxide fuel cell (SOFC). Due to different mechanisms of ionic conduction, the operating temperature and catalyst type of each fuel cells are different [2].

The PEM fuel cell uses polymer membrane as an electrolyte, and has an operating temperature under 80 °C. PEM fuel cells, due to their; low operating temperature, high power density, quiet operation, rapid start-up and shut down, high efficiency, and low emissions, are regarded as a promising clean energy source for eco-friendly vehicles [3]. Motivated by such advances in fuel cell technology, increasingly, more automakers have researched and developed fuel cell vehicles since 2000. To commercialize the fuel cell vehicles, presently, the infrastructure of the hydrogen fueling system, the durability of PEM fuel cell, and the cost-down of the cell stack

must all be improved. If current trends maintain, the market penetration of fuel cell vehicles is expected to increase continuously and the worldwide market share will achieve 90% of all vehicle sales by 2040, as shown in Figure 1.1 [4].

The polymer electrolyte membrane (Nafion[®]) requires a highly hydrated state for the conduction of protons to be effective, thus, external humidification of the reactants is necessary for the effective operation of a PEM fuel cell. As shown in Figure 1.2, there are catalyst layers on both sides of the membrane. The electrochemical reaction occurs at the cathode catalyst layer with protons transferred from anode side and oxygen ions. The reactant gases and the product water are all transported through the gas diffusion layer (GDL). The reactant gases, hydrogen and air, which are transported from the gas channel via convection, diffuse to the catalyst layer through the GDL. The product water is then transported to the channel via capillary force inside the GDL [5]. Consequently, the GDL is a medium of two-phase transport. To use the PEM fuel cell as a power source in vehicles, stack and balance of plant (BOP) systems, such as; air process (APS), fuel process (FPS), and thermal & water management (TWMS) systems, are required to operate a PEM fuel cell system optimally [6].

1.1.2 Gas diffusion layer

The GDL is the limiting element of a fuel cell system. It is located between the bipolar plate and the catalyst layer of MEA. The functions of the GDL are summarized as follows: (1) path of reactant gases and liquid water, (2) electric conductor, (3) thermal conductor, and (4) mechanical damper [7]. To enhance the liquid water removal capability, the GDL has hydrophobic characteristics by incorporation of polytetrafluoroethylene (PTFE). The GDL consists of two distinguished parts: substrate layer and micro porous layer (MPL), as shown in Figure 1.3. The substrate layer is

mainly composed of carbon fibers, and can be divided into three different manufacture types; carbon felt, carbon cloth, and carbon paper. Different arrangements of the carbon fiber produces different structural characteristics that affect passage and mass transport [8]. Generally, the pore size of the substrate layer is on the order of 5~100 μm . Since the pore size of substrate layer is about 1000 times greater than that of catalyst layer, an MPL used in the GDL to enhance both the electrical conductivity and capillary force between catalyst layer of MEA and the substrate layer of the GDL. The MPL is mainly composed of carbon powder with a pore size on the order of 0.1~1 μm [9]. Since the MPL cannot be existed in a single layer, when the MPL is coated on the substrate layer, some of carbon power penetrates through the substrate layer, and forms MPL penetration region. This region has characteristics intermediate to those of the MPL and substrate layers.

1.1.3 Major issues in the gas diffusion layer

Studies of the GDL are of interest due to appreciation of gas diffusion layers (GDL's) being the key component in the development of fuel cells over the past decade [10]. Recently, studies of GDL's have issues. One is optimal passage design of the GDL to enhance mass transport capability; another is the durability of the GDL.

Composed of perfluorosulfonated polymers and used in the typical PEM fuel cells with an operating temperature range of 50~80 $^{\circ}\text{C}$, the Nafion[®] membrane requires a highly hydrated state to conduct protons effectively. External humidification is required so as to maintain a high water content in the cell. Relevantly, high-load operating conditions produces relatively more water. When sufficient water vapor accumulates to exceed the saturated water vapor pressure, condensation can occur and a flooding phenomenon may occur [11]. To prevent the flooding

phenomenon, the GDL should maintain proper mass balance between water production and removal. Additionally relevant, because the external humidification causes additional power loss, the low humidification operation influences enhancement of the net efficiency of the system. For the low humidity operation, water retention in the GDL would counter membrane dehydration. The efficiency characteristics of the GDL have a trade-off relationship between water removal and retention, as shown in Figure 1.4 [12]. Studies on the optimal passage design of the GDL are required to determine how best to enhance water management by simultaneously adjusting water removal and retention.

Durability is another major issue in PEM fuel cell. The GDL plays a role as a mechanical damper, and buffers the degradation of other components. Unlike other PEM fuel cell components, such as MEA [13-15], few research studies on the GDL degradation and durability are available. Some researchers have investigated; the effect of the freeze/thaw conditions [16-22], carbon corrosion [23-27], and dissolution effect [28-30] on the GDL characteristics. Broadly, the durability of the GDL is shown to be susceptible to various degradation mechanisms and processes [8]. It is necessary to investigate the reasons for GDL degradation and its effects on the cell performance.

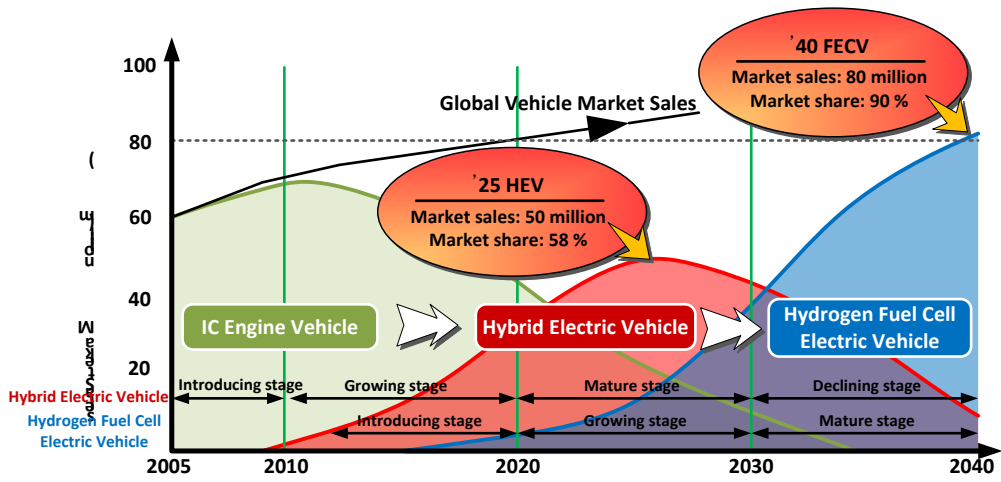


Figure 1.1 Forecast of the future market sales of vehicles [4]

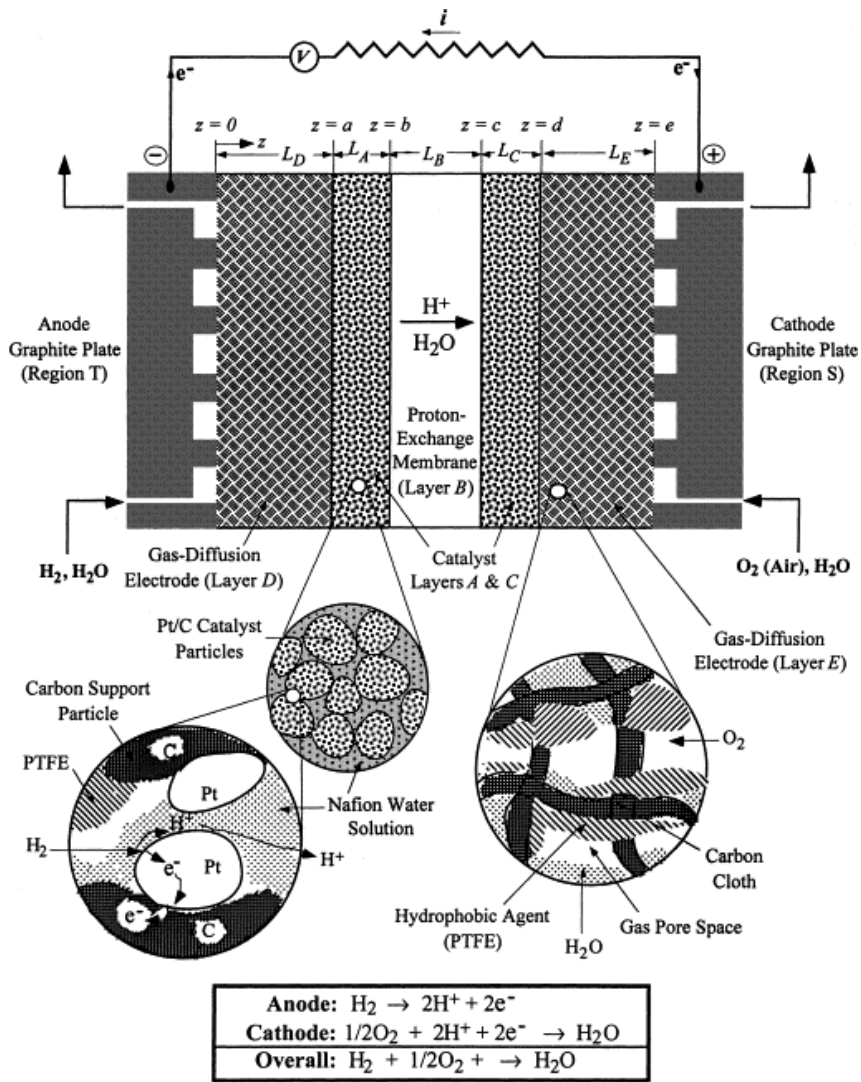


Figure 1.2 A schematic diagram of the PEM fuel cell in the cross-sectional direction

[5]

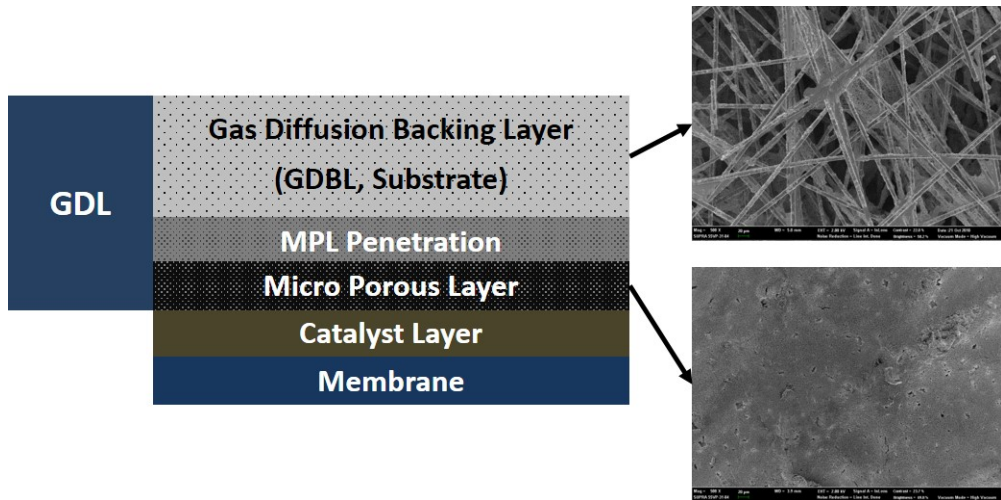


Figure 1.3 A schematic diagram of the GDL structure

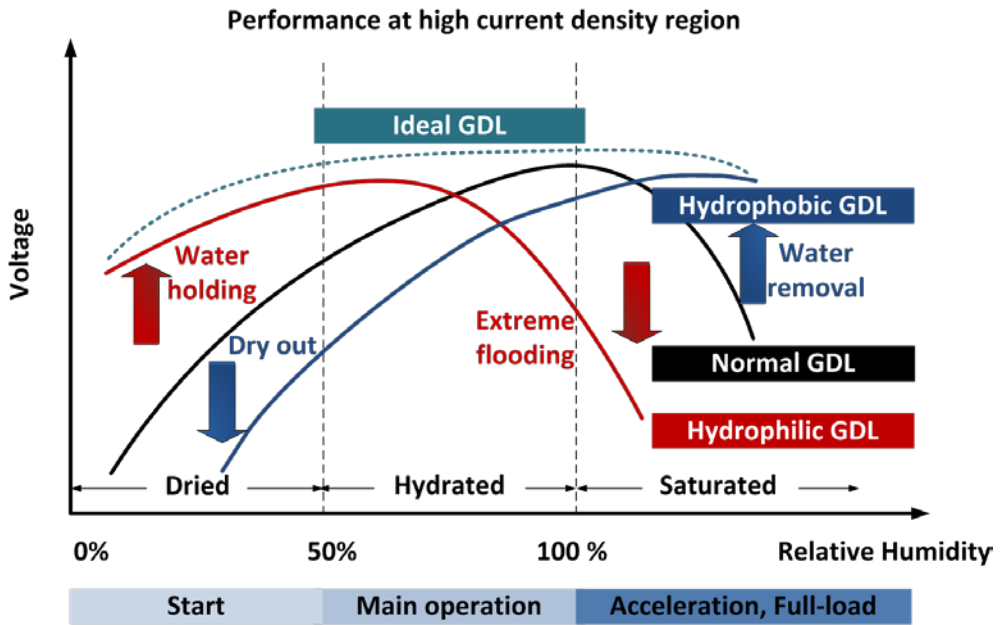


Figure 1.4 Trade-off relationship between water removal and retention abilities of the GDL [12]

1.2 Literature Review

1.2.1 Design of structural characteristics of the GDL

As discussed in the Background and Motivation section, the GDL is a critical component of the PEM fuel cell because it acts as a passage for the humidified reactants and products. Several attempts in the design of GDL structural characteristics so as to enhance the capability of mass transport have been reported. In the early stage, studies, which varied hydrophobicity of the GDL, are widely conducted to increase the liquid water removal capability [31-37]. As the substrate layer type affects transport in the GDL, investigation of the effect of the substrate layer type such as carbon cloth, felt, and paper are reported [38-40]. There have been attempts to design the passage of the GDL in an active way but most attempts have focused on MPL design because altering MPL characteristics is simpler than altering substrate characteristics. Several studies investigated the multiple-layered MPL design. Tang et al. [41] developed a triple layered MPL with pore-former. The porosity of the MPL is increased toward the channel with the amount of pore-former. Weng et al. [42] designed a triple-layered MPL that has a hydrophobicity gradient structure. Chun et al. [43] developed a comparative hydrophobic-hydrophilic double-layered MPL that has decreasing hydrophobicity from the catalyst layer to the channel. Cho et al. [44] changed the density of MPL slurries, and developed a double-layered MPL incorporating MPL slurries of different density, which found that increasing density from the catalyst layer to channel direction enhanced transport in both RH 50% and 100% conditions. Chun et al. [9] and Manahan et al. [45] have shown that the pore-size distribution of the MPL can be controlled by pore-former and laser perforation, respectively. Cho et al. [46] controlled the MPL penetration thickness, and found that

a thick MPL penetration has a balanced capillary pressure gradient through the GDL. In contrast, attempts to design the structural characteristics of the substrate layer have rarely been reported in the literature. Zhang et al. [47] developed a metallic GDL that controls porosity. The major difference between it and conventional GDL's is that it has not randomly formed pore structure but straight pores. Furthermore, Cho et al. [48] introduced the activated carbon fibers, and controlled the pore size distribution of the substrate layer. They have developed GDL's with either small macro-pores or large macro-pores, and investigated the water balance inside these GDL's.

However, these studies do not functionally correlate GDL characteristics with mass transport behavior and PEM fuel cell performance: a qualitative hypothesis is found necessary to explain the effect of GDL characteristics on the PEM fuel cell performance. Quantitative elucidation of mass transport characteristics as well as the PEM fuel cell performance are desirable because GDL characteristics, such as; porosity, pore size, contact angle, and thickness all critically affect the two-phase mass transport inside the GDL. Notably, the capillary pressure gradient, which is a driving force of the liquid water inside the GDL, and the diffusion coefficient, correlated to liquid water saturation of each GDL partition, need be analyzed to evaluate the active passage design of the GDL.

1.2.2 Studies on GDL characteristics

Thus far, many quantitative studies on GDL characteristics have been reported. There are mainly two methods to investigate GDL characteristics such as liquid water saturation, broadly; experimental and numerical studies. The experimental studies have focused on liquid water visualization. The most important issue in the experimental study of liquid water visualization is that it is possible to measure the

liquid water distribution in operating PEM fuel cell, in-situ. There are several ways to visualize the liquid water inside a cell. In this part, representative techniques will be introduced; neutron imaging, synchrotron X-ray, and optical photography. In numerical studies, there are two representative methods -pore-network model and lattice Boltzmann model- that are appropriate to investigate the micro scale liquid water behavior inside a GDL.

1.2.2.1 Experimental studies

The principle of neutron imaging is to measure signal attenuation in neutron beam irradiation. Since the attenuation coefficients of fuel cell components, such as; aluminum, graphite, and gold, are much smaller than those of hydrogen and hydrogen containing compounds, so, liquid water accumulation inside the GDL can be well visualized and quantified.

Pekula et al. [49] pioneered neutron imaging for visualization of liquid water in operating fuel cell conditions. Liquid water is found to tend to accumulate as a function of operating conditions and at 90° bends in the gas flow channels, especially. Kramer et al. [50] conducted in-situ neutron imaging measurement to characterize the two-phase mass transport. Neutron radiography is so used to quantify liquid water accumulation inside an operating the PEM fuel cell, and to investigate the effect of channel geometries on flow characteristics and water management. In the study, two channel geometries are used: interdigitated and parallel serpentine flow fields. The results show that serpentine flow field is more advantageous for transportation of liquid water, and it is discovered that liquid accumulation increased as current density and inlet dew-point increased. It is possible to investigate the distribution of water accumulation through in-plane direction. However, they could not quantify the amount of water accumulated through each GDL partitions with through-plane

direction. Additionally, the same research group [51] conducted a neutron imaging study of GDL's with differing composition. As a result, the cloth type GDL shows considerable less liquid inside the GDL compared to the paper type GDL. However, the relation between differences in performance and liquid contents is not elucidated. Kowal et al. [52] analyzed liquid water distribution with neutron imaging with varying humidity, current densities, and flow rates for both the cloth and paper GDL's. Water accumulation is found to tend to accumulate under the lands about 15% more than in the channel locations, in the GDL. Additionally, the results showed that the paper GDL contains 174% more water per volume under the land, compared to the cloth GDL's. Trabold et al. and Owejan et al. [53, 54] measured the water transport through the GDL with an interdigitated and serpentine flow fields by neutron radiography. Notably, Owejan et al. [54] found in case of an interdigitated flow field, the GDL is possible to contain liquid water up to 44.2% of the available void volume with excess reaction water removed from the cell at its production rate. Turhan et al. [55, 56] conducted the neutron imaging experiments that visualized the amount of cumulated liquid water in the channels and the GDL. Among several findings, it is observed that liquid water easily accumulated under the lands due to higher heat transfer and restricted mass transfer. In a recent paper, the same group [56] employed neutron imaging to seven different flow-field designs to study the effect of different landing-to-channel ratios on water management. It is concluded that the optimal L:C ratio is smaller than 2:3 and that a high L:C ratio is advantageous for dry operating condition, while, a low L:C is advantageous for high humidity operating condition. Hickner et al. [57] used high-resolution neutron radiography to observe the liquid water accumulation profile through the cross-section. The analyzed liquid water profile is dominantly affected by current density and temperature gradient due to local heating at the MEA. Notably, the water content in the MEA is maintained almost constantly between the current density range of 0.25 and 1.25 A/cm², even though the liquid

water accumulation at the gas flow channel changed drastically according to current densities.

X-ray radiography is used to measure the through-plane water content via variation of the intensity of the X-ray beam signal after it transmitted through the material. Since the X-ray radiography has high spatial and temporal resolutions, it is a promising technology to investigate the liquid water transport through the GDL.

Sinha et al. [58] conducted X-ray microtomography studies to quantify the liquid water saturation in the GDL. The results showed that the accumulated liquid water is drastically reduced with purge time, but after a limiting purge time, there is no further significant liquid water removal. Manke et al. [59] investigated the mechanism of liquid water formation with synchrotron x-ray radiography. They found that the accumulated liquid water is located under ribs and so moves to the channel wall. When the liquid water under ribs erupted through the boundary between rib and channel, the emptied pores would refill slowly, and again erupt. Another study by the same group [59] investigates liquid water accumulation in the cross-sectional direction. The conclusion is that liquid water accumulation is strongly related to the current density and also dependent upon the hydrophobic/hydrophilic characteristics of the GDL. Mukaide et al. [60] observed water distribution in both in-plane and cross-sectional directions in an operating PEM fuel cell, using synchrotron X-ray imaging. A GDL with a pinhole array perpendicular to the GDL indicated water flow into the pinhole pores, due to its low surface energy, indicating that the water flow in the GDL is affected by GDL characteristics, such as, hydrophobic/hydrophilic properties and pore radius.

Optical photography, which has high temporal and spatial resolution, uses transparent cells to investigate the liquid water transport with the advantage of this

window for observation of water transport within an operating fuel cell. However, the transparent materials of an optical cell are not usually used in PEM fuel cell construction [52] and high temporal resolution is required to capture the dynamic behavior of liquid water transport.

Tuber et al. [61] studied two-phase mass transport in the cathode via a transparent PEM fuel cell. They varied operating conditions such as stoichiometry, operating temperature, and ambient humidity. Especially, they found that hydrophilic GDL's show advantageous performance at the near operating condition of 30 °C, which can occur under start conditions. Yang and Zhang of the same research group [62, 63] investigated liquid water transport and removal from the GDL and gas channel, using a transparent cell. Liquid water removal is found to be affected by flow patterns and the shear force by the gas flow in the channel, limited by the liquid water droplet growth on the hydrophilic channel walls. Ge and Wang [64] conducted transparent PEM fuel cell studies to visualize water transport on the anode side, and observed the effect of the GDL wettability on water distribution in the anode. Notably, at a low current density of 0.2 A/cm², the hydrophobic GDL is disadvantageous because water tends to accumulate on the channel surfaces rather than inside the GDL so as to produce in channel clogging. Spornjak et al. [65] conducted experimental visualization of liquid water formation and transport using transparent serpentine PEM fuel cells while varying the GDL composition. It is found that in a GDL with an untreated water-proof function there is liquid water blockage of the pore, such that the gas and water transport toward the membrane is restricted, resulting in poor cell performance. Kimball et al. [66] observed how liquid water transport via the GDL and initiates at the GDL/channel interface with cloth and paper type of GDL's. It is concluded that water from the membrane/electrode interface is accumulated until it is possible to penetrate the GDL when the hydrostatic pressure exceeds the water/GDL

interfacial tension. Gao et al. [67] pioneered confocal microscopy to investigate liquid water behavior inside GDL's, studying various GDL types. Confocal microscopy can obtain different depths of focus, and is used to capture simultaneous three-dimensional imaging of the GDL fibers and liquid water.

However, these previous experimental visualization studies of liquid water inside the GDL have limitations with spatial and temporal resolution. Since the GDL has many components into the through-plane direction, as described in the Background and Motivation section, there is insufficient capability for analyzing the through-plane evolution of water transport, and is incapable of distinguishing the effects of each part of the GDL structure. Due to high costs and limited availability, only a few research groups worldwide conduct neutron imaging studies. Investigation of the effects of the various GDL structures on cell performance with experimental visualization is limited and thus additional analysis is imperative.

1.2.2.2 Numerical studies

One of the numerical studies for investigating micro-scale liquid water transport is pore-network model (PNM). In the PNM, a porous medium is represented at the microscopic level by a lattice of wide pores connected by narrower constrictions called throats. The morphology of a real porous medium is incorporated in the random pore-network structure and the PNM has relatively faster numerical analysis method than others.

Lee et al. [68] developed a pore-network model to observe the micro-scale behavior of liquid water transport in GDL's. It is found that the water saturation distribution in GDL's is lowered along the flow direction with a concave shaped slope. Additionally, the Geometric and capillary properties of GDL's, such as; pore distortion

factor, compression ratio, and contact angle, are analyzed. The same author group [69] developed a pore-network model combined with an invasion-percolation path-finding process. It is found that the water saturation in the GDL can be reduced by either decreased invaded pore fraction or GDL thickness. Luo et al. [70] developed a topologically equivalent pore network model, and observed the effect of the GDL morphology on liquid water transport in both the carbon cloth and carbon paper GDL types. Sinha et al. [71] develops a pore-network model with reflecting GDL morphology, and examines liquid water transport in the GDL as a function of capillary numbers. Wu et al. [72] develops a pore-network model, and investigates the effect of the MPL on liquid water transport in the GDL with pore level analysis. It is found that with an MPL it is possible to reduce the liquid water saturation of the GDL. The same researchers [73] also investigates the effect of bi-layered GDM on liquid water distribution with varying droplet size, coverage fraction and MPL properties, and find that increased droplet size reduces water saturation, and alters the shape of the water distribution profiles. A numerical study by Pauchet et al. [74] of the effect of hydrophobicity loss in a GDL on PEM fuel cell performance, using both combining pore-network and PEM fuel cell performance models, and elaborated the decrease of the through-plane gas diffusion coefficient in the PNM model. Additionally, using simulation, the increased flooding, decreased performance, and increased inhomogeneity of local current density in PEM fuel cell performance model are analyzed so as to characterize the GDL degradation, and its effects on the performance of the PEM fuel cell.

In the lattice Boltzmann model (LBM), the fluid consists of fictive particles, and such particles perform consecutive propagation and collision processes over a discrete lattice mesh. The LBM has advantages over other CFD methods, especially, in dealing with complex boundaries and incorporating microscopic interactions. Since the LBM

uses several grid per each pore size, it has higher computational demands than other numerical method such as the PNM [74].

Inoue et al. [75] conducted numerical analysis on flow and mass transfer in the GDL using a simulation model parameterized with respect to fiber diameter, average porosity, and thickness so as to evaluate structural properties, such as; local porosity distribution, surface roughness, pore size distribution, permeability, and tortuosity. Using a simple model incorporating tortuosity, PEM fuel cell performance is characterized according to an effective diffusion coefficient. It is concluded that the mass transport loss is largely affected by tortuosity. However, the simulated GDL did not include the MPL and the model did not consider two-phase transport and heat transfer. Hao et al. [76] studied liquid water transport in the GDL through development of a lattice Boltzmann method. It is found that the liquid water transport inside the GDL is dominated by the local capillary resistance. Thus, a GDL with non-uniform wetting characteristics transports liquid water, selectively, through the hydrophilic path with the smallest capillary resistance. Park et al. [77] develops a lattice Boltzmann model which reflects the morphology of the cloth type in a GDL. The GDL model includes a void space and fiber tow region for analysis of the permeability of the GDL, and it is found that the effective permeability of the GDL is dependent upon fiber tow orientation. Tabe et al. [78] develops a lattice Boltzmann model and analyzes the two-phase transport in the GDL. The simulation results show that the wettability of the channel dominantly affects the two-phase transport in a fuel cell.

These previous numerical studies only focused on the GDL itself so that they are useful to investigate the mass transport characteristics within this microscopic view. However, they could not connect the mass transport behavior of the GDL with cell performance directly due to difficulties in extension of the calculation domain. Thus, the previous numerical studies report only qualitative analysis when comparing

experimental and numerical results, although, analysis of mass transport characteristics of the GDL within the microscopic view is meaningful. The GDL is not a homogenous material but the total mass transport through the GDL has an average driving force. The macroscopic view with the average GDL properties is sufficient to understand the effect of such variables on GDL structure and cell performance. Consequently, developing a simplified model which can reflect each part of the GDL structure and predict the cell performance is needed to determine the correlation between the characteristics of mass transport and cell performance.

1.3 Objectives

The GDL is very important part of the PEM fuel cells, especially on mass transport behavior. Thus, much effort has been directed toward quantifying basic GDL characteristics, or the GDL structure design, with passage design for mass transport. Most experimental studies have investigated the mass transport behavior inside the GDL, qualitatively. Some experimental studies analyze cumulative water saturation inside the GDL quantitatively, though, with many limitations such as spatial and temporal resolution [79]. Numerical study of GDL's has the capability to quantify mass transport behavior inside the GDL, however, it is hard to investigate the relationship between cell performance and mass balance in the GDL due to high computational costs of PNM or LBM. Even though there are many attempts to design the GDL structure to enhance the mass transport capability, a more adequate investigation tool for assessing GDL's is warranted to achieve optimal passage design. Therefore, the objectives of this study are;

1. Developing the PEM fuel cell model which can consider the characteristics of each part of the GDL structure so as to understand the correlation between mass transport inside the GDL, and cell performance.
2. Investigation of the basic GDL structural characteristics which have different pore size in the substrate as well as different porosity, thickness, and contact angle within the experimental and simulation work.
3. Investigation of effects of the in-plane and through-plane structure design of the GDL by numerical simulation and experimental verification.

4. Lastly, suggestion of an ideal the GDL structure that would have improved mass transport capability and cell performance.

The PEM fuel cell model is developed by MATLAB®/Simulink®. One of the advantages of this study is that the PEM fuel cell model is adapted to macro-scale two-phase flow equations entailing Darcy's law and the concept of macroscopic capillary pressure and relative permeability. In the model, the dynamic characteristics of the cell are directly incorporated, and the results are likewise related to cell performance. The model is discretized in the through-plane direction and the model with through-plane direction is aligned with the in-plane coordinates. By this method, investigation of the effects of the GDL structure design in both the in-plane and through-plane directions is possible. It is expected that the reliability of the model will be straightforwardly measured by the experimental results. The model after validation can be used to predict the various GDL structural effects related to cell performance so that the ideal GDL structure can be suggested. The effect of suggested ideal GDL structure from the model is to be verified by experiment. In conclusion, the ultimate goals of this study -understanding the effect of the GDL structure on mass transport behavior and suggesting the ideal the GDL structure- are made practicable by coordination of experimental and simulation work. The methodology of this study is shown in Figure 1.5.

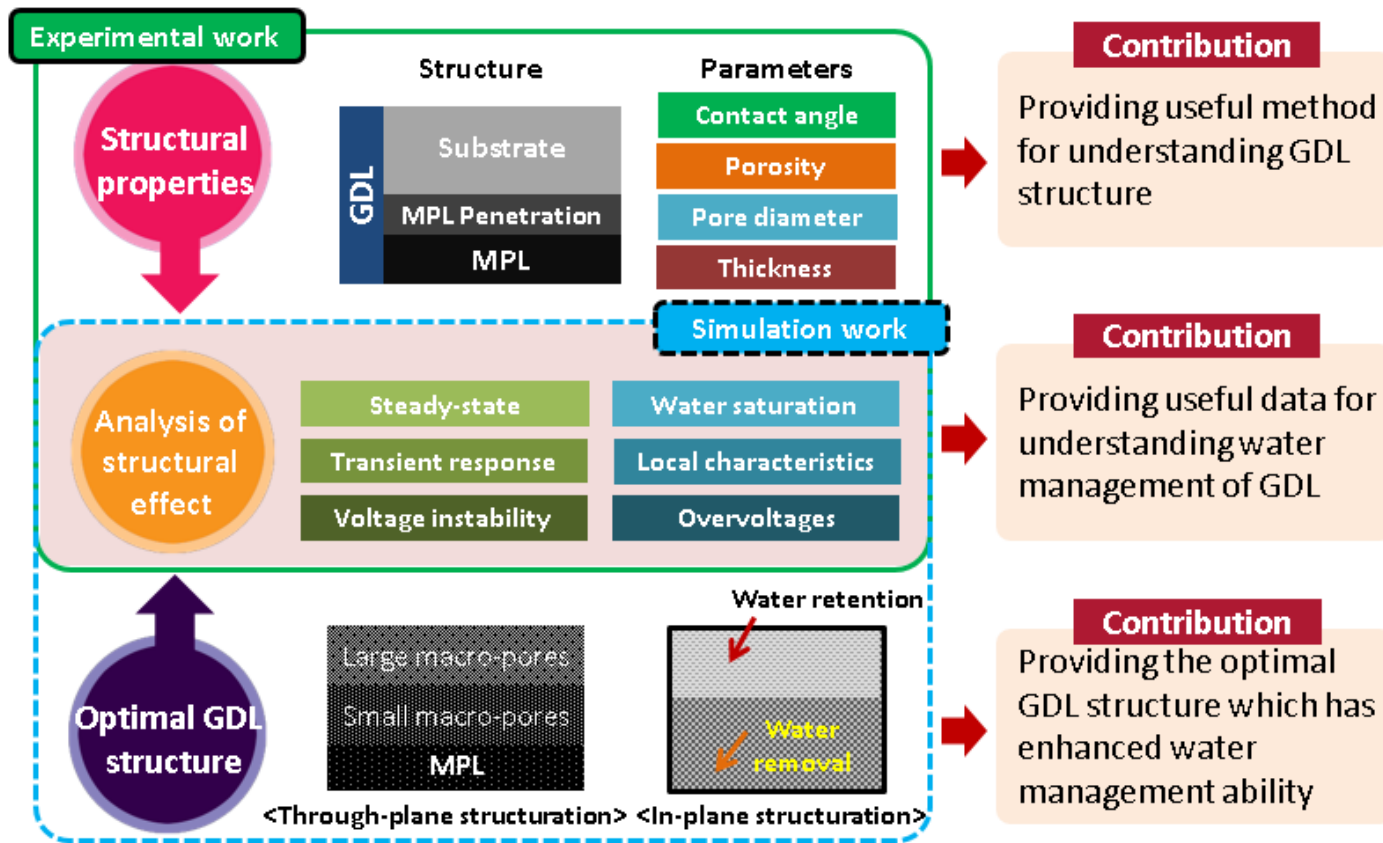


Figure 1.5 Methodology of the study

Chapter 2. Model descriptions and Experimental setup

2.1 Model descriptions

In this study, a dynamic, non-isothermal, and quasi-three-dimensional model of the PEM fuel cell is developed. The model used in this study is developed by modifying the previous model [80] to consider the structural characteristics of the GDL. The model is implemented in MATLAB[®]/Simulink[®] interface. For the simplicity of the model, the unit cell is firstly discretized in the through-plane (cross-sectional) direction (z) and then the model arranged by the in-plane (stream-wise) direction (x, y). By this method, the three-dimensional geometry of the model can be simplified (1+2D, quasi-3D) and the ordinary differential equations (ODEs) can be adopted in each control volumes. The model is simple enough for simulation on a personal computer (Intel[®] Core[™] i5 Processor (i5-2500K), 8.00 GB RAM), yet, capable of capturing the local characteristics of the PEM fuel cell. Each of the control volumes of the model is constrained by conservation equations of energy and species equations, likewise, the conservation equations are resolved for each control volumes and then the model predicts the reaction rate, heat transfer, mass transport, and cell voltage and current throughout the fuel cell from the numerical results of local temperatures and species mole fractions. Two-phase mass transport is adopted in the GDL control volumes and the model predicts liquid water transport and species diffusion throughout the GDL according to the water saturation in the GDL. Table 2.1 and 2.2 show the geometric PEM fuel cell model parameter values and the general PEM fuel cell model parameter value, respectively.

2.1.1 Assumptions

The major assumptions adopted in the model are same as those of Kang's work [80]. Each control volumes of the GDL and catalyst layer is considered as an isotropic porous media. Additionally, it is assumed that species diffusion throughout the GDL only occurs within the through-plane direction and diffusion within the in-plane direction is ignored [81, 82].

2.1.2 Discretization

To investigate the local characteristics of fuel cell, the unit cell is discretized into control volumes in a quasi-three-dimensional geometry. The one dimensional model along the through-plane direction (z) is discretized into twenty-five control volumes, which consist of the following components; (1) the solid plate, (2) the bulk gas, (3) the GDL, (4) the MEA, and (5) the coolant as shown in Figure 2.1. The merit of the model in this study is to consider the structural characteristics of the GDL along with fuel cell performance. To investigate the effects of the various the GDL structures, the GDL part is discretized into nine control volumes. As shown in Figure 2.2, there are four control volumes of substrate, two MPL penetrations, two MPLs, and one catalyst layer in the model. A two-phase mass transport equation is adopted in the GDL control volumes. It is with this discretization possible to understand the local characteristics of energy and mass transport of the cell in the through-plane direction. Specifically, the amount of liquid water inside of each GDL part can be quantified and its effect on mass transport behavior can be elucidated. According to the energy and mass transport, the operating voltage and local current is determined by the localized species mole fraction, temperature, and pressure at the catalyst layer control volumes. In addition

to discretization with the through-plane direction, the unit cell is also discretized in the in-plane direction. One set of twenty-five control volumes in the through-plane direction is repeated in the in-plane direction (x, y): one set of control volumes in the through-plane direction represents a single node and an associated segment of the fuel cell flow path. Each node is arranged along the flow channel geometry with the adjacent nodes connected for consideration of axial heat and mass transport. This allows the model to capture the local characteristics with serpentine flow geometry and the distributions of current density, temperature, and species molar concentrations. It is possible to investigate the effects of not only the through-plane structure design of the GDL but also the in-plane structure design of the GDL. In this study, as shown in Figure 2.3, the model comprises twenty nodes repeated along the stream-wise direction, which represent four-step serpentine flow channels.

2.1.3 Conservation equations

The basic characteristics of cell, such as; temperature, species mole fractions, and molar flow rate of each control volume, are solved from the first principles of conservation equations [82, 83]. Energy conservation and heat transfer equations are used to solve for the temperature; the species conservation and mass transport equations are used to solve for the species mole fractions and the molar flow rates. These equations are described given in the following sections (2.1.3.1, 2.1.3.2).

2.1.3.1 Energy conservation

Energy conservation equations are solved to determine the temperature within the control volumes. In the model, the outlet temperature of the control volume is

represented as the temperature of each control volume, and it is taken to be the inlet temperature of the next control volume in the in-plane direction.

The temperatures of each solid-plate control volume are determined by solving the following ordinary differential equation (ODE):

$$\rho \cdot V C \frac{dT}{dt} = \sum \dot{Q}_{in} \quad (2.1)$$

where \dot{Q}_{in} represents the amount of heat transferred from near control volumes.

Similarly, the bulk gas and the coolant temperature are determined by solving the following energy equation:

$$NC_v \frac{dT}{dt} = \sum \dot{N}_{in} h_{in} - \sum \dot{N}_{out} h_{out} + \sum \dot{Q}_{in} \quad (2.2)$$

The change in species enthalpy flux of each control volume is considered to determine the temperature of species mixture.

Since the control volumes of the GDL and MEA are assumed to have a lumped temperature, the temperature of the GDL and MEA is determined by combining the gas and solid control volume conservation equations (Equations (2.1) and (2.2)). For the MEA control volume, heat generation from the electrochemical reactions is modeled as follows:

$$\left(\sum (\rho \cdot V C)_s + \sum (NC_v)_g \right) \frac{dT}{dt} = \sum \dot{N}_{in} h_{in} - \sum \dot{N}_{out} h_{out} + \sum \dot{Q}_{in} + \Delta H \cdot \frac{I}{nF} - \frac{V \cdot I}{1000} \quad (2.3)$$

where ΔH is the enthalpy of water formation, and V and I are the fuel cell voltage and current, respectively.

2.1.3.2 Species conservation

The species molar flow rates and species mole fractions at each control volume are determined from the first principles of species mass conservation. The exit mole number of each bulk gas control volume is found from the species conservation equation:

$$\frac{d(N\bar{X})}{dt} = \dot{N}_{in} \bar{X}_{in} - \dot{N}_{out} \bar{X}_{out} + \sum \bar{\Phi} \quad (2.4)$$

Also, the exit molar flow rate is determined from the total species conservation equation:

$$\dot{N}_{out} = \dot{N}_{in} + \sum \bar{\Phi} - \sum \frac{d(N\bar{X})}{dt} \quad (2.5)$$

$\bar{\Phi}$ in Equations (2.4) and (2.5) is the species mass transport flux from the adjacent GDL control volume. The control volume mole fractions are assumed to be those at the control volume exits by the “perfectly stirred” assumption [82].

The species mole number of the catalyst layer control volume is determined as follows:

$$\frac{d\bar{N}}{dt} = -\sum \bar{\Phi} + \sum \Psi_{H_2O} + \sum \Theta_{H_2O} + \bar{R} \quad (2.6)$$

where $\Psi_{\text{H}_2\text{O}}$ is the water diffusion flux term from the near MEA control volume and $\Theta_{\text{H}_2\text{O}}$ is the water osmotic drag flux term through the MEA control volume. \bar{R} is the local electrochemical reaction rate for each species.

2.1.4 Heat transfer

When the electrochemical reaction occurs, heat is generated in the cell due to irreversibility. The heat generated from the MEA control volume is transferred to the adjacent control volumes via convection and conduction. The heat transferred to bulk gas through convection also transfers to the solid-plate control volumes through conduction. Heat in the solid-plate is then transferred to the coolant channel (in the case of cathode) or ambient air (in the case of anode) through convection. Not only heat transfers into the cross-sectional direction, but also heat is transferred between repeated control volumes along the in-plane direction. Specifically, conduction heat transfer between adjacent solid plates and natural convection at the edge of each solid plate is included in the model.

Convection heat transfer between solid and gas control volume is determined from Newton's law of cooling:

$$\dot{Q} = A \cdot h \cdot (T_2 - T_1) \quad (2.7)$$

Conduction heat transfer is determined from Fourier's law:

$$\dot{Q} = \frac{A \cdot k_s \cdot (T_2 - T_1)}{L} \quad (2.8)$$

2.1.5 Species mass transport and Reaction rates

Species mass transport $\bar{\Phi}$ and reaction rates \bar{R} in the mass conservation equations (Equations (2.4), (2.5), and (2.6)) are resolved in the model.

Species mass transport is considered between the bulk gas and the GDL control volumes. The driving forces of species mass transport from the bulk gas to the GDL are convection driven by a concentration gradient and diffusion. Throughout the GDL, the driving force of species mass transport is mainly diffusion. The mass transport coefficient \bar{g}_m at the interface between the gas channel and the GDL is obtained based on the Reynolds analogy between heat and mass transfer:

$$\bar{g}_m = \frac{Sh \cdot \bar{D}_m}{D_H} \quad (2.9)$$

where Sh is the Sherwood number, \bar{D}_m is the diffusion coefficient, and D_H is the hydraulic diameter of the gas flow channel.

The diffusion coefficients for the species mass transport are determined by the temperature and pressure. From the Bruggeman correlation [84], a modified diffusion coefficient is defined considering the effect of porosity and tortuosity of the GDL:

$$\bar{D}_m = \bar{D}_0 \left(\frac{T}{T_0} \right)^{3/2} \left(\frac{P_0}{P} \right) \quad (2.10)$$

$$\bar{D}_m^{\text{eff}} = \varepsilon^{1.5} \times \bar{D}_m \quad (2.11)$$

where \bar{D}_0 is the species diffusion coefficient at the standard pressure and temperature, \bar{D}_m^{eff} is the effective species diffusion coefficient, and ε is the GDL porosity. The effective species diffusion coefficient (Equation (2.11)) should be modified when considering two-phase flow because liquid water blocked the pore so that the porosity becomes smaller. Detailed explanation will be followed in section 2.1.7.

Consequently, the species diffusion flux between the bulk gas and the GDL is the as follows:

$$\bar{R}_{\text{dif}} = A \cdot \frac{1}{\frac{1}{g_m} + \frac{t_{\text{GDL}}}{\bar{D}_m^{\text{eff}}}} \quad (2.12)$$

$$\bar{\Phi} = \bar{R}_{\text{dif}} \cdot (\bar{C}_2 - \bar{C}_1) \quad (2.13)$$

where \bar{R}_{dif} is the total diffusion resistance of each species, and t_{GDL} is the thickness of the GDL.

The reaction rates of anode and cathode are function of the current from the Faraday's law:

$$\dot{R}_{\text{H}_2\text{O}} = -\dot{R}_{\text{H}_2} = -2\dot{R}_{\text{O}_2} = \frac{I}{n \cdot F} \quad (2.14)$$

2.1.6 Water transport between the GDL and MEA

Two mechanisms of water transport between the GDL and MEA are considered in the model. The one is the electro-osmotic drag and the other one is the diffusion due to a concentration gradient between control volumes.

The electro-osmotic drag from the anode side to the cathode side is proportional to the current and the electro-osmotic drag coefficient as follows:

$$\Theta_{\text{H}_2\text{O}} = n_d \cdot \frac{I}{A \cdot F} \quad (2.15)$$

where n_d is calculated from the membrane water content which is affected by water activity a , as follows:

$$n_d = 0.0029\lambda^2 + 0.05\lambda - 3.4 \times 10^{-19} \quad (2.16)$$

$$\lambda = \begin{cases} 0.043 + 17.81a - 39.85a^2 + 36a^3 & \text{for } 0 < a \leq 1 \\ 14 + 1.4(a-1) & \text{for } 1 < a \leq 3 \end{cases} \quad (2.17)$$

The water diffusion between the MEA and the GDL is expressed by the concentration gradient as follows:

$$\Psi_{\text{H}_2\text{O}} = D_w \cdot A \cdot \frac{(C_2 - C_1)}{t_{\text{MEA}}} \quad (2.18)$$

where D_w is the diffusion coefficient and t_{MEA} is the membrane thickness. The diffusion coefficient of water in the membrane is calculated from the empirical equation [85].

$$D_w = D_\lambda \cdot \exp\left[2416\left(\frac{1}{303} - \frac{1}{T}\right)\right] \quad (2.19)$$

where,

$$D_\lambda = \begin{cases} 10^{-6} & \text{for } \lambda < 2 \\ 10^{-6}(1 + 2(\lambda - 2)) & \text{for } 2 \leq \lambda \leq 3 \\ 10^{-6}(3 - 1.67(\lambda - 3)) & \text{for } 3 < \lambda < 4.5 \\ 1.25 \times 10^{-6} & \text{for } \lambda \geq 4.5 \end{cases} \quad (2.20)$$

The water concentration C is calculated from the membrane water content λ :

$$C = \frac{\rho_m}{M_m} \cdot \lambda \quad (2.21)$$

where ρ_m is the dry density of the membrane and M_m is the membrane dry equivalent weight.

2.1.7 Liquid water transport

Driving force of liquid water transport inside the GDL is the capillary pressure gradient. To calculate the capillary pressure of each the GDL control volume, firstly the saturation factor is needed. The saturation factor can be calculated as follows [86]:

$$s = \frac{V_{\text{liquid water}}}{V_{\text{pore}}} = \frac{C_w - C_{\text{sat}}}{\frac{\rho^{(l)}}{M_w} - C_{\text{sat}}} \quad C_w > C_{\text{sat}} \quad (2.22)$$

$$s = 0 \quad C_w \leq C_{\text{sat}} \quad (2.23)$$

Then, the two-phase mixture density is calculated as follows:

$$\rho = s\rho^{(l)} + (1-s)\rho^{(g)} \quad (2.24)$$

The interaction of the two-phase flows in the GDL is determined through the relative permeabilities, $k_r^{(l)}$ and $k_r^{(g)}$:

$$k_r^{(l)} = s^4 \quad (2.25)$$

$$k_r^{(g)} = (1-s)^4 \quad (2.26)$$

The relative mobilities of liquid and gaseous phase $\lambda^{(l/g)}$ are expressed as follows:

$$\begin{cases} \lambda^{(l)} = \frac{k_r^{(l)}/\nu^{(l)}}{(k_r^{(l)}/\nu^{(l)})+(k_r^{(g)}/\nu^{(g)})} \\ \lambda^{(g)} = \frac{k_r^{(g)}/\nu^{(g)}}{(k_r^{(l)}/\nu^{(l)})+(k_r^{(g)}/\nu^{(g)})} \end{cases} \quad (2.27)$$

The capillary pressure P_c is calculated by following equation:

$$P_c = \tau \cos(\theta_c) \left(\frac{\varepsilon}{K} \right)^{\frac{1}{2}} J(s) \quad (2.28)$$

where τ is surface tension, θ_c is contact angle, ε is porosity, K is permeability, and $J(s)$ is Leverette function.

The permeability K is determined by Kozeny-Carman relation with pore diameter and porosity as follows [87]:

$$K = \frac{\varepsilon^3 \left(\frac{1}{4} \sqrt{\frac{4}{\pi}} d_p \right)^2}{96(1-\varepsilon)^2} \quad (2.29)$$

Since the pore diameter is the same, permeabilities with different porosity can be expressed as follow:

$$\frac{K_1}{K_2} = \frac{\varepsilon_1^3 (1-\varepsilon_2)^2}{\varepsilon_2^3 (1-\varepsilon_1)^2} \quad (2.30)$$

The Leverett J-function is calculated by:

$$J(s) = 1.417s - 2.120s^2 + 1.263s^3 \quad (2.31)$$

Then, the capillary liquid water flux is determined:

$$\vec{j}^{(l)} = \frac{\lambda^{(l)} \lambda^{(g)}}{\nu} K \left[\nabla P_c + (\rho^{(l)} - \rho^{(g)}) \vec{g} \right] \quad (2.32)$$

As the liquid water occupy and block the pore inside the GDL, the effective diffusion coefficient (Equation (2.11)) for determining the species diffusion considering two-phase flow should be modified as follows:

$$\bar{D}_m^{\text{eff}} = [\varepsilon(1-s)]^{1.5} \cdot \bar{D}_m \quad (2.33)$$

2.1.8 Electrochemical model

The operating voltage of the cell is determined as follows:

$$V = V_{\text{Nernst}} - \eta_{\text{act}} - \eta_{\text{ohm}} \quad (2.34)$$

where the Nernst voltage is determined based on the species partial pressures in the catalyst layer and on the MEA temperature [88]. The Nernst voltage is determined from the following equation:

$$V_{\text{Nernst}} = E^0 + \frac{RT}{nF} \ln \left[\frac{P_{\text{H}_2} \cdot (P_{\text{O}_2})^{0.5}}{P_{\text{H}_2\text{O}}} \right] \quad (2.35)$$

with

$$E^0 = 1.23 - 2.304 \cdot 10^{-4} (T - 298.15) \quad (2.36)$$

The activation polarization is modeled using the Tafel equation:

$$\eta_{\text{act}} = \frac{RT}{\alpha F} \ln \left(\frac{I/A}{i_0} \cdot \frac{C_{O_2}^{\text{ref}}}{C_{O_2}} \cdot \frac{1}{1-s} \right) \quad (2.37)$$

where the $C_{O_2}^{\text{ref}}$ is the local reference oxygen concentration at the bulk gas channel and C_{O_2} is the local oxygen concentration which reaches at the catalyst layer by diffusion.

The membrane ionic conductivity is proportional to the membrane water content and expressed as follows:

$$\kappa = (0.005139\lambda - 0.00326) \cdot \exp \left(b_1 \left(\frac{1}{303} - \frac{1}{T_{\text{MEA}}} \right) \right) \quad (2.38)$$

The cell resistance is then modeled by the membrane ionic conductivity κ and the electric conductivity of the GDL σ with the ohmic polarization being proportional to the cell resistance:

$$R_{\text{ohmic}} = \frac{t_{\text{MEA}}}{\kappa} + \frac{2t_{\text{GDL}}}{\sigma} \quad (2.39)$$

$$\eta_{\text{ohmic}} = I \cdot R_{\text{ohmic}} \quad (2.40)$$

Through the Equations (2.34) to (2.40), the nodal voltage is determined. Since an equipotential electrode surface is assumed, however, the cell voltage and each nodal voltage cannot be different. Thus, each nodal current is iterated until all the

nodal voltage is the same with the cell voltage, satisfying the Ohm's law as shown in Equation (2.41).

$$V_{\text{node}} = V_{\text{cell}} = \sum I_{\text{node}} \cdot R \quad (2.41)$$

With this iteration, the sum of all nodal currents multiplied by the external resistance is equal to each nodal voltage and the cell voltage.

2.1.9 Pressure drop

The pressure drop is considered in the model to determine local pressures of the anode and cathode bulk gas channels. Each local pressure affects the local characteristics, such as the Nernst voltage. The Laminar Friction Constant fRe is 56.91 for square or rectangular flow geometry. The Reynolds number, friction factor, head loss, and pressure drop are expressed in following equations, respectively [89]:

$$Re = \frac{\rho v D_H}{\mu} \quad (2.42)$$

$$Re \leq 2100 \quad f = \frac{56.91}{Re} \quad (2.43)$$

$$h_f = f \frac{L}{D_H} \frac{v^2}{2g} \quad (2.44)$$

$$\Delta p = \rho g h_f \quad (2.45)$$

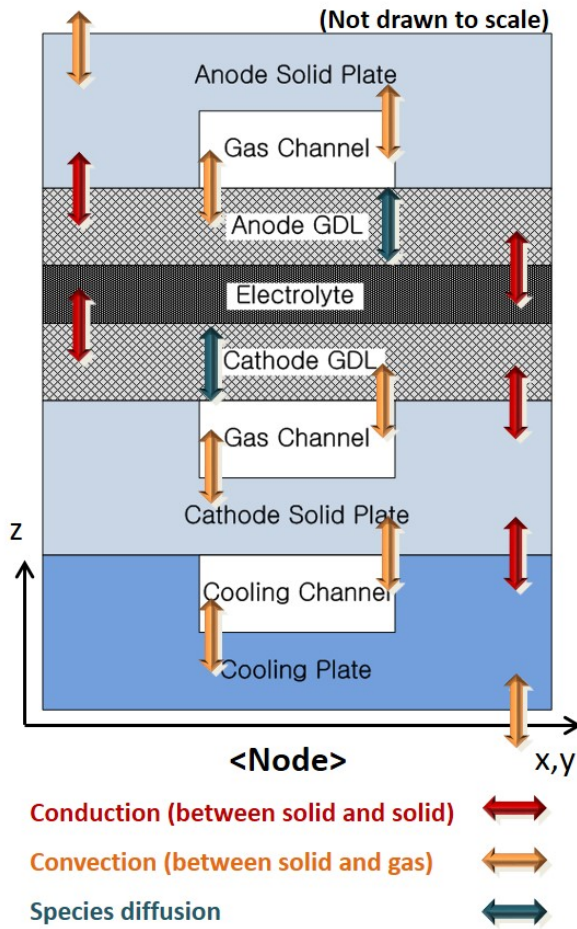


Figure 2.1 Schematic diagram of one-dimensional model with cross-sectional direction

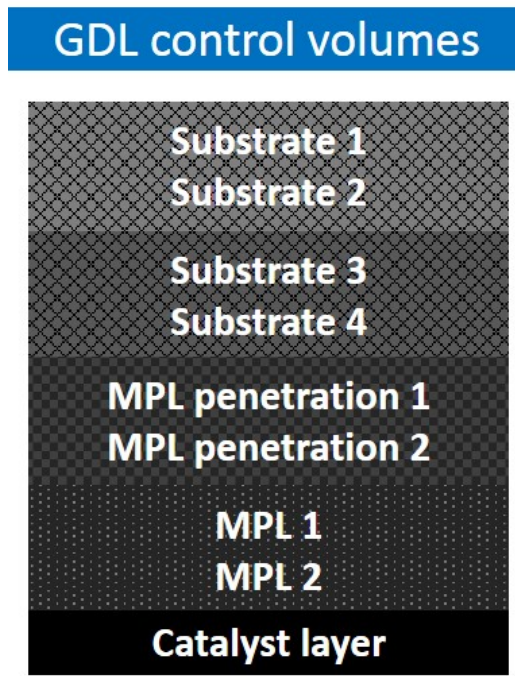


Figure 2.2 Schematic diagram of the GDL control volumes

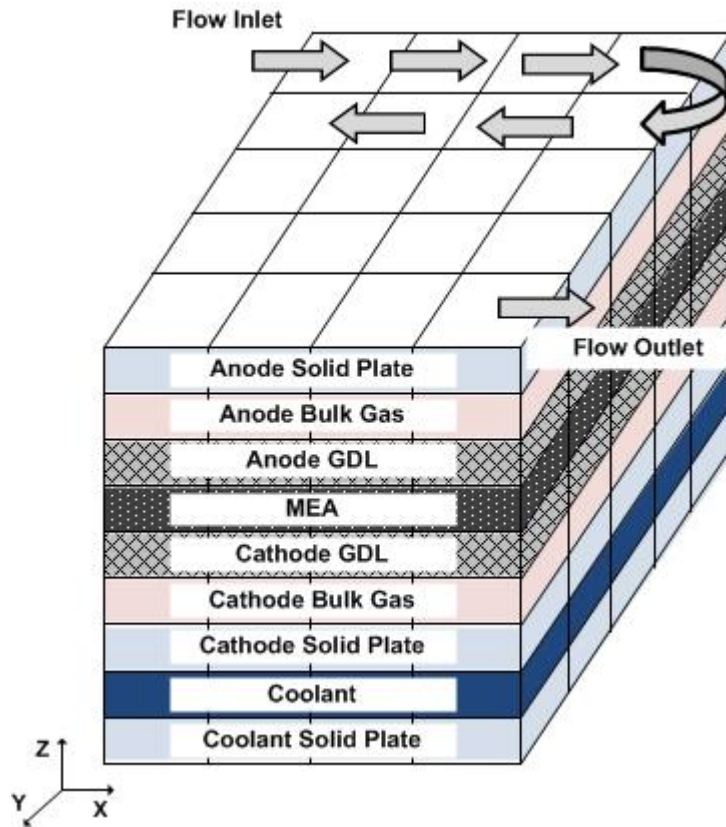


Figure 2.3 Illustration of the stream-wise and the cross-sectional discretization of a PEM fuel cell (not drawn to scale)

Table 2.1 Geometric PEM fuel cell model parameter values

Description	Value	Units
Cell width (x)	0.05	m
Cell height (y)	0.05	m
Depth of anode gas channel (z)	0.002	m
Depth of cathode gas channel (z)	0.002	m
Thickness of separator plates (z)	0.002	m
Thickness of electrolyte (z)	2×10^{-5}	m
Thickness of catalyst layer (z)	1×10^{-5}	m

Table 2.2 General PEM fuel cell model parameter value

Description	Value	Units
Transfer coefficient	0.56	-
Exchange current density	1.5×10^{-4}	A cm ⁻²
Cell temperature	65	°C
Anode stoichiometric mass flow rate (H ₂)	1.5	-
Cathode stoichiometric mass flow rate (air)	2.0	-
Coolant inlet temperature	65	°C
Anode/cathode inlet pressure	101.4	kPa
GDL conductivity	220	S m ⁻¹
Permeability of MPL penetration (assumption)	1×10^{-13}	m ²
Permeability of MPL @ porosity of 0.4 [90]	2.5×10^{-13}	m ²
Permeability of catalyst layer @ porosity of 0.1 [91]	1×10^{-15}	m ²

2.2 Experimental setup

2.2.1 Fuel cell and test station

As shown in Figure 2.4, a 25 cm² unit cell with a parallel serpentine flow pattern of channel size 1 mm × 1 mm is used to investigate the cell performance according to the various GDL structure. The same GORE™ PRIMEA® 5730 catalyst coated membrane (0.4 mg Pt/cm² on the cathode, 0.1 mg Pt/cm² on the anode) is used for each experiment with the target GDL on both sides of anode and cathode. After assembling the cell, activation process is conducted before the performance test and nitrogen purge process is carried out after the test for all cases to maintain the same experimental operating conditions. High purity of hydrogen (99.999%) and air are supplied to the cell with humidification. All supplying reactant gas lines are heated to maintain cell operating temperature. To remove the generated heat from the cell, a cooling fan is used in front of the cathode side. Basically, the electric loader (class of 1kW) is used to control the load change. Additionally, the voltage data is obtained with a data acquisition board (USB6009) from National Instrument for saving fast and reliable voltage responses during the load changes.

2.2.2 Experimental condition

The cell performing test is conducted with maintaining a temperature of 65 °C and inlet gas pressure of 1 atm. The stoichiometric ratios of hydrogen and air are fixed to 1.5 and 2.0 respectively. Relative humidity conditions which are conducted in this study are 50% and 100%. All voltage data from the experiment are measured with a data acquisition rate of 100 Hz. Steady-state performance test is conducted while

maintaining each current step for three minutes and averaging the voltage data except the first one minutes and the last thirty seconds. The transient performance test is conducted at a sudden load current change from 15 A to 30 A (0.6 A/cm² to 1.2 A/cm² in current density). During the transient performance test, the flow rates are fixed with those of high-load condition. Due to the limitation of the response of the gas flow at the mass flow controller. Standard deviation of the voltage as a current density is also measured in the same condition.

2.2.3 Water permeability test

To determine the internal contact angle, water permeability of the GDL is measured as shown in Figure 2.5. The test apparatus had a chamber made of a stainless steel cell with 17 cm high. Two Teflon tubes of 1/4 inch diameter with 2 m high are connected to the top of the chamber. There is another Teflon tube besides the chamber with a ruler to measure the height of water inside of Teflon tubes. A diameter of 5.0 cm of the GDL sample is inserted into the bottom of chamber and 0.2 LPM of water with 25 °C is continuously added to the chamber by Teflon tube using a pump. The maximum height of water inside of Teflon tube at which water passes through the GDL sample and begins to flow is measured. Then the maximum pore pressure is calculated with conventional meter of water (1 mH₂O = 0.097 atm). With the maximum pore pressure, the internal contact angle of the GDL is calculated as follows [92]:

$$P = \frac{4\tau \cos \theta}{d} \quad (2.46)$$

where P is the maximum pore pressure, τ is surface tension of water, d is diameter of pore, and θ is the internal contact angle.

2.2.4 Surface contact angle measurement

The surface contact angle is measured by the sessile drop method. To make the water droplet, a micro syringe pump (Harvard Apparatus, Pump 11) is used. Water droplet on the GDL surface is captured by zoom lens with CCD camera (TS-93001, SUGITOH, Japan). A halogen lamp is used as a backlight, and measurement of droplet height and contact angle is conducted with NEX MEASURE software. The surface contact angle increases as the water droplet height increases. Therefore, the height of water droplet is fixed to 1.3 mm in this study. The schematic diagram of the surface measurement system is depicted in Figure 2.6.

2.2.5 Mercury Porosimetry

The porosity and pore size distribution of the GDL is measured using a mercury porosimetry (AutoPore IV 9520, Micromeritics, USA) as shown in Figure 2.7. From the same equation (Equation (2.46)), mercury can fill smaller pore size as the intrusive pressure of mercury increased. Consequently, pore diameter corresponding to the pore with filled mercury is inversely proportional to pressure. With this mechanism, porosity and pore size distribution could be calculated with measurement of the volume of filled mercury as an increased pressure.

2.2.6 Scanning electron microscope (SEM)

The surface and cross-sectional images of the GDL are captured by the scanning electron microscope (FE-SEM SU70, Hitachi, Japan). Especially, the cross-sectional images are captured by using exclusive jig for preventing the sample from tilting. With the SEM images, the structural differences of the GDL could be investigated.

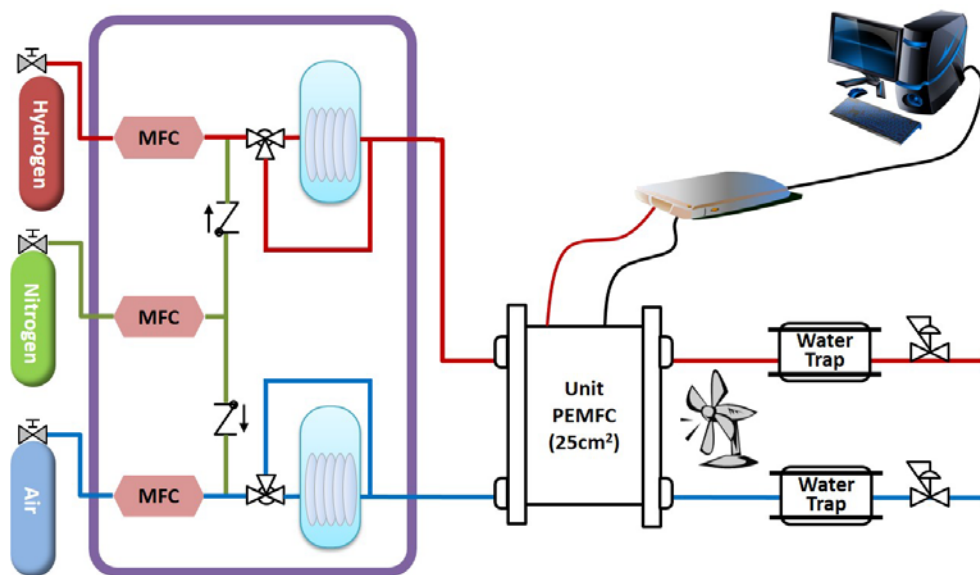


Figure 2.4 Experimental apparatus for testing the 25 cm² PEM fuel cell

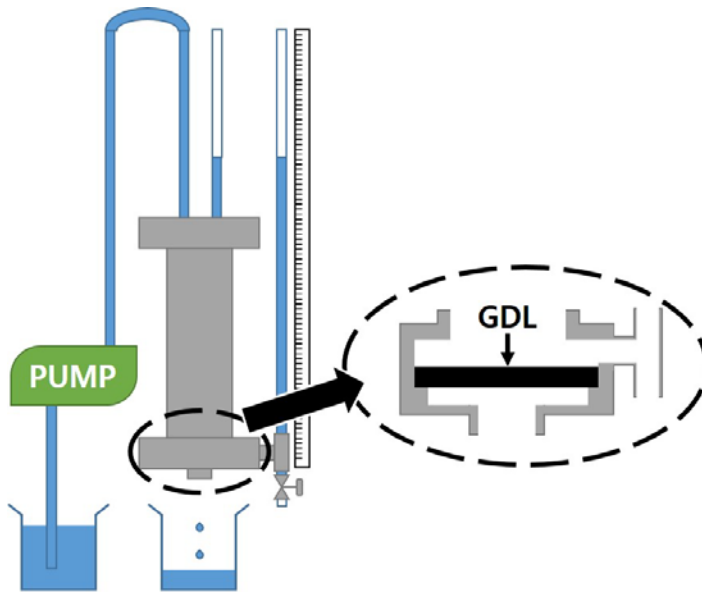


Figure 2.5 Experimental apparatus for measuring water permeability of the GDL

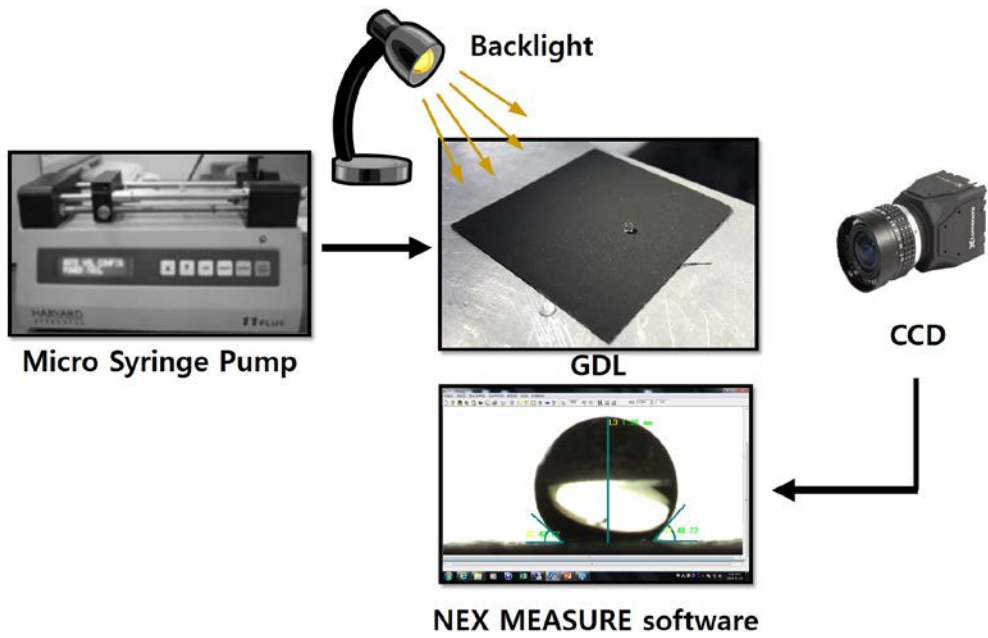


Figure 2.6 Experimental process for measuring surface contact angle of the GDL

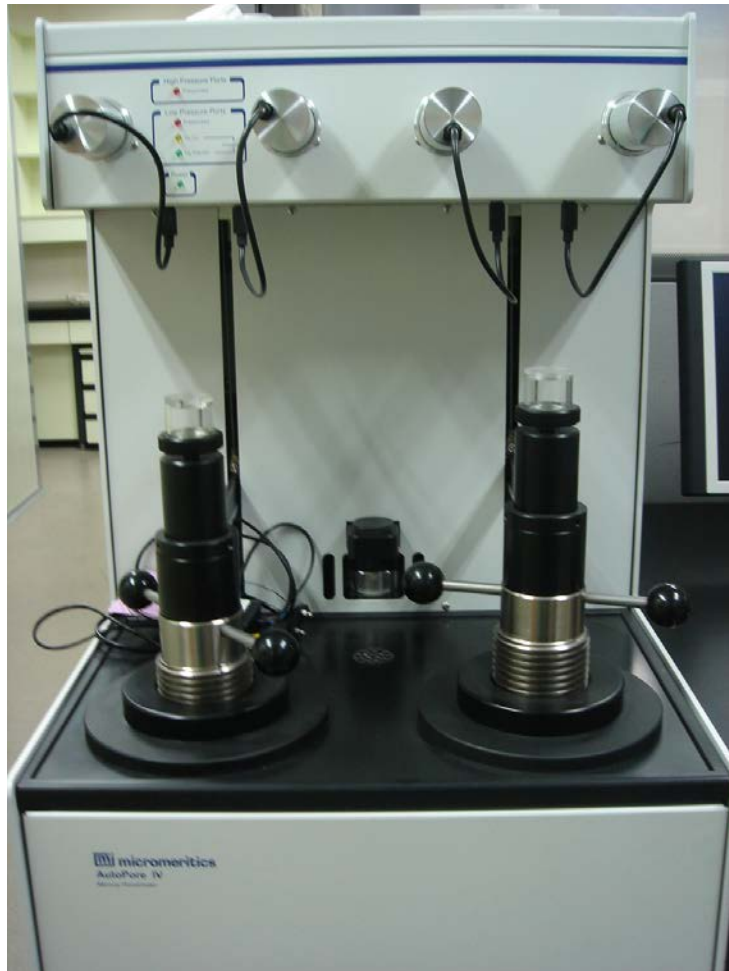


Figure 2.7 Mercury porosimetry

Chapter 3. Effect of the pore size variation in the substrate on water management and cell performance

3.1 Structural parameters of the GDL

To enhance the water management and mass transport capability of the GDL, many attempts to design the various GDL types have been fabricated. Much attention has been devoted to increasing hydrophobicity so as to enhance water removal capability. Although research on controlling the amount of PTFE have widely been conducted, the structural parameters of the GDL that affect the liquid water and mass transports are not only hydrophobicity. As discussed in the Model descriptions chapter, the main structural parameters of the GDL are porosity, pore diameter, thickness, and contact angle, as is, the overall permeability of the GDL. However, the permeability can be expressed with porosity and pore diameter as in Equation (2.29). By revising the Equations (2.28) and (2.32) with the Equation (2.29), substitution of the permeability K to the porosity and the pore diameter, the capillary pressure and liquid water flux can be expressed as follows:

$$P_c = \tau \cos(\theta_c) \left(C_1 \frac{(1-\varepsilon)}{\varepsilon d_p} \right) J(s) \quad (3.1)$$

$$\vec{j}^{(l)} = \frac{\lambda^{(l)} \lambda^{(g)}}{\nu} C_2 \frac{\varepsilon^3 d_p^2}{(1-\varepsilon)^2} \left[\nabla P_c + (\rho^{(l)} - \rho^{(g)}) \vec{g} \right] \quad (3.2)$$

with

$$C_1 = 34.73 \text{ and } C_2 = 8.29 \times 10^{-4} \quad (3.3)$$

The porosity of the GDL affects the mass diffusion, liquid capillary pressure, and liquid water flux through the GDL. As the porosity increases, the effective mass diffusion coefficient and the liquid water flux are increased while the capillary pressure is decreased. It means that when the porosity increases, water removal capability is enhanced due to increase in capillary pressure gradient and liquid water flux. Additionally, mass transport capability is enhanced due to increased porosity and lowered liquid water saturation. The pore diameter affects the capillary pressure and liquid water flux inside the GDL. In the same manner of porosity effect, increase in pore diameter enhances water removal capability. The GDL thickness affects the diffusion resistance and liquid water saturation. As the GDL thickness increases, mass diffusion is decreased as well as liquid water saturation if the same amount of water is maintained. Lastly, the contact angle affects the capillary pressure. As the contact angle increases, the capillary pressure is increased. To increase the capillary pressure gradient within the GDL and enhance the water removal capability, the porosity, pore diameter, and thickness of each GDL part such as MPL, MPL penetration, and substrate should be continuously increased and the contact angle should be steadily decreased in the direction from the catalyst layer to the channel.

Consequently, to enhance the water management capability of the GDL in an active way, understanding GDL design parameters is primary. After that, applying the design parameters and suggesting the ideal GDL structure follow.

To investigate one of the main GDL structural parameters, pore diameter, two types of GDL's with different pore size are tested in this chapter. With GDL's, investigation of the effect of pore size variation of the substrate on the PEM fuel cell characteristics can be conducted.

3.2 Design of the GDL

To control the pore size in the substrate, two types of carbon fibers whose lengths are 13 mm and 6 mm are used. Generally, the relatively large macro-pore is formed when the long carbon fibers are used. Conversely, short carbon fibers make the relatively small macro-pores. Given this mechanism, two types of GDL's with controlling portion of each fiber length are designed. Two GDL's have almost the same areal weight. However, the weight portion of the two different carbon fiber lengths is different: for one, the weight portion of short carbon fiber length (6 mm) is 80% and for long carbon fiber length (13 mm) is 20%; for the other, short and long fibers, the weight portions are reversed. To refer to each GDL in a simple way, the notations of "S8L2" and "S2L8" will be used in this study for the first and second, respectively. Table 3.1 shows the basic characteristics of two GDL's such as thickness and areal weight. The areal weight of each GDL has almost the same and the total thickness of S2L8 is 4.3% longer than that of S8L2. However, the ratio of substrate thickness to total GDL thickness of two samples is same as 83.3%. As mentioned in the Background and Motivation section, when the MPL slurry coated on the substrate, some carbon particles penetrate into the substrate and the MPL penetration region is formed. In this study, it is assumed that the MPL penetration part is 23% of the whole substrate thickness. The thicknesses of the substrate and MPL are measured easily during manufacturing process. However, it is hard to estimate well how much the MPL slurry penetrates into the substrate. Thus, the MPL penetration thickness of samples is determined using the cross-sectional SEM images, which is discussed in the following section 3.3. The amount of the PTFE of the samples is by wt.10% to fix the hydrophobicity characteristics between two samples.

Table 3.1 Basic GDL characteristics of S8L2 and S2L8

Description	S8L2	S2L8
Weight percent of short carbon fiber (6 mm)	80 %	20 %
Weight percent of long carbon fiber (13 mm)	20 %	80 %
Thickness	305 μm	318 μm
Areal weight	98.1 g/m^2	97.3 g/m^2

3.3 Experimental results

3.3.1 Analysis with scanning electron microscope

To investigate and validate the structural characteristics of two samples, the images of scanning electron microscope (SEM) are observed. Figure 3.1 shows the surface SEM images of S8L2 and S2L8. The magnifications of images are x50 and x100. The macro-pore of the substrate is formed between fibers. In the figure, the short carbon fibers which have length of 6 mm overlapped more frequently than that of 13 mm so that relatively small macro-pores are formed in S8L2 while relatively large macro-pores are formed in S2L8 with long carbon fibers. In Figure 3.1, the S8L2 sample had smaller macro-pores on the whole GDL compared with the S2L8 sample. In the cross-sectional SEM images which are shown in Figure 3.2, the difference between S8L2 and S2L8 is also observed. As shown on the surface SEM images, the pore size of S8L2 is smaller than that of S2L8. It seems that S2L8 has more vacant spaces than S8L2.

Consequently, since the S8L2 and S2L8 with different weight portion of the fiber lengths which are 13 mm and 6 mm, the effect of different weight portion of the fiber lengths caused different macro-pore sizes of the substrate.

Furthermore, the thickness of the MPL penetration can be estimated with the cross-sectional SEM images. As shown in Figure 3.3, the thickness of the MPL is obtained by subtracting the thickness of the substrate from the total GDL thickness ($c = a - b$) as the thickness of the substrate (b) and total GDL (a) are known. From the cross-sectional SEM images of the GDL, the thickness from the boundary between the substrate and the MPL to the end of the MPL ($c + d$) is estimated. With the

estimated thickness, the MPL penetration thicknesses (d) is obtained. In Figure 3.3, the estimated thicknesses (c + d) of both samples are about 110 μm and 114 μm , respectively, and the MPL penetration thickness (d) are obtained to 59 μm , and 62 μm , respectively. The penetration ratio, which is defined as the amount of the substrate filled with MPL, is calculated with the estimated penetration thickness. The penetration ratios of S8L2 and S2L8 are 23.2% and 23.4%, respectively. In this study, considering the variation of GDL's, the penetration ratio is assumed to be 23%. Therefore, the MPL penetration thicknesses of S8L2 and S2L8 are 58 μm and 61 μm , respectively. The thicknesses of each the GDL part of S8L2 and S2L8 are listed in Table 3.2.

3.3.2 Analysis with porosimetry

In addition to analysis using the SEM, analysis with mercury porosimetry is conducted to observe the pore size distribution and porosity according to the pore size of the GDL. Figure 3.4 shows the pore size distribution of S8L2 and S2L8. There are in the results, two large peaks near 0.05 μm and near 40 μm with an additional small peak near 1 μm . The peaks near 0.05 μm and near 40 μm are the MPL and substrate region, respectively. The small peak near 1 μm is the MPL penetration region. The pore sizes of the MPL and MPL penetration region of two samples are almost the same and the pore sizes at each peak are 0.05 μm and 1 μm , respectively. In case of the substrate, however, the pore sizes at the peak of S8L2 and S2L8 are 36.6 μm and 49.5 μm respectively. As observed in the SEM analysis, the pore size between two samples differs as is intended in their fabrication.

From the results of mercury porosimetry, the porosity of the GDL could be calculated with the volume of mercury, which penetrates the GDL pores. The total

porosity with the pore size range of 0.01 to 200 μm of S8L2 and S2L8 are 71.0% and 72.2%, respectively. The definition of porosity is the amount of void volume exists in the total volume:

$$\varepsilon = \frac{V_{\text{void}}}{V_{\text{total}}} = \frac{V_{\text{total}} - V_{\text{solid}}}{V_{\text{total}}} = \frac{\frac{1}{\rho_{\text{total}}} - \frac{1}{\rho_{\text{solid}}}}{\frac{1}{\rho_{\text{total}}}} \quad (3.4)$$

Regardless of the pore size, the porosity is determined by the areal weight, thickness, and density of the materials that comprise the GDL. Since the S8L2 and S2L8 had almost the same areal weight, the total porosity of two samples are also similar. Additionally, the porosity of each single GDL component, such as; MPL, MPL penetration, and substrate could be calculated by mercury porosimetry. Generally, the pore size of micro-pores of MPL is under 0.1 μm , and that of meso-pores of the MPL penetration is from 0.1 μm to 5 μm . Lastly, the pore size of macro-pores of substrate is from 5 μm to 200 μm [9]. Table 3.3 shows the local porosity of each GDL part of S8L2 and S2L8. The local porosity of each GDL part is determined by the volume of mercury which penetrate the certain pore size of each part. However, the value is not the porosity of each single part of the GDL: the value is determined by the volume of mercury which penetrates each pore size with respect to the whole volume of the GDL. Therefore, the thickness of each part of the GDL, which is the parameter of the GDL volume, should be considered to determine the porosity of each single part. Considering the thickness ratio between each GDL part and the whole GDL, the local single porosity of each part could be calculated and shown in Table 3.3. It is noted that there is no large difference between the local porosities of the substrate in the two samples. However, local porosities of the MPL and the MPL penetration showed large differences between two samples. It seems that they are affected by the pore size.

When the MPL slurry penetrated into the substrate, it is prone to fill the substrate densely due to S8L2 having relatively small macro-pores. After filling the substrate, the rest of the MPL slurry formed the MPL densely as well. Therefore, both porosities of the MPL and MPL penetration are decreased. In the case of S2L8, in contrast, it had relatively large macro-pores so that the MPL slurry might fill the substrate coarsely and formed coarse MPL penetration as well as MPL.

3.3.3 Analysis with water permeability and surface contact angle measurement

The contact angle of the GDL is the criterion of the hydrophobic property. The contact angle of the GDL is usually measured by the sessile drop method [93]. However, it is difficult to measure an accurate contact angle because of the rough surface of the substrate and the effect of water droplet weight. Also, during measuring the surface contact angle, water on the surface is not affected by internal pore structure. Consequently, it is difficult to relate the structural characteristics of the GDL to the value. Hence, it is required to measure the internal contact angle which represents the value on the inside the GDL pore [94]. To measure the internal contact angle, water permeability test is conducted and the maximum pore pressure is measured as described in the section 2.2.3. To evaluate the internal contact angle of the substrate, the samples of S8L2 and S2L8 which have no MPL are used. To maintain the hydrophobic property, PTFE is treated as the samples with the same amount by wt.10%. The water permeability test is conducted three times for each sample and then averaged for which maximum pore pressure is obtained. The maximum pore pressures of S8L2 and S2L8 is 3121.8 Pa and 2840.7 Pa, respectively. As shown in Equation (2.46), determining the internal contact angle requires pore diameter. To obtain the pore diameter, the substrate only samples also investigated the pore size

distribution. Figure 3.5 shows the pore size distribution of the substrate only sample of S8L2 and S2L8. In the substrate only sample, which has no MPL and MPL penetration, the number of pore and the pore size increased. The peak pore sizes of S8L2 and S2L8 are $49.5 \mu\text{m}$ and $60.5 \mu\text{m}$, respectively. Since the test is conducted at the room temperature, the surface tension value is 0.072 N/m . Collectively, the internal contact angles of S8L2 and S2L8 are determined as 122.4° and 126.6° .

To compare the internal contact angle to the surface contact angle, the static contact angle measurement by the sessile drop method is used. As a result, the surface contact angles of the S8L2 and S2L8 are 138.0° and 138.4° , respectively. As expected, the surface contact angle is higher than the internal contact angle due to the surface roughness. Additionally, there is no difference in values between two samples. These results verified that surface contact angle could not reflect the structural characteristics of the GDL.

However, the internal contact angle measurement of the MPL is not possible because the MPL cannot exist in a single layer. Since the surface roughness of the MPL is smoother than that of the substrate, the effect of roughness on the surface contact angle may be minor. Therefore, the contact angle of the MPL is determined with the surface contact angle in this study. In the sessile drop method, the surface contact angle of the MPL is 140.5° in both S8L2 and S2L8 because the same MPL slurry is used.

Since the MPL penetration part does not have a surface and cannot exist in a single layer, it is not possible to measure both the internal contact angle and the surface contact angle. In this study, therefore, the contact angle of the MPL penetration part is assumed to be 130° which is near the averaged value between the substrate and MPL.

3.3.4 Analysis with steady-state performance

Figure 3.6 shows the steady-state performance of the S8L2 and S2L8 at the RH 100%, 50%, and 30% conditions. At full humidification, the S8L2 experienced mass transport loss at the high-load region. In contrast, the S2L8 is advantageous at full humidification: in comparison, the voltage of the S8L2 at the current density of 1.6 A/cm² is 10.3% lower than that of S2L8 under RH 100%. These results indicate that mass transport resistance increased as the pore size of the macro-pores decreases. In case of RH 50% condition, the performances between two samples are almost the same but the voltage of S8L2 at high-load condition is slightly higher than that of S2L8. The voltage of the S8L2 at the current density of 1.6 A/cm² is 4.2% higher than that of S2L8 under RH 50%. In case of RH 30% condition, the performance of S8L2 is higher than S2L8 especially at the high-load condition. The voltage of the S8L2 at the current density of 1.6 A/cm² is 68.1% higher than that of S2L8 under RH 30%. The advantage in performance of the S8L2 under the low humidification (RH 50% and 30%) compared to the fully humidification can be explained in two ways. The first one is that the significant mass transport loss of the S8L2 at RH 100% is improved due to the low humidification. The second one is that the GDL with relatively small macro-pores had water retention capability so that the GDL hydrates the membrane at low humidity. Therefore, the performance graph of RH 100% and 50% of S8L2 had the cross point at the current density of 1.2 A/cm² (Figure 3.7). In other words, the cell performance of S8L2 at RH 50% is higher than that of RH 100% condition under the current density over 1.2 A/cm². In contrast, the results of S2L8 had no cross point between two conditions. The voltage values of the whole current density region under RH 50% condition are lower than at RH 100%.

Voltage instability is estimated by standard deviation of voltage according to the current density. Generally, the cell voltage fluctuated with the sluggish oxygen supply due to blockage of the pores with saturated liquid water or local deficit. The voltage instability is usually increased as current density increases because the large amount of reactants and products that exists in the cell. Therefore, it is a criterion of the level of overvoltages such as activation overvoltage including mass transport loss and ohmic overvoltage. Figure 3.8 shows that the voltage instability of S2L8 is lower than S8L2 at full humidification. These results indicate that the mass transport loss of S2L8 is better than S8L2 with enhanced water removal capability. In RH 50% condition, the voltage instability of S8L2 is lower than S2L8 at the low-load condition under 0.8 A/cm². After that, however, it exceeded the value of S2L8. In respect to the water retention capability, the S8L2 is remarkable at low-load condition. As the current density increased, the water retention capability is reduced with increased mass transport loss despite of the RH 50% condition. In the RH 30% condition, there is no significant difference between S8L2 and S2L8. It means the difference in mass transport loss of two samples under extremely low humidification is negligible. These results also support the characteristics of macro-pores variation in the substrate between S8L2 and S2L8.

3.3.5 Analysis with transient response of voltage

Since the PEM fuel cell performance is dominated by the membrane water content, the water retention and removal capability (termed water management) is very important, notably, in the transient responses on the cell voltage. As described in the model description section (section 2.1), the water flux inside the membrane is determined by two flux terms: electro-osmotic drag and back diffusion as follows:

$$J_{\text{H}_2\text{O}} = \overbrace{2n_d \frac{I}{2F} \frac{\lambda}{22}}^{\text{Electro-osmotic drag}} - \overbrace{\frac{\rho_m}{M_m} D_\lambda(\lambda) \frac{d\lambda}{dz}}^{\text{Back diffusion}} \quad (3.5)$$

When the current load rapidly increases, the electro-osmotic drag increased from anode to cathode and the membrane becomes dehydrated. After that, the water concentration at the interface between the cathode catalyst layer and the GDL increased temporarily. Back diffusion from cathode to anode also increased with the water mass balance between anode and cathode catalyst layer. Therefore, the water retention/removal capability of the GDL is very crucial because it affects the net water flux in the membrane directly. Therefore, it is concluded that observation of the transient response of voltage is key to evaluation of GDL characteristics, especially under the RH 50% condition due to harsh condition for membrane hydration [95].

Figure 3.9 shows the transient response of voltage of S8L2 and S2L8. In case of RH 100%, both results showed almost no voltage undershoots because the fully hydrated condition mitigates the membrane dehydration. However, the voltage instability of S8L2 is higher than that of S2L8, as described in the section 3.7. It indicates that the S8L2 could not remove the increased water from electro-osmotic drag and water production properly: a flooding phenomenon is induced with the S8L2. These results also support that S8L2, which has relatively small macro-pores, lacks water removal capability. In case of RH 50% condition, in contrast, the trend is reversed. Due to relatively low humidification, both results showed the voltage undershoots when the step change in current is applied. After the voltage undershoots, the amount of voltage recovery and recovery time are important factors in evaluating the GDL. The voltage recovery after current step of S8L2 is larger relative to that of S2L8. Contrary to the results of at RH 100%, the water retention capability of S8L2 is effective at RH 50% condition. The high water concentration at the cathode GDL

of S8L2 allowed improved back diffusion to the dehydrated membrane so that large voltage recovery could be possible. After the current step, the cell voltage of S8L2 is 13% recovered while that of S2L8 is 9.5% recovered. In the same manner, the results of S8L2 under RH 30% also shows the large and fast voltage recovery after the step change in current is applied, relative to the results of S2L8.

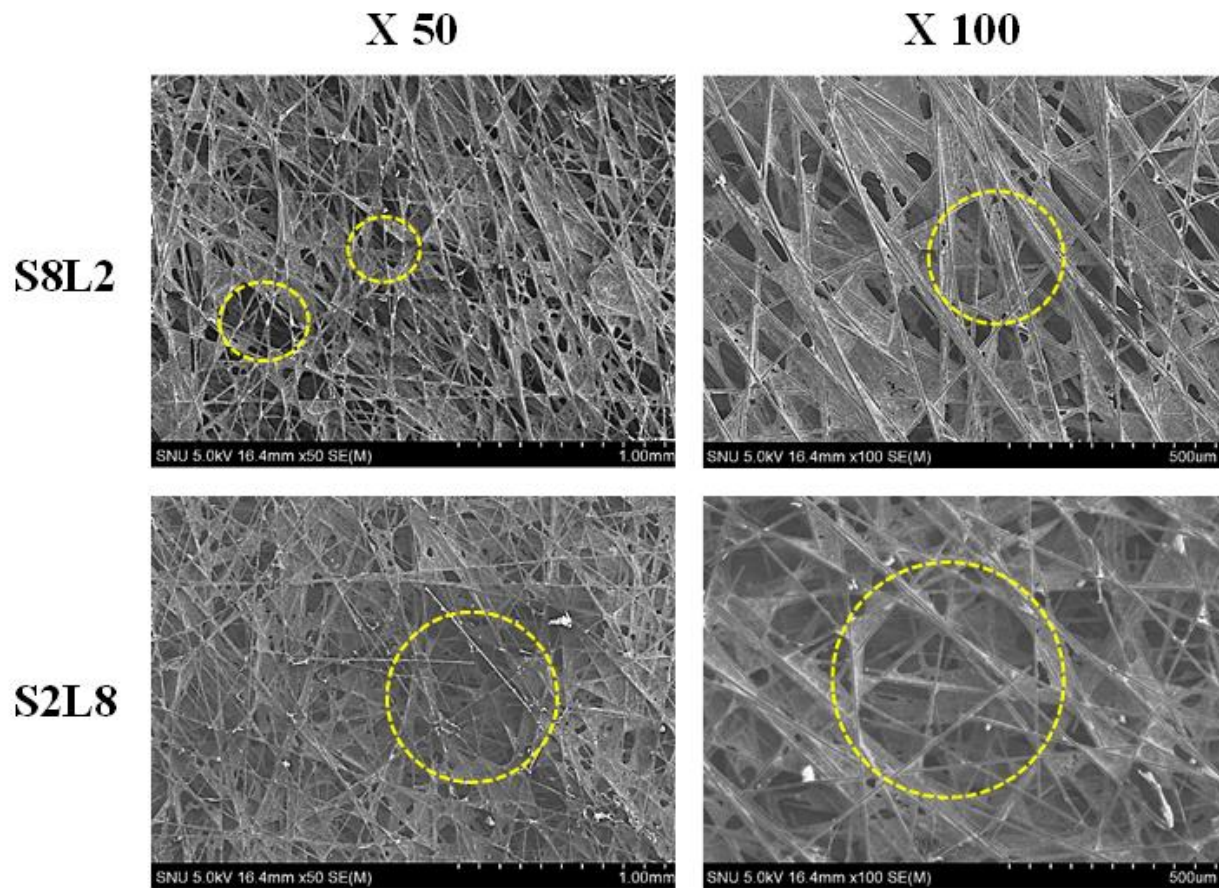


Figure 3.1 Surface SEM images of S8L2 and S2L8

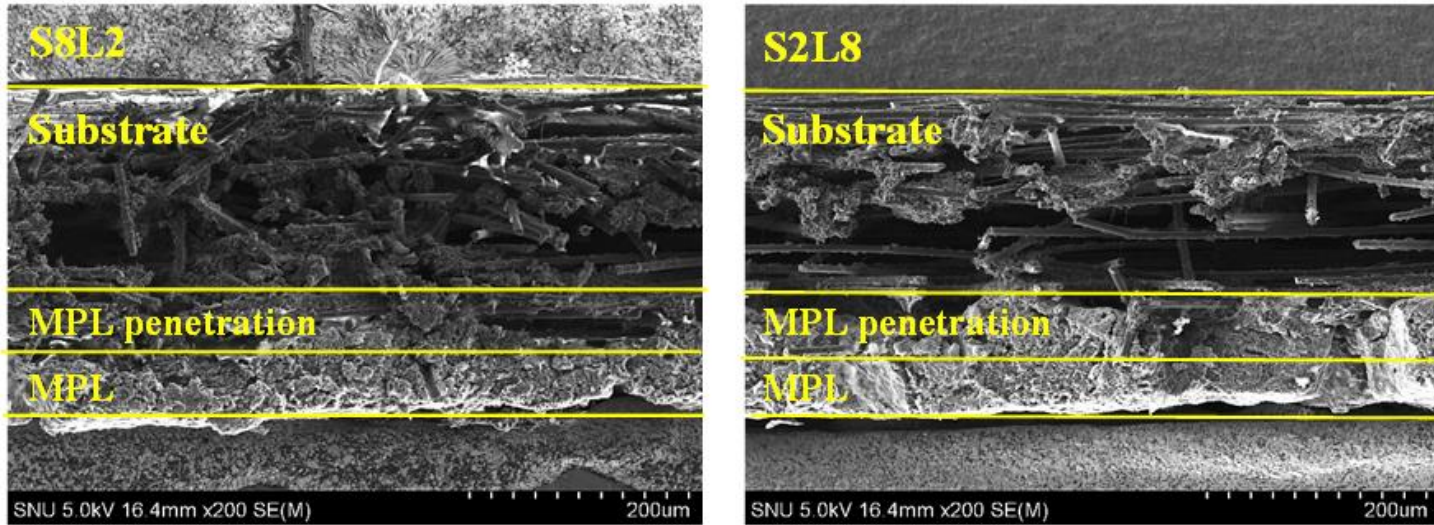


Figure 3.2 Cross-sectional images of S8L2 and S2L8: (a) S8L2 and (b) S2L8

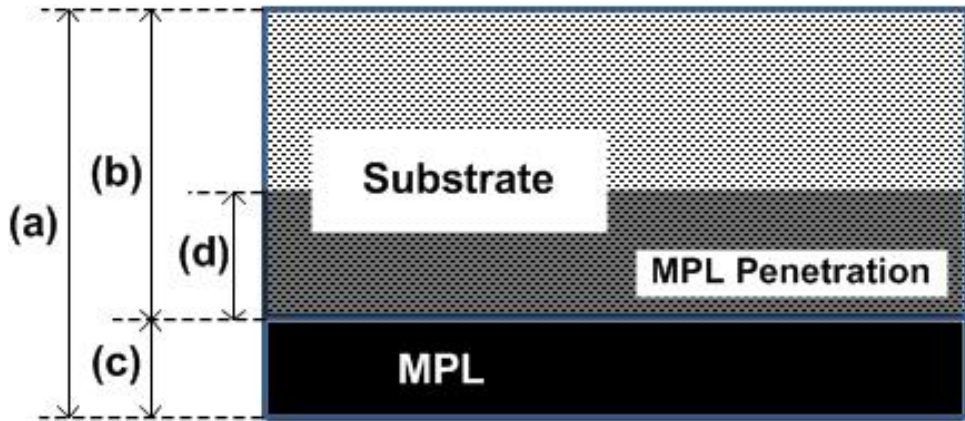


Figure 3.3 Schematic diagram cross-sectional structure of the GDL

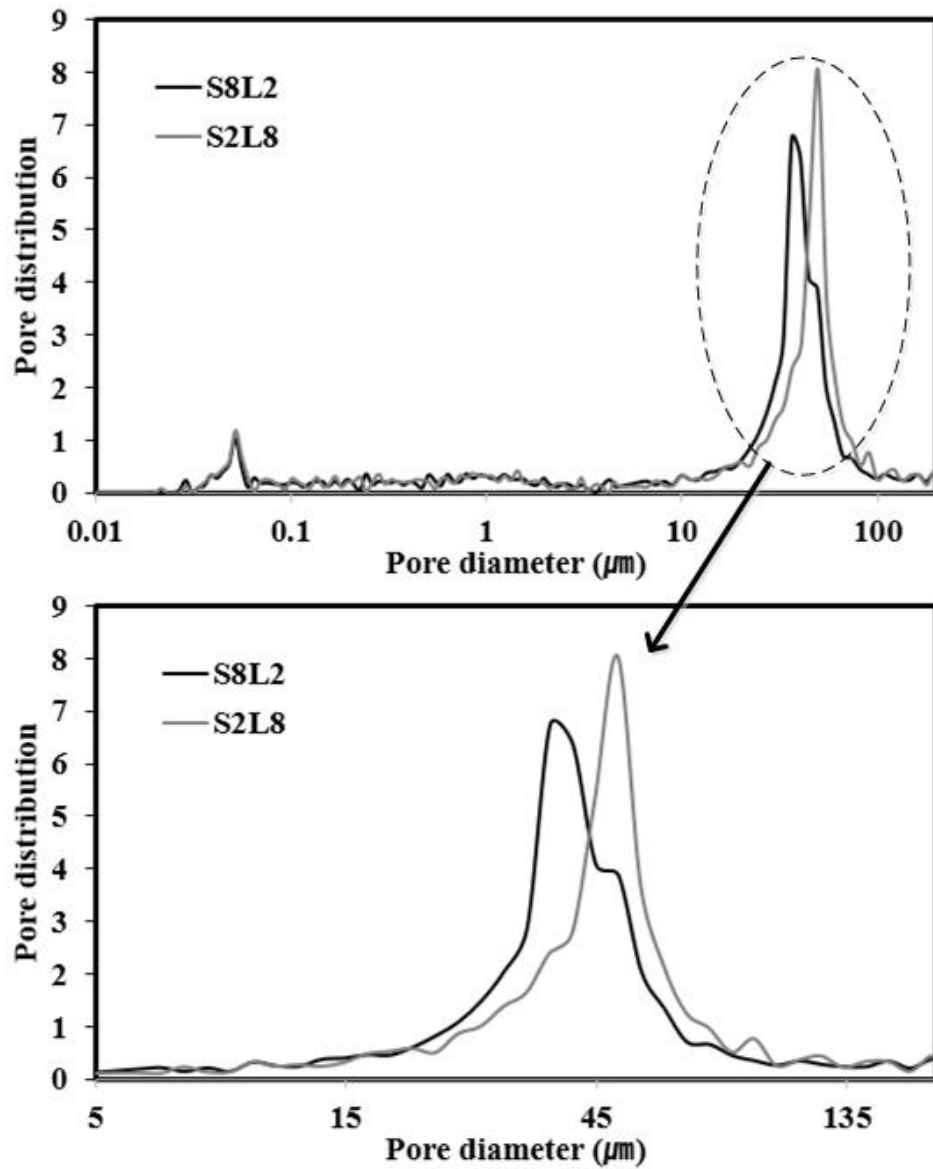


Figure 3.4 Pore size distribution of S8L2 and S2L8

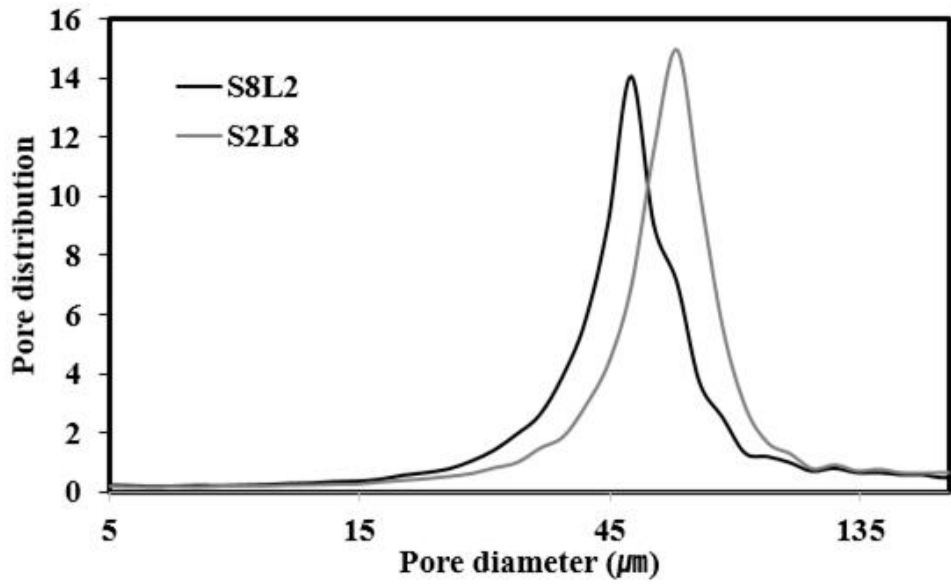


Figure 3.5 Pore size distribution of substrate only sample of S8L2 and S2L8

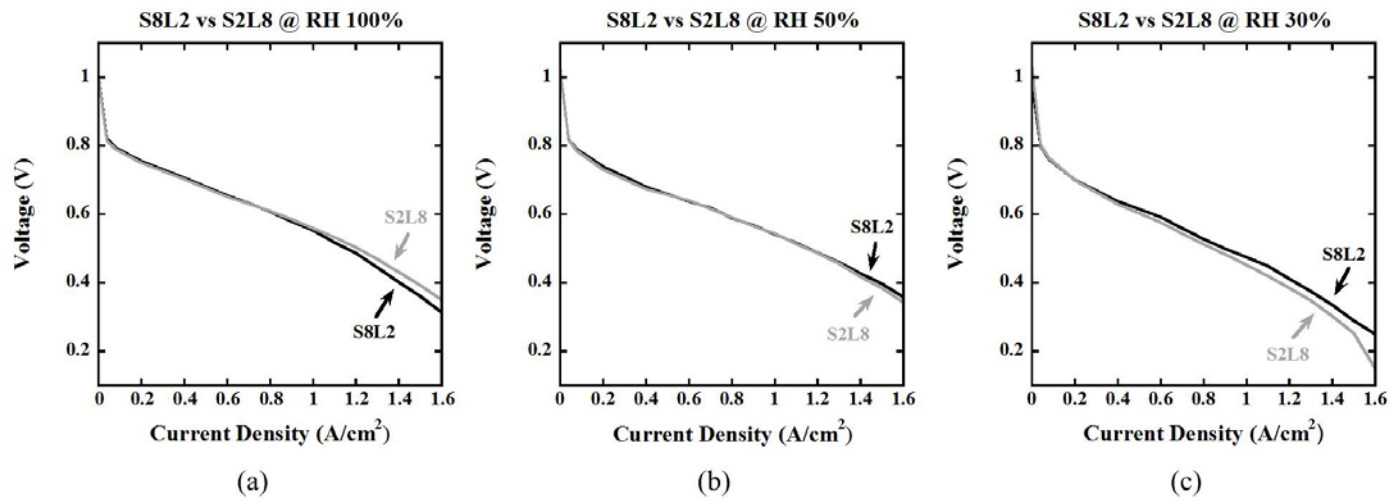


Figure 3.6 Steady-state performance of the S8L2 and S2L8: (a) at RH 100%, (b) at 50%, and (c) at 30%

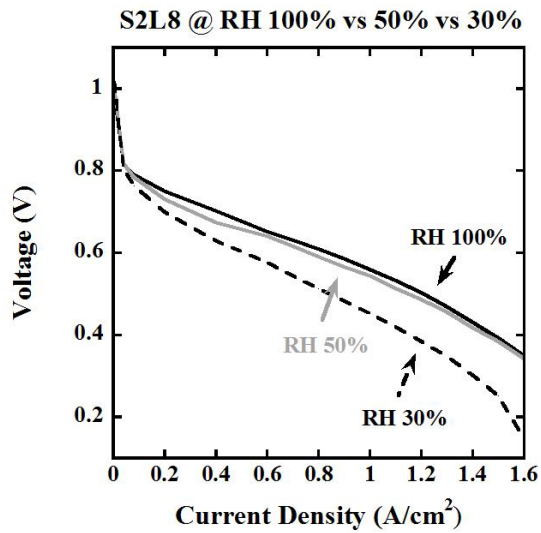
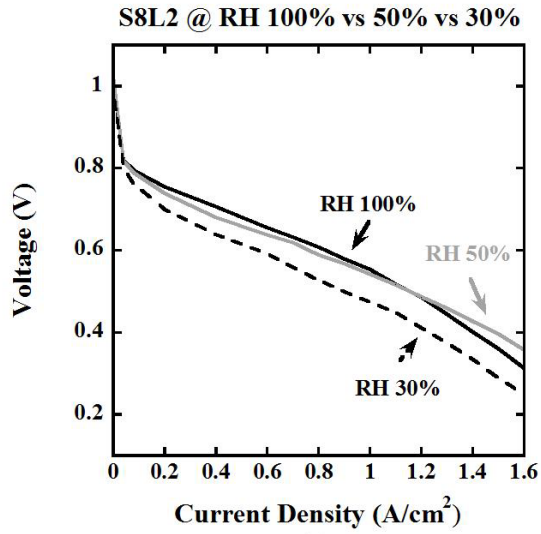


Figure 3.7 Comparison of steady-state performance of S8L2 and S2L8 at various humidification: (a) S8L2 and (b) S2L8

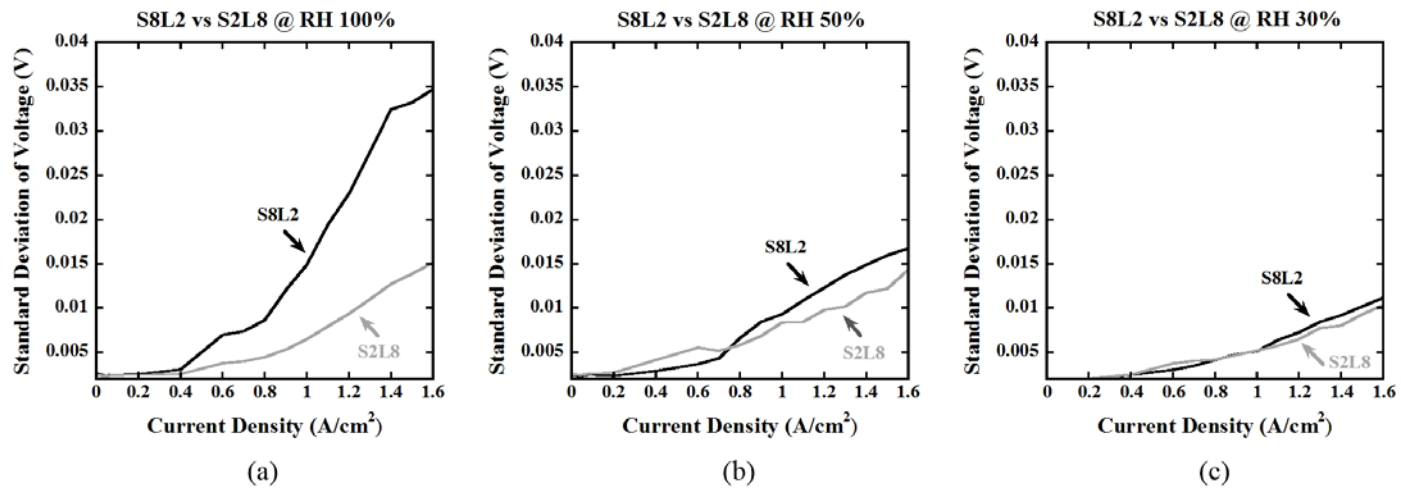


Figure 3.8 Comparison of standard deviation of voltage of S8L2 and S2L8: (a) at RH 100%, (b) at RH 50%, and (c) at RH 30%

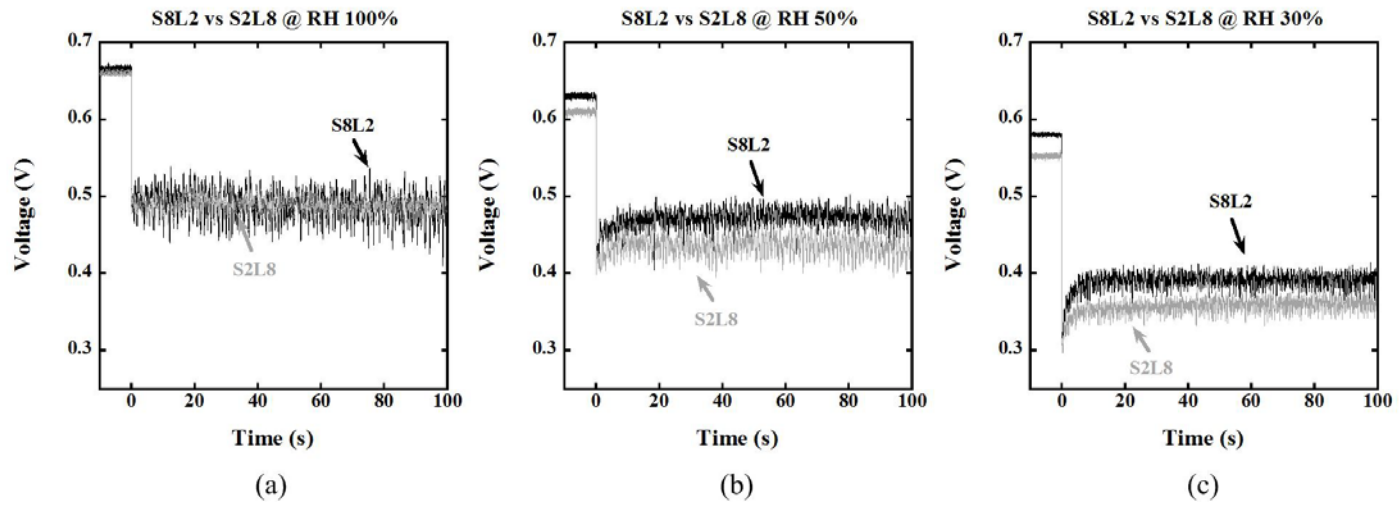


Figure 3.9 Comparison of transient response of S8L2 and S2L8: (a) at RH 100%, (b) at RH 50%, and (c) at RH 30%

Table 3.2 Thickness of each the GDL part of S8L2 and S2L8

Description		S8L2	S2L8
Thickness	MPL	51 μm	53 μm
	MPL penetration	58 μm	61 μm
	Substrate	254 μm	265 μm
	Pure substrate (No MPL penetrated region)	196 μm	204 μm
	Total	305 μm	318 μm

Table 3.3 Porosity and local porosities of S8L2 and S2L8

Description		S8L2	S2L8
Total porosity		71.0%	72.2%
Local porosity	MPL	4.9%	6.2%
	MPL penetration	10.4%	12.4%
	Pure Substrate (No MPL penetrated)	55.8%	54.2%
Local porosity with considering thickness ratio	MPL	29%	37%
	MPL penetration	54%	64%
	Pure Substrate (No MPL penetrated)	87%	85%

Table 3.4 Contact angles of S8L2 and S2L8

Description		S8L2	S2L8
Internal contact angle	Substrate	122.4°	126.6°
Surface contact angle	Substrate	138.0°	138.4°
	MPL	140.5°	
Assumed contact angle	MPL penetration	130°	

3.4 Simulation results

The simulation work is conducted to elucidate the experimental results for cell performance of S8L2 and S2L8. The simulation condition is the same as the experimental condition. In particular, the GDL geometry variables from the experimental results are applied. However, the cooling fan used in the experimental work is substituted with coolant channel in the model. The water coolant flow rate is fixed to 0.03 kg/s.

In the simulation work, the validation of simulation results of polarization curve with the experimental data and analysis of activation and ohmic overvoltage, liquid water saturation of the GDL, species mass transport according to water saturation, distributions of oxygen mole fraction, and membrane water content are conducted. The effect of the GDL structural characteristics on cell performance can be investigated with the simulation work.

3.4.1 Validation

Figure 3.10 shows the comparison of cell polarization curve between the experimental data and simulation results. The simulation results showed a good agreement with the experimental data of RH 100% and 50% conditions. Notably, there are some differences between the values of experimental data and simulation results of S8L2 at the high-load conditions over 1.2 A/cm². However, the mass transport loss behavior is well predicted. The averaged errors of the simulation results of S8L2 at RH 100% and 50% are 1.6% and 1.2%, respectively. In case of S2L8, the averaged errors are 0.8% and 1.2%, respectively.

3.4.2 Analysis with simulation results

Figure 3.11 shows the activation and ohmic overvoltage of S8L2 and S2L8 at RH 100% and 50% conditions. As expected in the experimental results, the mass transport loss which is included in the activation overvoltage, the value of S8L2 is higher than that of S2L8 at the high current density region. Generally, the mass transport loss is regarded as insignificant at low humidification. However, the water removal capability of S8L2 is insufficient so that the mass transport loss of high-load current region also increased under low humidification. These results verify the experimental results of the voltage instability as shown in Figure 3.8. In the results, the voltage instability of S8L2 under RH 50% condition is lower than that of S2L8 until 0.8 A/cm^2 . At the range over 0.8 A/cm^2 , however, the voltage instability of S8L2 is higher than that of S2L8 due to the increased mass transport loss.

The ohmic overvoltage of two samples at RH 100% had no differences due to highly hydrated membrane condition. However, the ohmic overvoltage of S8L2 is lower than that of S2L8 at the range over 1.2 A/cm^2 under RH 50%. At the low humidification, S8L2 held the water well and made the membrane hydrated, even though the electro-osmotic drag increased. The electro-osmotic drag makes the membrane to be dehydrated, and it increased according to the increment in load current. These results well illustrate the trade-off relationship between water removal and retention capability of the GDL which is described in the section 1.1.3.

The liquid water saturation of the GDL is also analyzed. The liquid water saturation is a representative index of the water management capability of the GDL. Figure 3.12 shows the liquid water saturation of S8L2 and S2L8 through the GDL thickness direction. The values of each GDL part are calculated by averaging the value of twenty nodes.

As shown in Figure 3.12, the averaged saturation value of the MPL and MPL penetration of S8L2 is 18.8% higher than that of S2L8 at RH 100%. Since the porosity of the MPL and MPL penetration of S8L2 is lower than that of S2L8, the liquid water saturation increased in these parts. The accumulated water in the MPL and MPL penetration of S8L2 hindered the mass diffusion from the bulk gas channel to the catalyst layer. It is confirmed by the results in Figure 3.13. The figure shows that the oxygen concentration of each GDL part at 1.6 A/cm² under RH 100%. As shown in the figure, the oxygen concentration between S8L2 and S2L8 is almost the same as in the substrate. From the MPL penetration to the catalyst layer, however, the oxygen concentration of S8L2 is much lowered than in S2L8 due to the increased liquid water saturation. This phenomenon is intensified with the increment in current as shown in Figure 3.14. The oxygen concentration of S8L2 at the catalyst layer is 56.2% lower than that of S2L8 at 1.6 A/cm². The activation overvoltage of S8L2 is increased according to the relevant equation (Equation 2.36) given the lower oxygen concentration and higher liquid water saturation at the catalyst layer. The local oxygen mole fraction is also affected by the increased liquid water saturation. Figure 3.15 shows the distribution of the oxygen mole fraction at RH 100%. At the current density of 1.6 A/cm², the S8L2 experienced the severe local starvation of oxygen throughout the cell, which is depicted in Figure 3.15 with dark blue areas, and the oxygen mole fraction is near 0.01. This result is consistent with the results of voltage instability of S8L2 (Figure 3.8) that is dramatically increased at the high-load current region.

In contrast, the capillary pressure gradient between the catalyst layer and MPL is lowered due to the increased saturation at the MPL and MPL penetration. Due to the lower driving force of liquid water transport induced from lowered capillary pressure gradient, the water saturation of S8L2 maintained higher than that of S2L8 at the catalyst layer. Moreover, the anode GDL of S8L2 also maintained higher water

concentration compared to that of S2L8. Figure 3.16 shows the water molar concentration through the anode GDL, MEA, and cathode GDL at RH 50% condition. The results of the S8L2 showed that the cathode GDL maintained higher water concentration than that of S2L8 at the cathode catalyst layer. Moreover, the results of S8L2 maintained higher water concentration at the anode catalyst layer, compared to that of the S2L8. Higher water concentration at the anode catalyst layer is advantageous to prevent membrane dehydration by stably supplying the water with electro-osmotic drag. This water retention capability of the S8L2 is advantageous under low humidification. Figure 3.17 shows the distribution of the membrane water content of S8L2 and S2L8 at RH 50%. As shown in the figure, the membrane water content is increased along the channel due to accumulation of the product water. However, the distribution of S2L8 had more dried area compared to the distribution of S8L2. This is the why S8L2 is advantageous at low humidification.

One remarkable thing in the results of liquid water saturation is that the saturation values at the substrate between S8L2 and S2L8 had no considerable differences. It means that the pore size variation between S8L2 and S2L8 does not significantly affect the liquid water transport in the substrate. Figure 3.18 shows the capillary pressure gradient in the substrate of S8L2 and S2L8 at RH 100%. The averaged capillary pressure gradient from the substrate 1 to 4 in control volumes of S8L2 is 8.4% higher than that of S2L8. However, such difference of capillary pressure gradient does not significantly affect liquid water saturation values at the substrate between S8L2 and S2L8. The averaged saturation value of the substrate of S8L2 is 2.3% higher than that of S2L8 at RH 100%. Consequently, the pore size variation in the substrate (e.g., 36.6 μm for S8L2 and 49.5 μm for S2L8) affects the liquid water behavior characteristics of the MPL and MPL penetration instead of changes in the characteristics of the substrate.

Through this chapter, the basic structural characteristics of two GDL's, which have different macro-pore sizes in the substrate, are analyzed. The structural parameters are evaluated with the experimental work, and are applied in the model to elucidate the experimental results, particularly, in regard to cell performance. The experimental results validate the model. It is confirmed that the model can reflect the structural characteristics of the GDL and predict its effect on the cell performance. It is concluded from both the experimental and simulation work, that the large macro-pores in the substrate formed the MPL penetration and the MPL part coarsely. In contrast, the small macro-pores in the substrate formed the MPL penetration and the MPL part densely, as evaluated with porosimetry analysis. The characteristics of the MPL penetration and MPL affected by variation in macro-pore size of the substrate, indicate that the water management capability of the GDL is balanced between the water retention and removal characteristics. Additionally, the cell performance is affected according to operating conditions of relative humidity and current load.

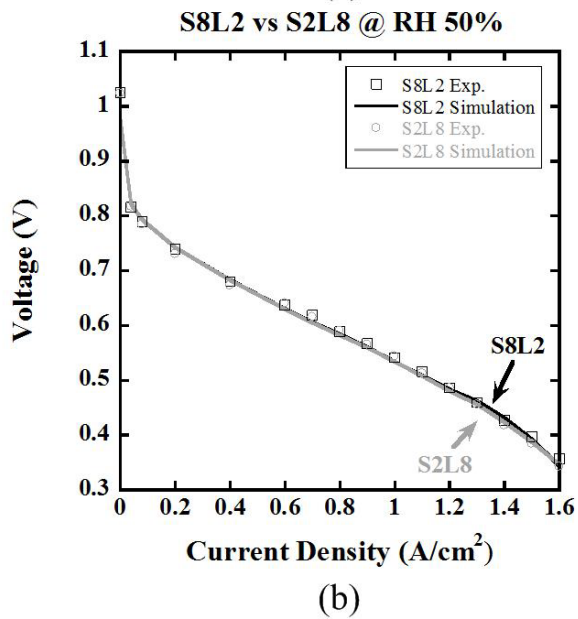
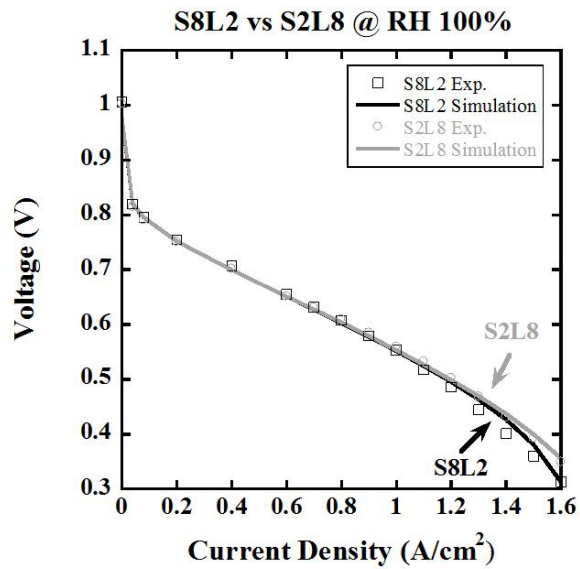


Figure 3.10 Validation of simulation results of S8L2 and S2L8: (a) at RH 100% and (b) RH 50%

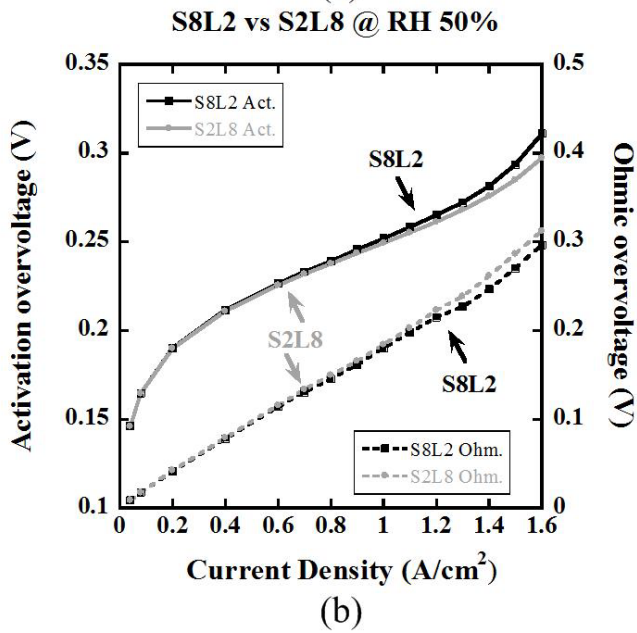
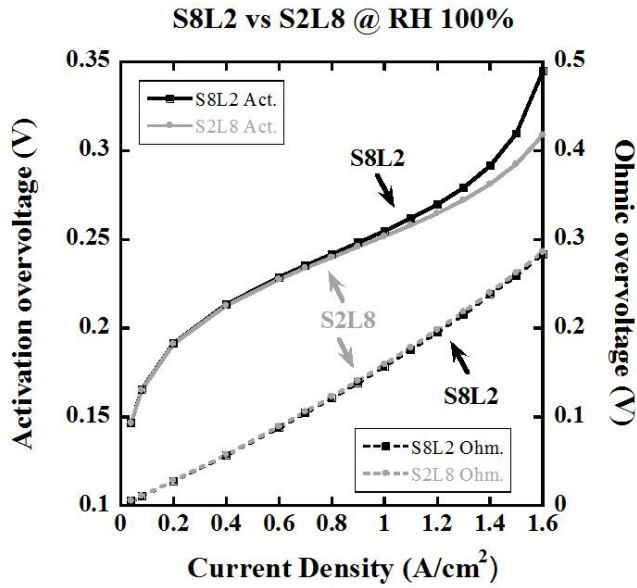


Figure 3.11 Overvoltages of S8L2 and S2L8: (a) at RH 100% and (b) at RH 50%

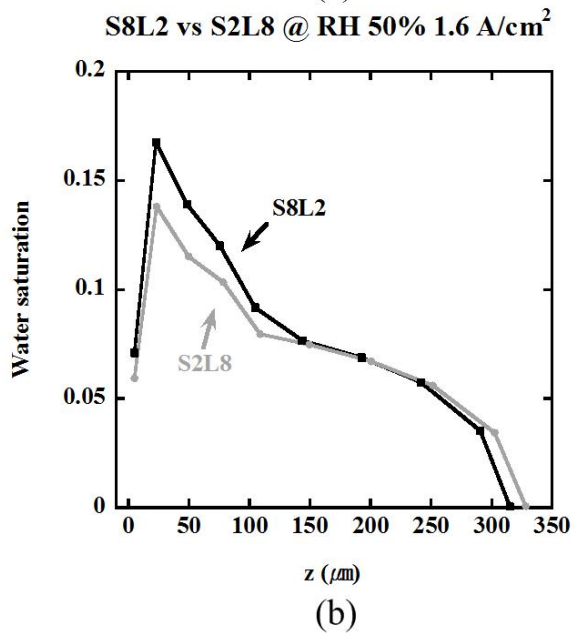
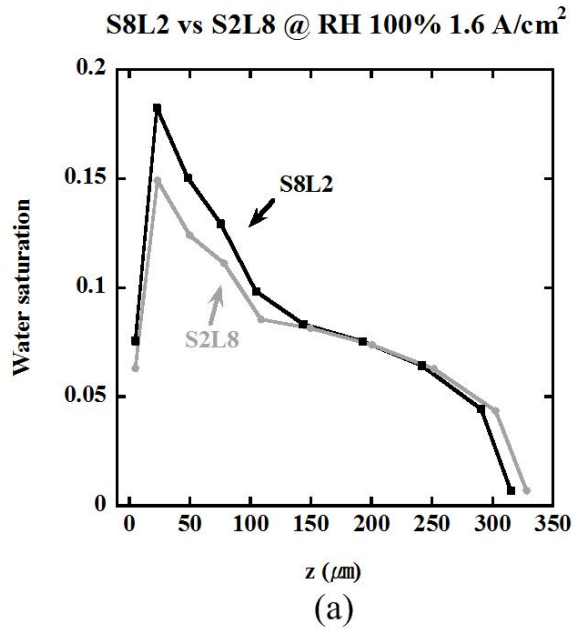


Figure 3.12 Liquid water saturation along the GDL thickness of S8L2 and S2L8 at 1.6 A/cm²: (a) at RH 100% and (b) at RH 50%

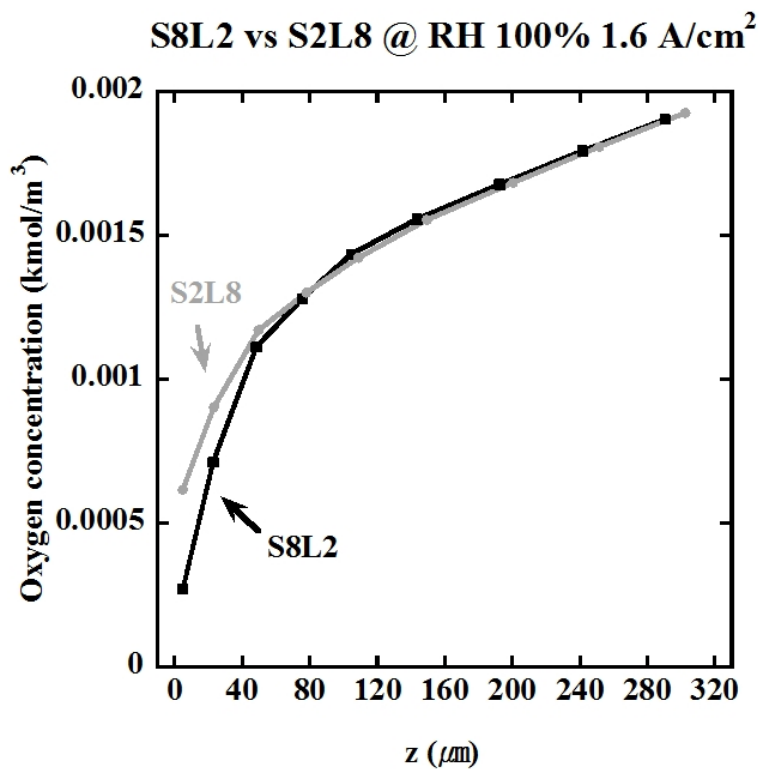


Figure 3.13 Oxygen concentration of S8L2 and S2L8 along the GDL thickness

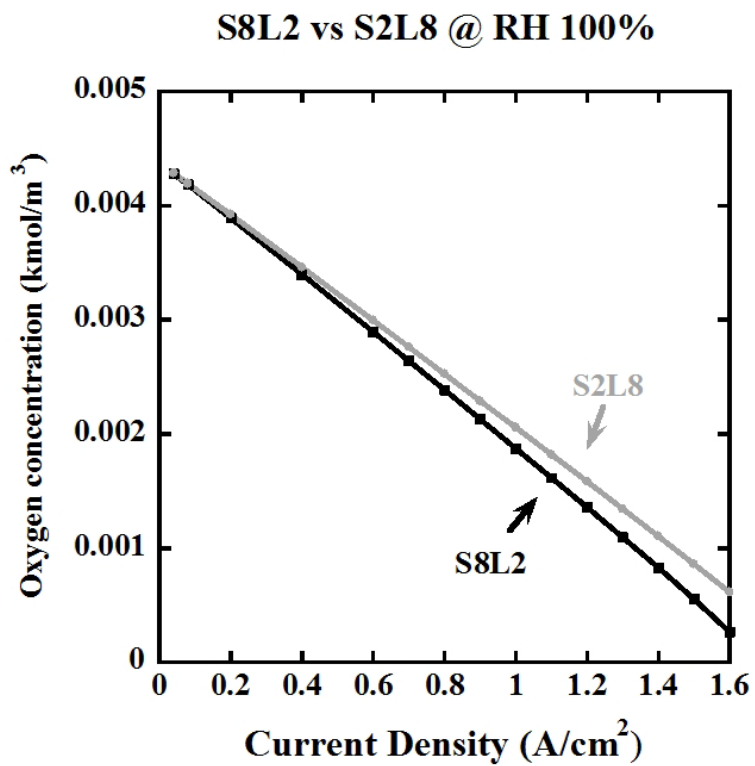
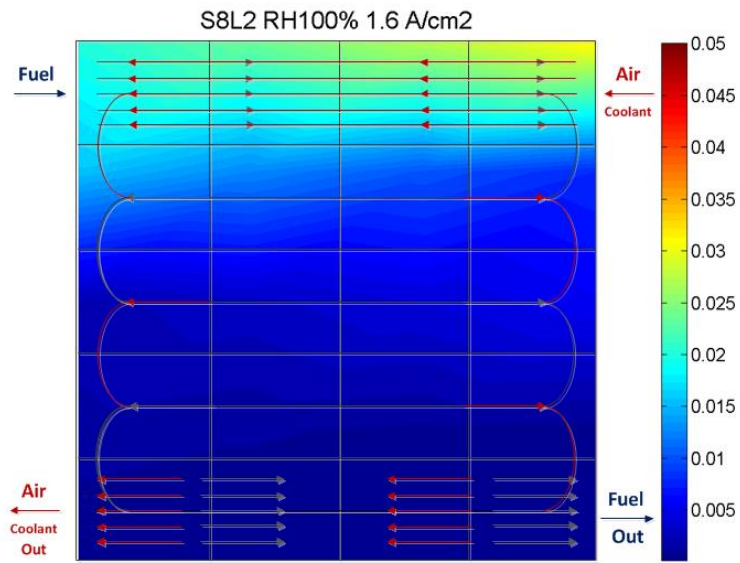
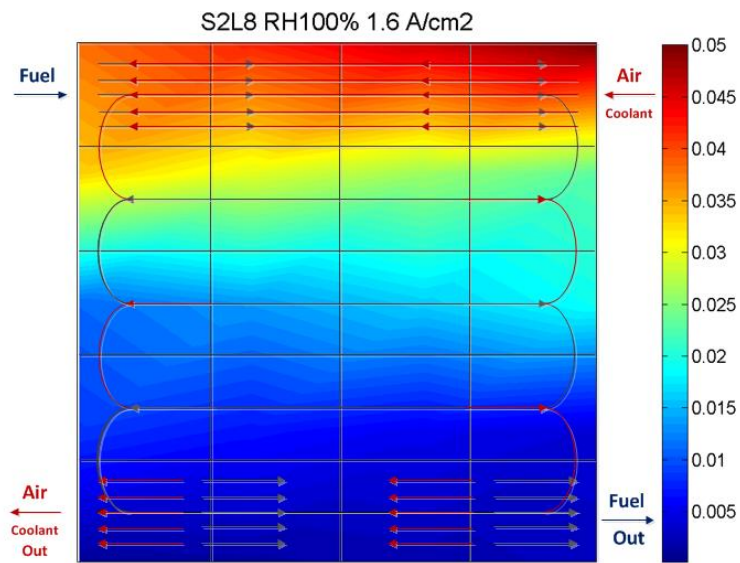


Figure 3.14 Oxygen concentration of S8L2 and S2L8 according to current density



(a)



(b)

Figure 3.15 Distribution of oxygen mole fraction of S8L2 and S2L8 at RH 100%:

(a) S8L2 and (b) S2L8

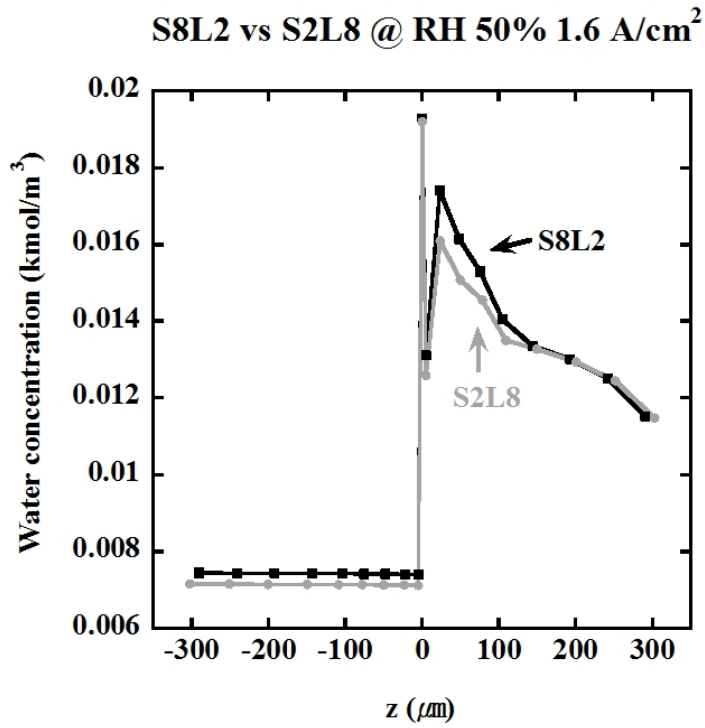


Figure 3.16 Water concentration of S8L2 and S2L8 along the anode GDL, MEA, and cathode GDL

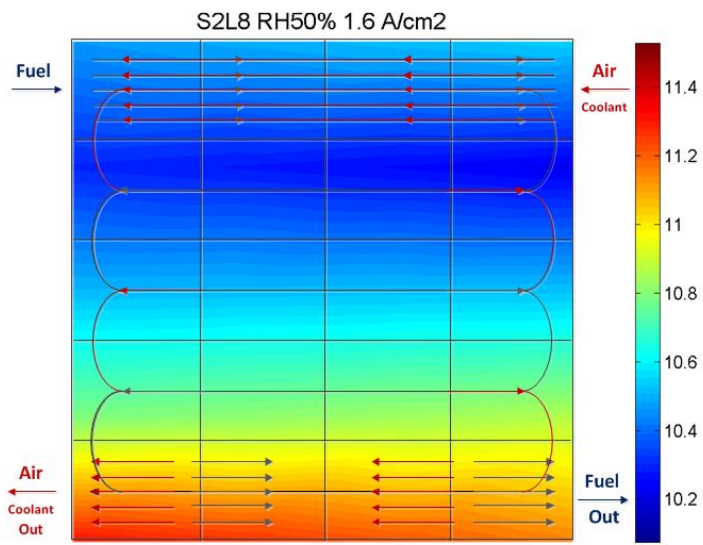
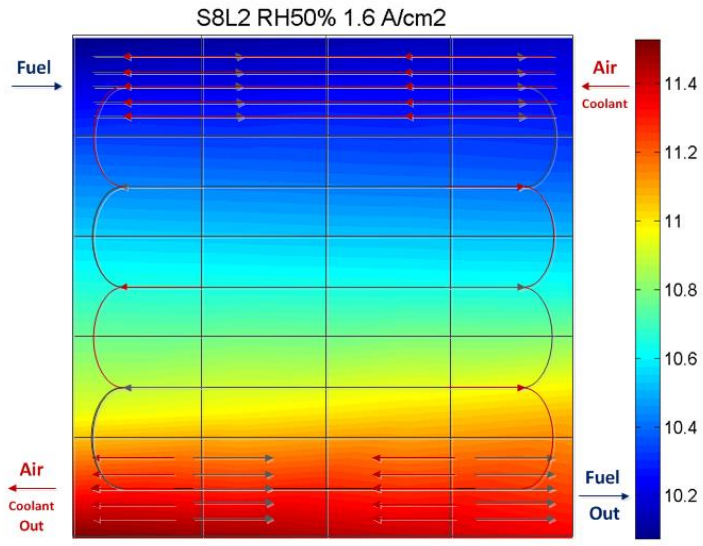


Figure 3.17 Distribution of membrane water content of S8L2 and S2L8 at RH 50%:
 (a) S8L2 an (b) S2L8

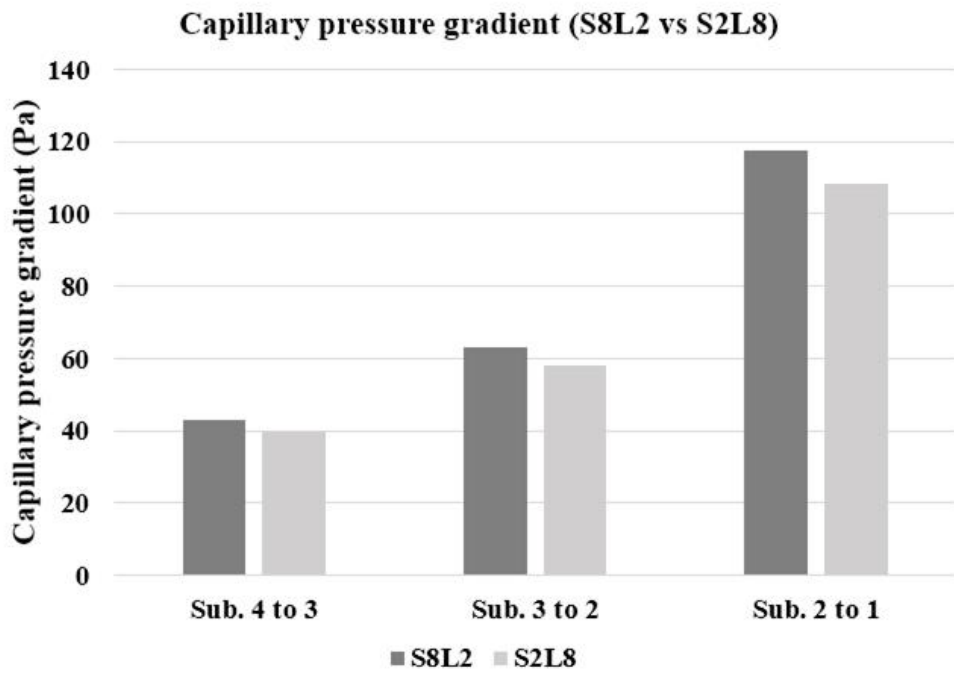


Figure 3.18 Capillary pressure gradient of S8L2 and S2L8 along the substrate at RH 100%

Chapter 4. Effect of in-plane structure design of the GDL on water management and cell performance

Fuel cell performance generally is not uniform throughout the cell. The current density distribution is affected by; the stoichiometric ratio of the hydrogen and oxygen in the air, humidification, the microstructure of the diffusion media, and the flow field design [96]. Since the parameters do not have uniform distribution throughout the cell, this induces non-uniform current density distribution. The non-uniform current density distribution causes; lower catalyst utilization, lower energy efficiency, and reduced durability of the cell [97]. Fuel cells are operated under conditions of heat and humidity that exigently entails non-uniform operation, which causes local variation in thermal stress and consequential degradation of the MEA. This results in reduced durability of the cell, therefore, uniform operation of the cell is required and many attempts to enhance the uniformity of the current density distribution are reported [97-100]. The representative attempt is to optimize the flow channel configuration and layouts [83, 101-103]. However, the previous researches are only focused on just discharging the saturated water in the channel. It is a passive way of water management since the operating cell needs to contain a proper amount of water in the cell. Therefore, water management in an active way with the simultaneous water retention and removal characteristics should be suggested to enhance the uniformity of current density distribution.

To enhance the uniformity of current density distribution, the effect of in-plane structure design of the GDL is investigated in this chapter. The cathode gas channel inlet is prone to dry with the parallel serpentine flow channel geometry because the

amount of water produced near cathode inlet is not sufficient to saturate the GDL. Back diffusion from the cathode to anode is less than the electro-osmotic drag from the anode to cathode, and results in membrane dehydration near the cathode inlet. In contrast, the water concentration is gradually increased along the channel with accumulation of the produced water and the region near the cathode outlet is prone to saturation. The proper amount of water in the cathode is helpful to maintain the membrane hydration, especially, at a sudden increase in load current, however, excessive water caused flooding phenomenon and an increase of the mass transport loss. Under these conditions, the cell experiences local mass imbalance so that the current density distribution is not uniform. To improve the uniformity of mass balance with uniform current density distribution, the GDL near the cathode inlet is required to have the liquid water retention. Also, the GDL, near the cathode outlet is required to have the capability to remove water. However, the GDL has a trade-off relationship between water retention and removal. It is not possible to have both abilities locally with a single GDL. Therefore, the in-plane structure design of the GDL is introduced, which has local water retention and removal capability simultaneously.

The objective of this chapter is to analyze the effect of in-plane structure design of the GDL on the water management and cell performance. To investigate the effect of in-plane structure design, the simulation work analyses four GDL combinations with two different GDL's. Out of them, the best combination case is confirmed. After the simulation work, the experimental work of the combined GDL is performed and the simulation work is validated.

The potentials of in-plane structure design of the GDL are thereby investigated, and the ideal GDL structure which has improved water management capability is determined.

4.1 Design of the GDL

The basic concept of in-plane structure design of the GDL is a combination of different two types of GDL's that have water retention and removal capabilities, respectively. In the previous chapter, it is determined that the S8L2 has the water retention capability and S2L8 has the water removal capability with different pore size in the substrate., The GDL comprised of these two GDL's has the desired, local water management properties, however, correct identification of the dry and wet areas of the cell is prerequisite to the design of the in-plane structure design of the GDL. Comparatively, the channel inlet region is dry due to the increased electro-osmotic drag and the decreased back diffusion to the membrane, while, the channel outlet region is wet due to water accumulation along the gas channel. Four combinations are used in this study with S8L2 near the cathode inlet and S2L8 near the cathode outlet.

Figure 4.1 shows the four combinations. Based on the 25 cm² square cell with the four-step parallel serpentine channel geometry, the area portion of S8L2 is increased by 20%, 40%, 60%, and 80% from the channel inlet. Conversely, the area portion of S2L8 for four combination cases from the channel outlet are 20%, 40%, 60%, and 80%, respectively. To refer each GDL combination in a simple way, the notations of "1-4", "2-3", "3-2", and "4-1" which mean the portion of S8L2 and S2L8 will be used in this study. According to the composition of each GDL, the combined GDL's have different local water management capabilities. It is expected that 1-4 has the emphasized water removal capability and 4-1 has the emphasized water retention capability, while 2-3 and 3-2 have the medium characteristics of water retention and removal capability.

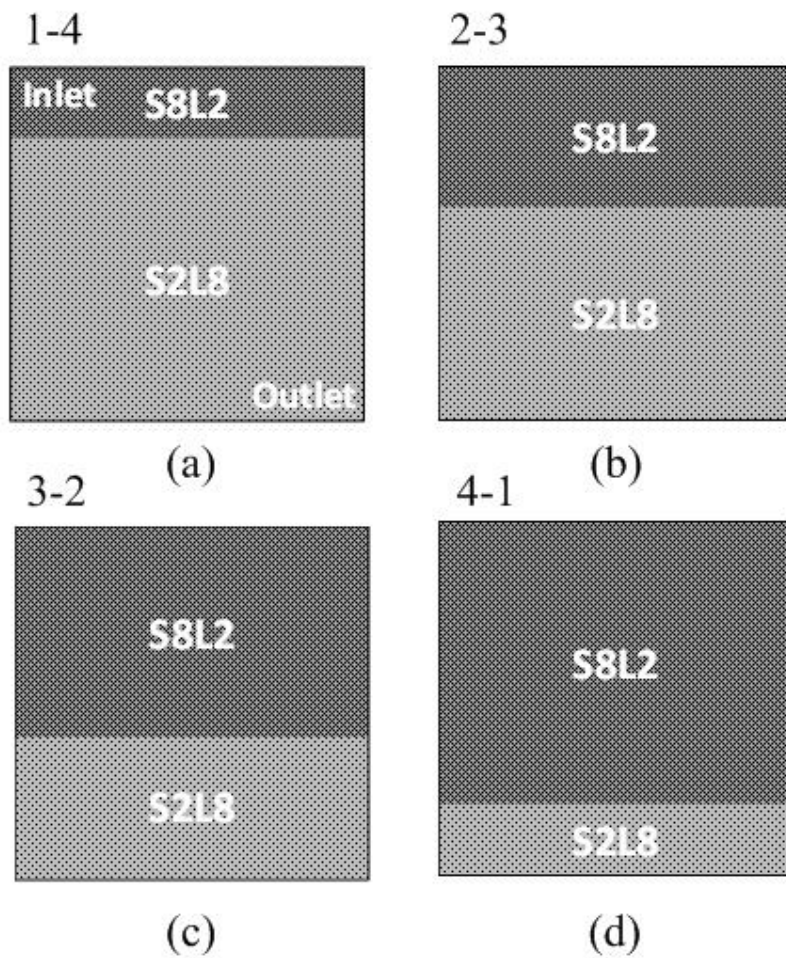


Figure 4.1 Design of four combinations of the GDL: (a) 1-4 of S8L2 20% and S2L8 80%, (b) 2-3 of S8L2 40% and S2L8 60%, (c) 3-2 of S8L2 60% and S2L8 40%, and (d) 4-1 of S8L2 80% and S2L8 20%

4.2 Analysis with simulation results

To clarify the effect of four combination cases on water management and cell performance, the simulation work is conducted. Since the model has twenty nodes, each GDL characteristics of S8L2 and S2L8 is applied to corresponding nodes according to the combination cases. For example, in case of 2-3, from the node 1 to 8 are applied to the characteristics of S8L2 and from node 9 to 20 are adopted the characteristics of S2L8.

The high current density region of the GDL at the catalyst layer where there is high water production and saturation is focal for determining the water management capability of the GDL. Thus, the water balance inside the GDL affects cell performance significantly at the high current density region. In this simulation work, the current density of 1.6 A/cm² case is investigated for all combined GDL cases without consideration of the whole operating range of the polarization curve.

Firstly, the cell voltage, activation overvoltage, and ohmic overvoltage are analyzed. Figure 4.2 shows the results of the cell voltage and overvoltage at RH 100% and 50% conditions.

In pursuit of improvement, the cell voltage and overvoltages of four combined GDL's at RH 100% are compared to the simulation results for S8L2, which is disadvantageous at RH 100%. Basically, the ohmic overvoltage of all combined GDL cases are slightly decreased compared to S8L2. Although the combined GDL's include S2L8, which has water removal capability that causes membrane dehydration, ohmic overvoltages are not affected significantly due to high humidification. Nevertheless, uniformity of membrane water content is improved in combined GDL's so that ohmic overvoltages are improved. These improvements will be elucidated with the results of

distribution of membrane water content of Figure 4.4 in below. The activation overvoltage of combination cases decreased as the portion of S2L8 increases. When the portion of S8L2 is greater than 60% from channel inlet, the activation overvoltage increased sharply with hindering mass transport through the GDL. Therefore, the combinations of 1-4 and 2-3 are advantageous at RH 100%.

In case of RH 50%, the voltage and overvoltages of combined GDL's are compared to the results of S2L8, which is disadvantageous at RH 50%. The ohmic overvoltage is decreased as the portion of S8L2 increases and showed the lowest value at 3-2 case. Then, it is increased when the portion of S8L2 is greater than 80% from channel inlet. It means the water retention capability is effective when S8L2 is located at the dry area of the cell. Specifically, when S8L2 is located in the region of high accumulated water concentration, the distribution of membrane water content becomes non-uniform and causes increased ohmic overvoltage. The activation overvoltage is increased as the portion of S8L2 increases. Especially, when the portion of S8L2 is greater than 60%, the activation overvoltage is higher than that of S2L8 because the area contained a high portion of accumulated water concentration that resulted in an increase of mass transport loss. The activation overvoltage of 1-4 and 2-3 are the same. Additionally, activation and ohmic overvoltage are almost the same level in 4-1 case.

Figure 4.3 shows the liquid water saturation of combinations of the GDL. The averaged liquid water saturation is increased as the portion of S8L2 increases at the MPL and MPL penetration region. These data support the results of cell voltage and overvoltages of the GDL combinations. For example, the result of increase in activation overvoltage at RH 100%, when the portion of S8L2 is greater than 60%, is due to the increase of liquid water saturation at the MPL and MPL penetration region, which affects the mass transport through the GDL. Consequently, the averaged

characteristics of the combined GDL follows the basic GDL characteristics of S8L2 and S2L8 according to the portion of each base GDL.

In addition to the basic characteristics of the combined GDL's, the local characteristics are also analyzed to determine the uniformity of current density distribution. Figure 4.4 shows the distribution of membrane water content of the combined GDL's at RH 50%. As the portion of S8L2 increases, the dry area decreased but a significant difference is not captured between the 2-3 and 3-2. The 1-4 had the largest dry area among the combined GDL's. One remarkable thing in the results of 1-4 is that the lowest membrane water content is not located on channel inlet. In other words, the membrane water content is improved with the water retention capability of S8L2 near the channel inlet. Away from the S8L2 along the channel, however, water retention decreased with the water removal capability of S2L8. In contrast, other combined GDL's showed the lowest membrane water content at the start of channel inlet and it is continuously increased along the channel. These results correlate with the results of ohmic overvoltage of combinations at RH 50% as shown in Figure 4.2.

Figure 4.5 shows the distribution of the oxygen mole fraction of combinations GDL's at RH 100%. As shown in the figure, the local starvation area is increased as the portion of S8L2 increases. Especially, when the portion of S8L2 is greater than 40%, the area where the oxygen mole fraction is near 0.01 occupied 80% of the whole cell. This result caused the increased activation overvoltage of 3-2 and 4-1 compared to other combinations of GDL's. The current density distribution is affected by the influence of the local characteristics of oxygen mole fraction as well as the local characteristics of the membrane water content.

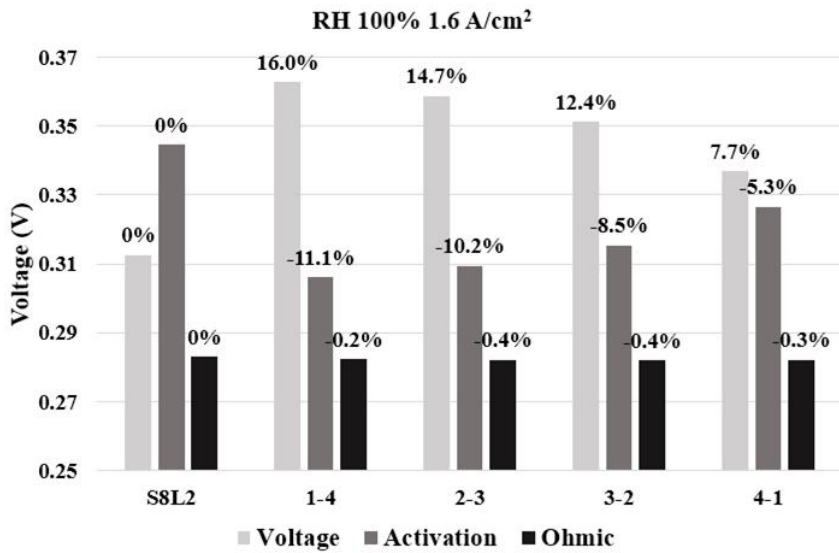
Figures 4.6 and 4.7 show the current density distribution of combinations of the GDL under RH 50% and 100%, respectively. As shown in Figure 4.6, the uniformity

of current density distribution seems to be higher with 2-3 and 3-2 combinations than 1-4 and 4-1 combinations in case of RH 50%. Specially, there are local current densities greater than 1.7 A/cm^2 in the results of 1-4 and 4-1 combinations, even though the operating condition of load current density is 1.6 A/cm^2 . Under this non-uniform operating condition, the thermal stress can concentrate focally, and degrade the durability of cell.

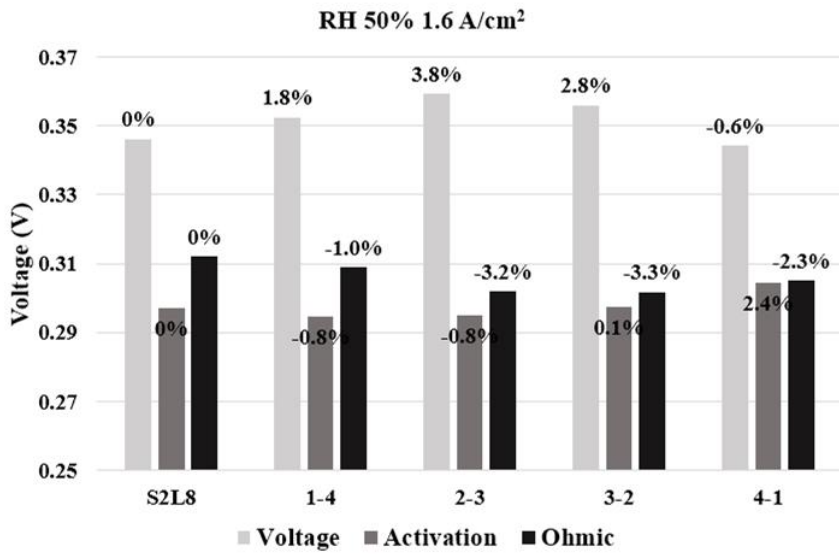
Furthermore, uneven current density distribution affects the activation overvoltage. The activation overvoltage of 1-4 is not improved compared to that of 2-3 at RH 50% even though the water removal capability increased as the portion of S2L8 increases. From Equation (2.37), the local activation overvoltage is also affected by not only local oxygen concentration at the catalyst layer but also by the local current density. Therefore, locally high current density caused increase of the activation overvoltage in case of 1-4 combination. This is why the activation overvoltage of 1-4 is not improved compared to that of 2-3.

As shown in Figure 4.7, the uniformity of current density distribution of the 1-4 and 2-3 combinations seems to be higher than that of 3-2 and 4-1 combinations in case of RH 100%. However, estimating of the uniformity of current density distribution is not conclusive from the figures. Thus, the standard deviation of the local current density is analyzed. As shown in Figure 4.8, the standard deviation value of 2-3 is the lowest among the combinations at RH 100%. In case of RH 50%, 3-2 had the lowest standard deviation value, and this indicates that the combination of 2-3 and 3-2 had the most uniform current density distribution among combinations of the GDL. Except for the 4-1 combination at RH 100%, the standard deviation of the local current density of all combinations with the in-plane GDL structure design is lower than a single layer GDL of S8L2 and S2L8. Consequently, as intended in this study, the in-plane GDL structure design had an effect of making the current density distribution

uniformly. Furthermore, this is the most suitable combinations of in-plane GDL structure design for enhanced cell performance, under the operating conditions.



(a)



(b)

Figure 4.2 Voltage and overvoltages of combinations of the GDL at 1.6 A/cm²: (a) at RH 100% and (b) at RH 50%

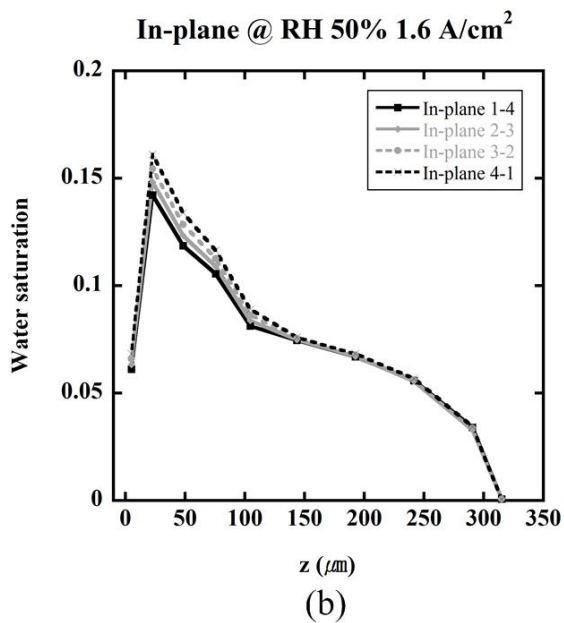
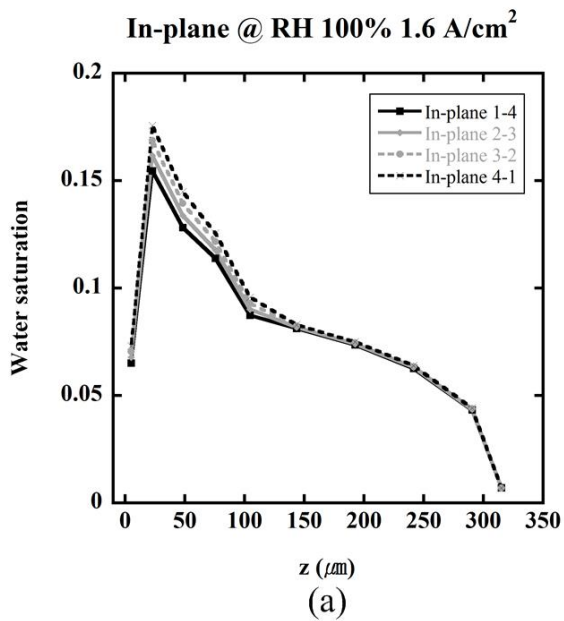


Figure 4.3 Liquid water saturation of combinations of the GDL at 1.6 A/cm²: (a) at RH 100% and (b) at RH 50%

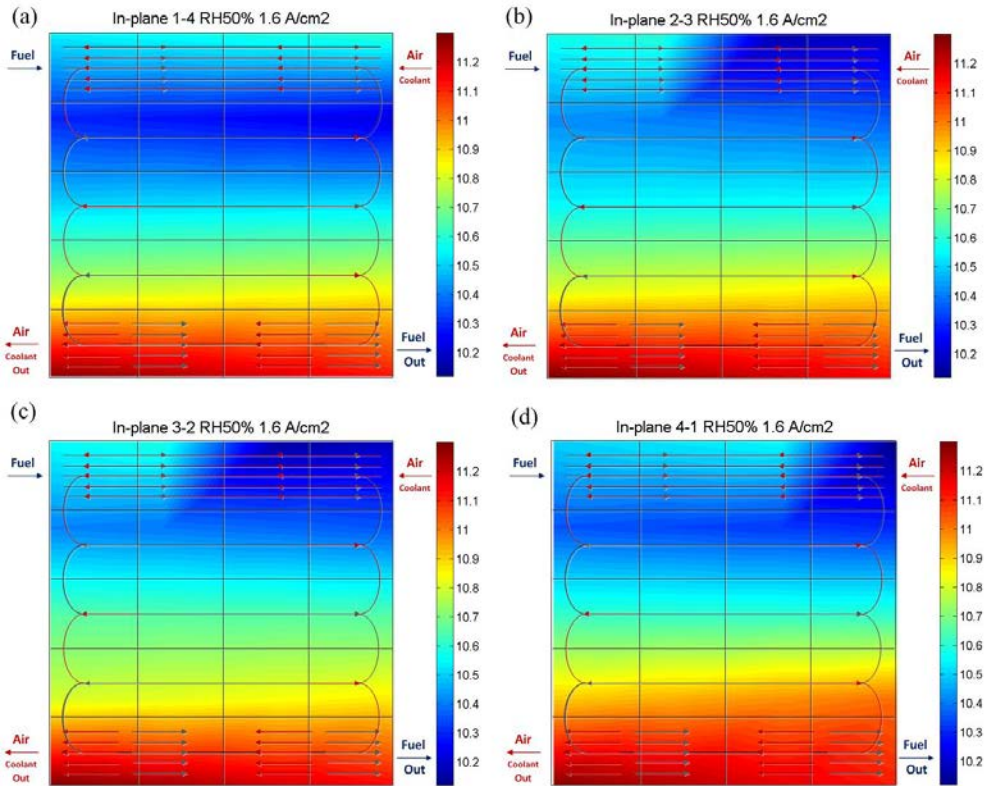


Figure 4.4 Distributions of membrane water content at RH 50%: (a) combinations of 1-4, (b) combinations of 2-3, (c) combinations of 3-2, and (d) combinations of 4-1

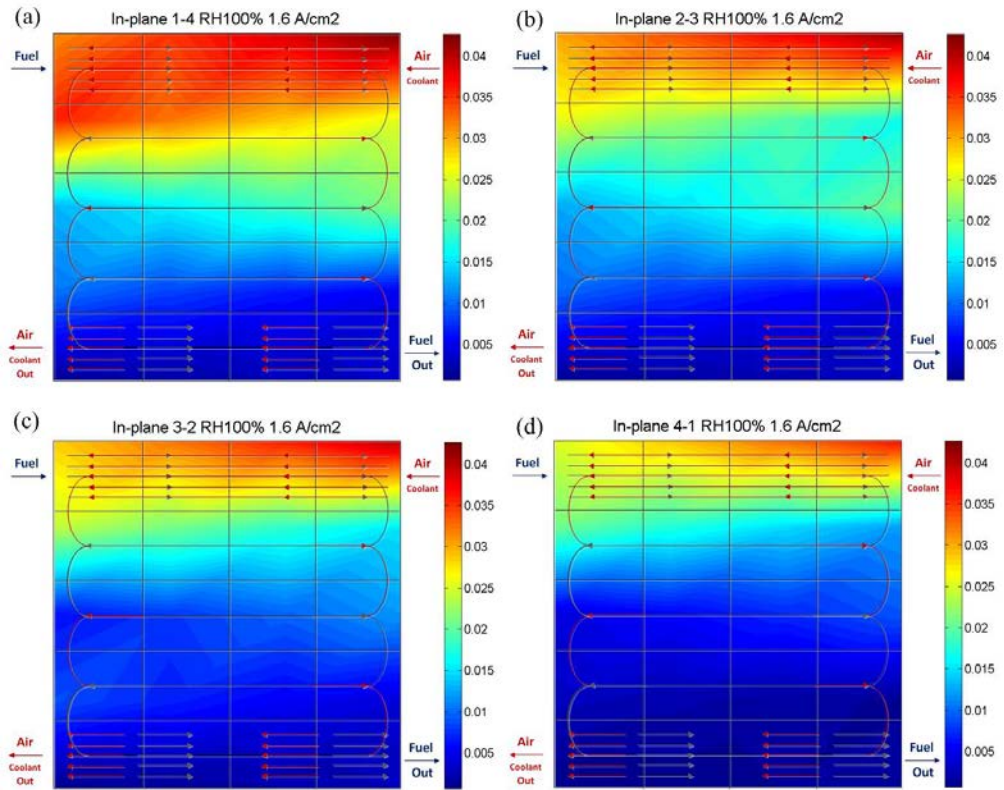


Figure 4.5 Distributions of oxygen mole fraction at RH 100%: (a) combinations of 1-4, (b) combinations of 2-3, (c) combinations of 3-2, and (d) combinations of 4-1

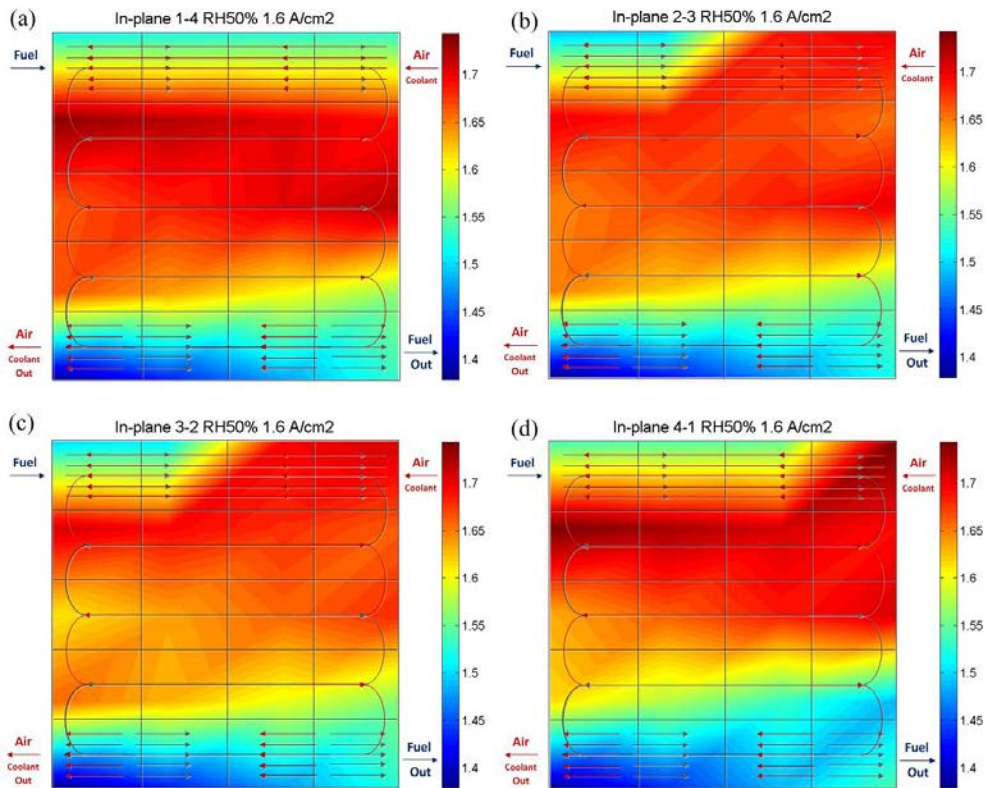


Figure 4.6 Distributions of current density at RH 50%: (a) combinations of 1-4, (b) combinations of 2-3, (c) combinations of 3-2, and (d) combinations of 4-1

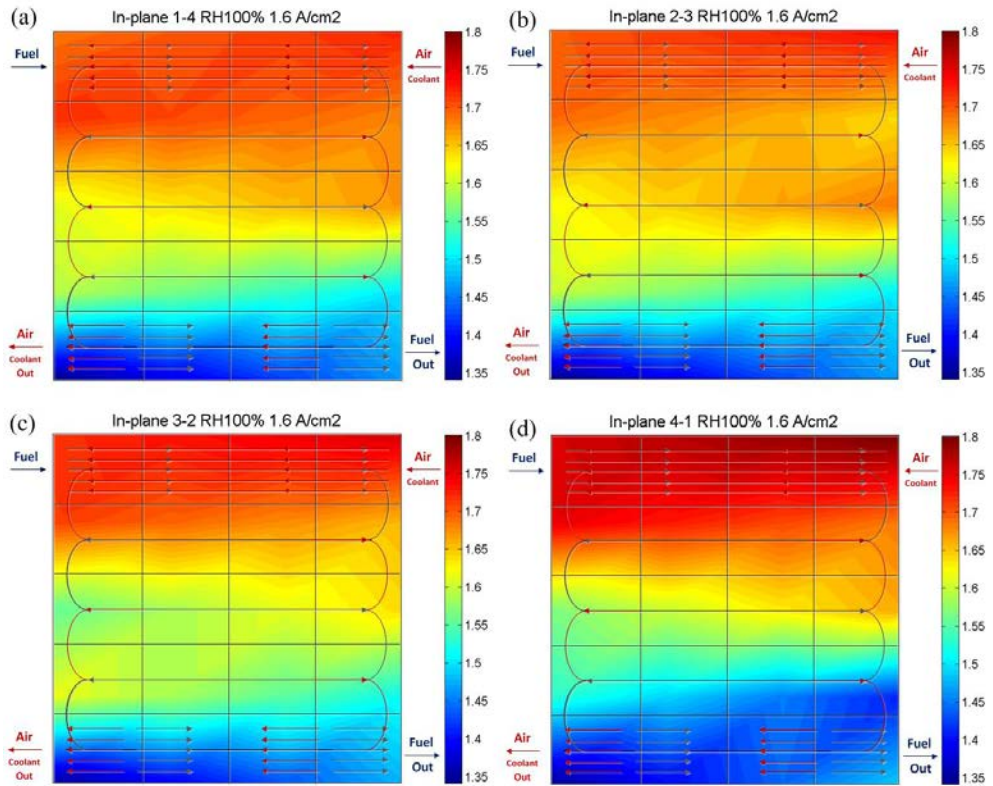


Figure 4.7 Distributions of current density at RH 100%: (a) combinations of 1-4, (b) combinations of 2-3, (c) combinations of 3-2, and (d) combinations of 4-1

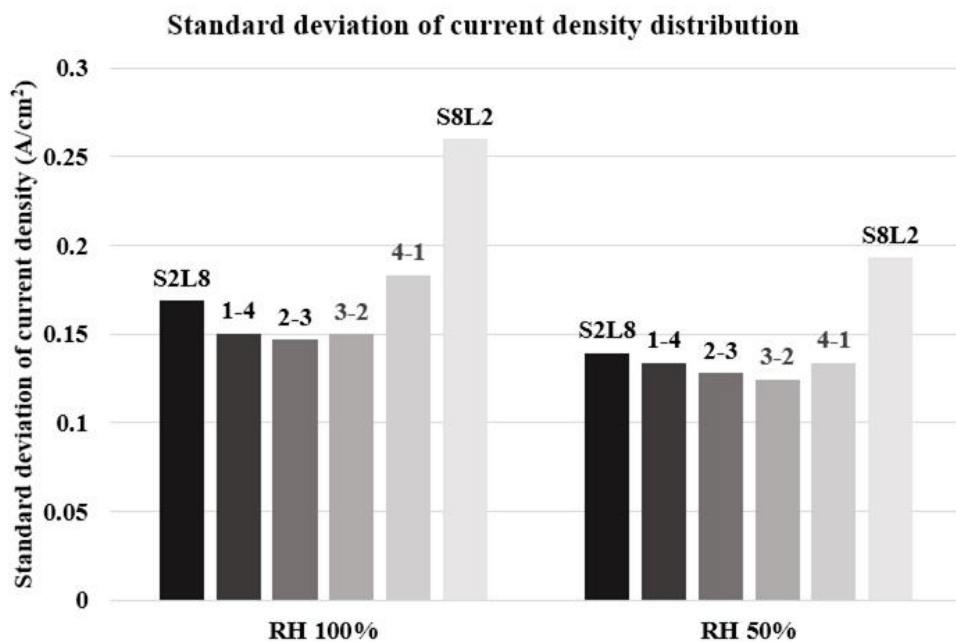


Figure 4.8 Standard deviation of current density distribution of combinations of the GDL

4.3 Verification of the effect of in-plane structure design with experimental results

The combination of 2-3 with the simulation work shows the efficient performance at the both RH 100% and 50%. It had improved cell voltage, including, overvoltages and uniformity of current density distribution. In this study, therefore, the effect of combination of 2-3 is verified with the experimental work. Figure 4.9 shows the experimental design. The size of S8L2 is $2.3 \times 5.6 \text{ cm}^2$ and that of S2L8 is $3.3 \times 5.6 \text{ cm}^2$. The combination of two samples ($5.6 \times 5.6 \text{ cm}^2$) stands for both anode and cathode GDL's which are used for the 25 cm^2 square unit cell experiment. For the sample development, the samples are arranged with S8L2 near the channel inlet and S2L8 near the channel outlet. The operating conditions are the same as the experimental work with single GDL of S8L2 and S2L8.

Figure 4.10 shows the steady-state cell performance of 2-3 with the simulation results. The simulation results showed a good agreement with the experimental data at both RH 100% and 50% conditions. The averaged errors of the simulation results of 2-3 at RH 100% and 50% are 1.5% and 1.0%, respectively. From the results, the developed model is validated, demonstrating that it is possible to predict the local characteristics of the GDL and the effect of local characteristics on water management and cell performance.

Figure 4.11 shows the comparison of cell performance among S8L2, S2L8, and 2-3 at RH 100%, 50%, and 30%. From the results, the performance of 2-3 shows the best performance at RH 100%. The cell voltage of 2-3 at 1.6 A/cm^2 is 2.7% higher than that of S2L8 and 14.4% higher than that of S8L2. In the case of RH 50% condition, the cell voltage of 2-3 at 1.6 A/cm^2 is 1.3% lower than that of S8L2 and

2.9% higher than that of S2L8. These results indicate that the performance characteristics of combination of 2-3 is similar with those of S2L8 at RH 100% and those of S8L2 at RH 50%. Figure 4.11 (c) shows the results of RH 30%. At the extremely low humidification, the performance characteristics of 2-3 are similar to S8L2 at the low- and medium-load current region. At the high-load current region, however, the characteristics of 2-3 are similar to those of S2L8. This result indicates that the water retention capability of 2-3 under extremely low humidification is insufficient as the electro-osmotic drag increases at the high current region.

Figure 4.12 shows the standard deviation of cell voltage. As expected with simulation results of liquid water saturation through the GDL (Figure 4.3), the voltage instability of 2-3 reveals the medium characteristics of S8L2 and S2L8, especially with RH 100%, where the effect of mass transport loss is remarkable: the water management capability of 2-3 throughout the whole cell has averaged characteristics between the two base GDL's as well as locally improved water management capabilities.

The transient response characteristics of 2-3 are also analyzed. Figure 4.13 shows the transient response of the cell voltage of 2-3 with the results of S8L2 and S2L8. As mentioned above, the characteristics of transient response of 2-3 followed the strong point of S8L2 and S2L8 at the RH 50% and RH 100%, respectively. At the extremely low humidification of RH 30%, 2-3 had the medium characteristics between S8L2 and S2L8.

The effect of in-plane GDL structure design on the water management and cell performance are determined, and analyzed by prediction from the simulation work and verification from the experimental work. Through consideration of dry and wet areas of the cell, the structural design parameters of water retention and removal

capability can be applied locally, and in-plane structure design of the GDL uniquely enhances water management. This improves the variation of the mass transport throughout the cell, and results in uniformed current density distribution in the cell. The enhanced cell performance and local thermal characteristics with uniformed current density distribution are expected for the long term operation of the fuel cell.

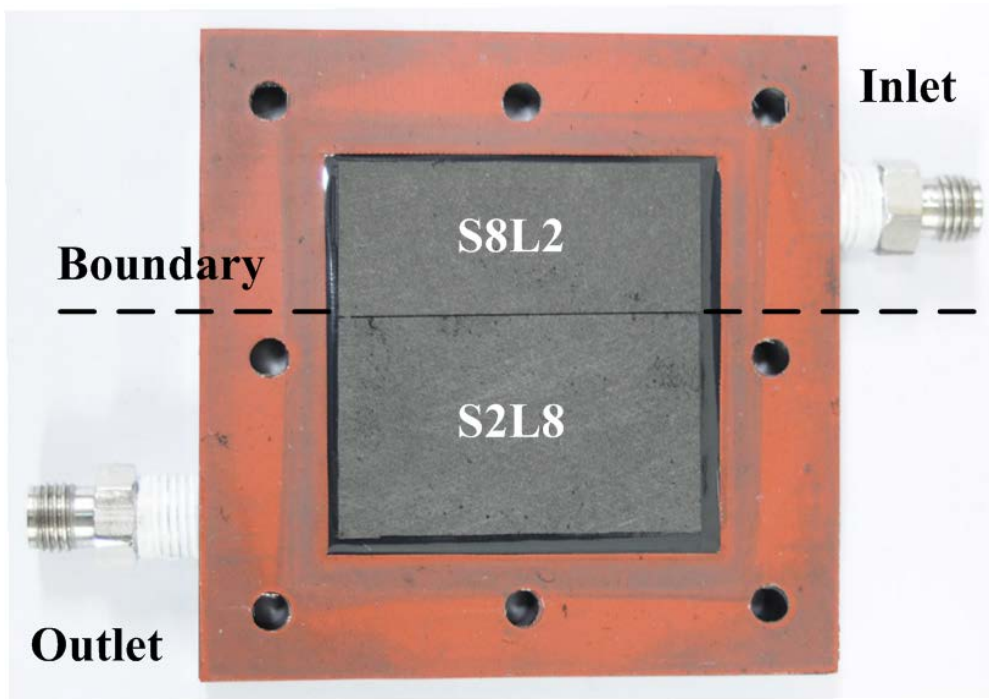


Figure 4.9 Experimental setup of combination of 2-3

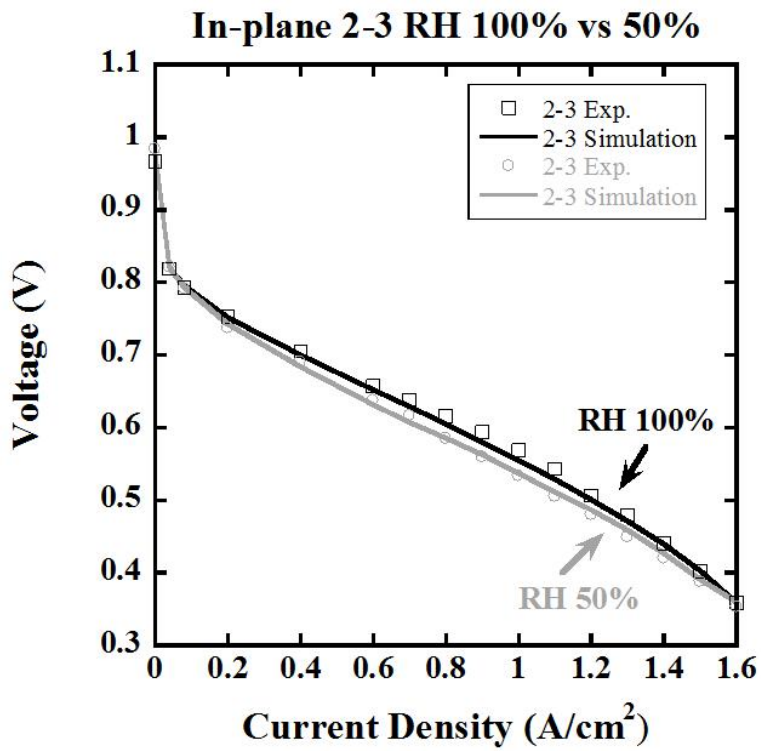


Figure 4.10 Steady-state performance of 2-3 and validation of simulation results

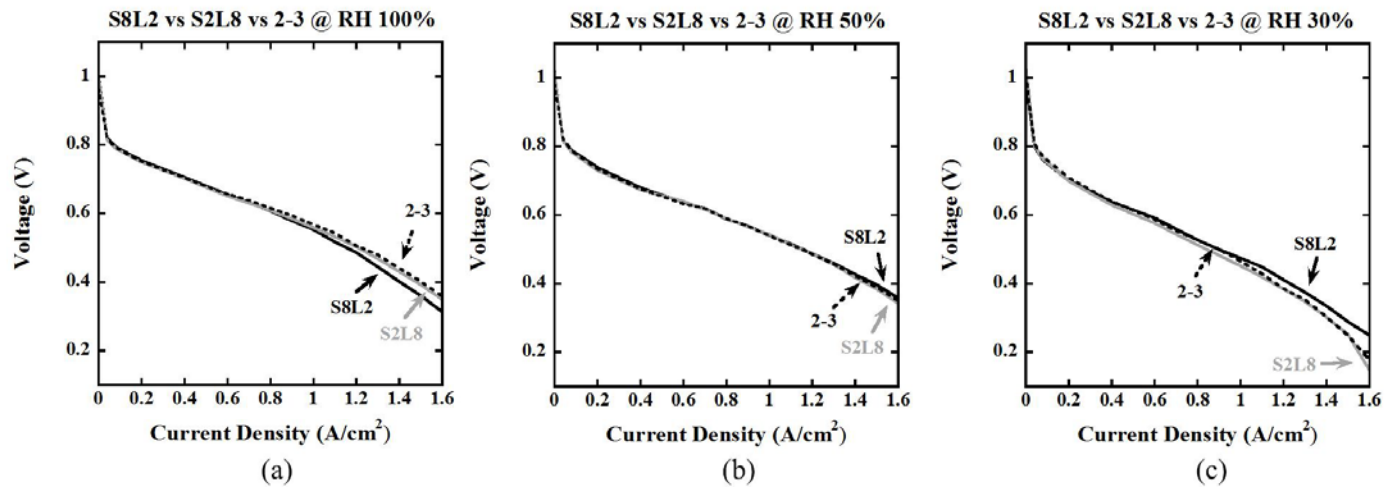


Figure 4.11 Comparison of steady-state performance of S8L2, S2L8, and 2-3: (a) at RH 100%, (b) at RH 50%, and (c) at RH 30%

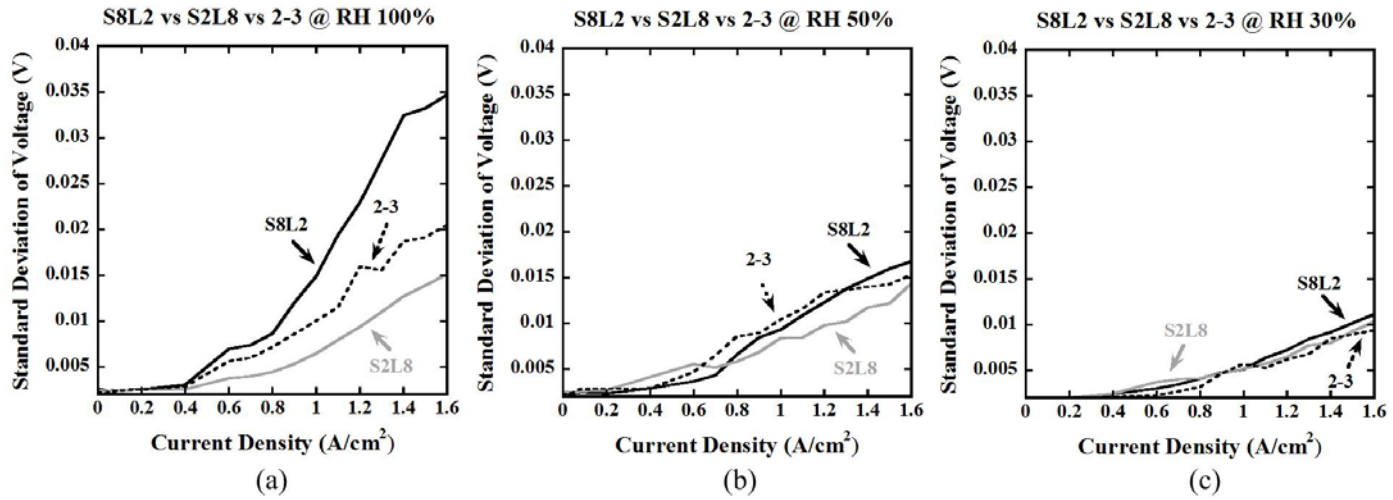


Figure 4.12 Comparison of standard deviation of voltage of S8L2, S2L8, and 2-3: (a) at RH 100%, (b) at RH 50%, and (c) at RH 30%

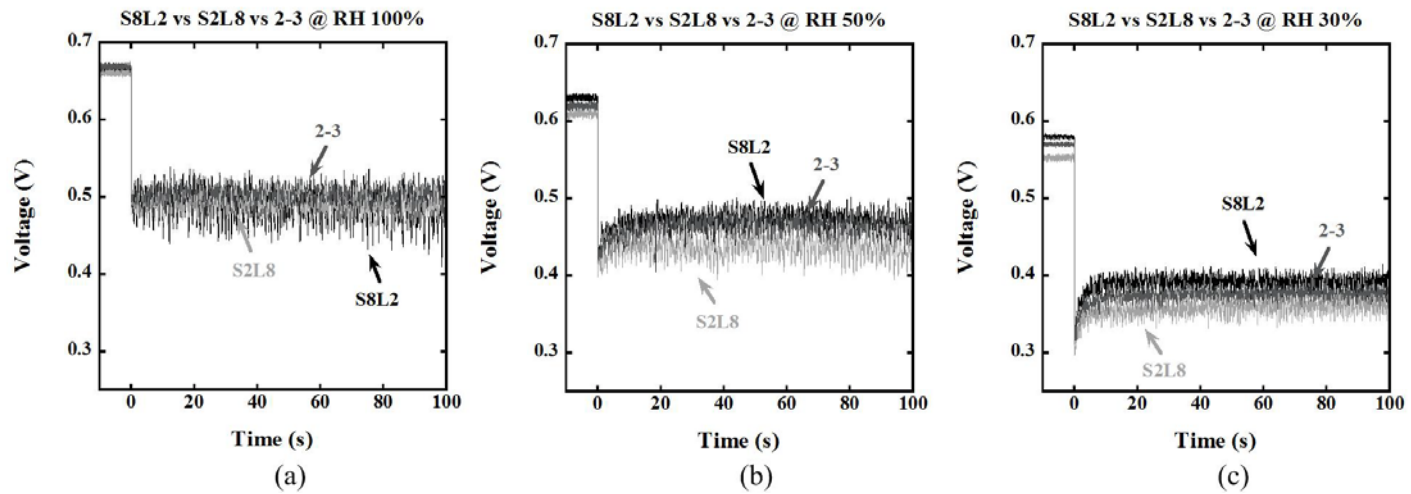


Figure 4.13 Comparison of transient response of S8L2, S2L8, and 2-3: (a) at RH 100%, (b) at RH 50%, and (c) at RH 30%

Chapter 5. Effect of through-plane structure design of the GDL on water management and cell performance

As discussed in Chapter 3, the pore size variation of the substrate affects the MPL and MPL penetration characteristics, but not significantly, the substrate itself. Especially, as shown in Figure 3.18, the averaged capillary pressure gradient values through the substrate were almost same between two GDL samples which have differing pore sizes in the substrate. Starting from the catalyst layer, the liquid water is transported to the next part such as MPL, MPL penetration, and substrate with a large capillary pressure gradient due to the significant variation of pore size or porosity between the GDL parts. However, once the liquid water is transferred from the MPL penetration region to the substrate, the liquid water is transported to the channel with an averaged capillary pressure gradient of the single substrate with same pore size and porosity even though the substrate has the largest thickness and mass transport resistance among the GDL parts. To enhance the liquid water transport in the substrate, the capillary pressure gradient should be increased continuously inside the substrate, in the direction from the catalyst layer to the channel.

In this chapter, a GDL with pore size gradient structure in the substrate is designed and analyzed incorporation of a continuously increasing capillary pressure gradient in the substrate. The GDL which has the continuously increased pore size throughout the substrate is designed artificially. The effect of the GDL on water management and cell performance is investigated using the simulation work. Especially, the liquid water saturation values of the substrate between pore size gradient GDL and normal GDL are compared. After the confirmation of the effect, the

pore size gradient GDL is fabricated and the effects is verified by the experimental work of steady-state cell performance, transient response of voltage, porosimetry, and SEM image analysis. Specially, analyses of porosimetry and SEM image are used to verify the pore size gradient structure of the substrate.

The potentials of through-plane structure design of the GDL are investigated to determine ideal GDL structure which has enhanced water management capability.

5.1 Design of the GDL

To design the pore size gradient GDL, the reference GDL is necessary. The reference GDL is selected by the conventional GDL which has the weight portion of long carbon fiber (13 mm) and short carbon fiber (6 mm) as 50% and 50%, respectively. To refer to each GDL in a simple way, the notations of “PG” and “NPG” which means “Pore size gradient” and “Non-pore size gradient” will be used in this study. The characteristics of NPG are analyzed in the same way as the S8L2 and S2L8 GDL in Chapter 3. With porosimetry analysis, the pore diameter and local porosity are determined. Additionally, the water permeability test is conducted to evaluate the internal contact angle. The identified characteristics of NPG are listed in Table 5.1.

With the basic characteristics of NPG, PG is designated. Since the model has four control volumes of the substrate part, the pore size of the substrate is set to have a gradient from 50 μm to 95 μm increasing by 30% for each control volumes as shown in Figure 5.1. In addition to the increase of pore size, the porosity of the substrate is set to have a gradient and the values are 86%, 87%, 89%, and 90% from the near catalyst layer to channel. The averaged porosity of the substrate of PG is 88% and it is the same as the porosity of the substrate of NPG. In Chapter 3, it is found that the porosity of MPL penetration and MPL is affected by the pore size variation of the substrate. Because the pore size of PG starts from 50 μm , MPL penetration and MPL porosity is set to 64% and 37%, respectively. They are the same as the value of S2L8 in Chapter 3. The thickness and contact angle of each control volumes of the GDL are the same as the value of NPG. The designed structural characteristics of PG are also listed in Table 5.1.

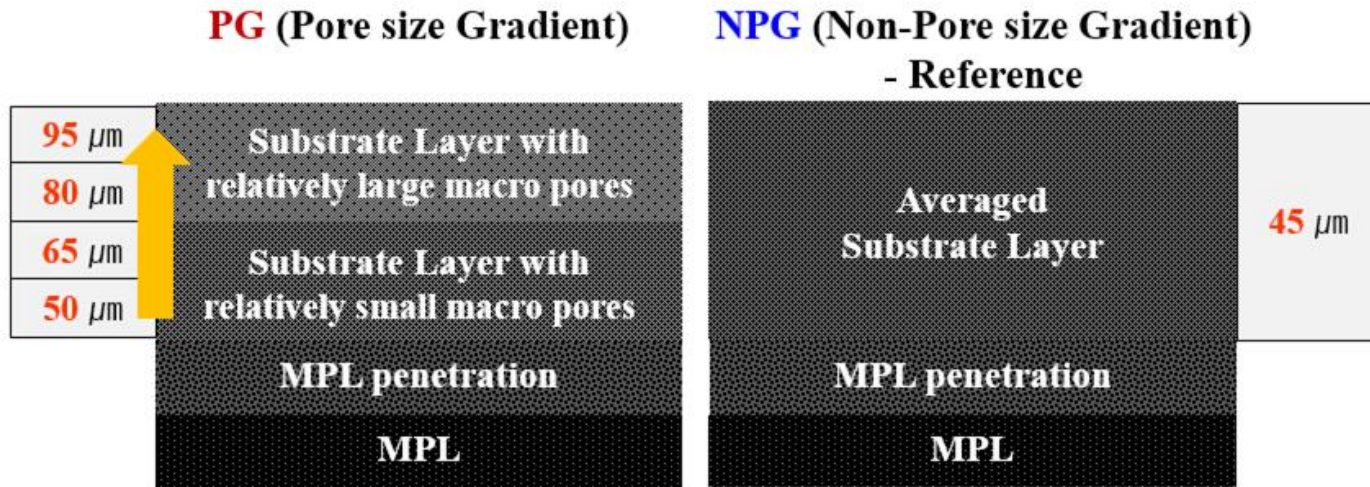


Figure 5.1 Design concept of the PG

Table 5.1 Structural parameters of the GDL: PG and NPG

Description		PG (assumption)	NPG (measured)
Thickness	MPL	58 μm	58 μm
	MPL penetration	59 μm	59 μm
	Substrate only (No MPL penetration)	197 μm	197 μm
Porosity	MPL	37%	31%
	MPL penetration	64%	64%
	Substrate 4	86%	88%
	Substrate 3	87%	
	Substrate 2	89%	
	Substrate 1	90%	
Pore diameter	MPL	0.0055 μm	0.0055 μm
	MPL penetration	0.1 μm	0.1 μm
	Substrate 4	50 μm	44.8 μm
	Substrate 3	65 μm	
	Substrate 2	80 μm	
	Substrate 1	95 μm	
Contact angle	MPL	140.5°	140.5°
	MPL penetration	130°	130°
	Substrate	122.5°	122.5°

5.2 Analysis with simulation results

Figure 5.2 shows the steady-state cell performance of PG and NPG. The result included the validation of simulation results of NPG with the experimental data. The simulation results of NPG showed a good agreement with the experimental data of RH 100% and 50% conditions. The averaged errors of the simulation results of NPG at RH 100% and 50% are 0.7% and 0.8%, respectively.

The performance of PG is higher than that of NPG at the high-load current region under both RH 100% and 50% conditions as shown in Figure 5.2. The cell voltage of PG at 1.6 A/cm^2 from the simulation work is 6.5% higher than that of NPG from experimental work. In case of RH 50%, the cell voltage of PG is 4.4% higher than that of NPG. The reason of improved performance is that the activation overvoltage is improved at both humidifications as shown in Figure 5.3.

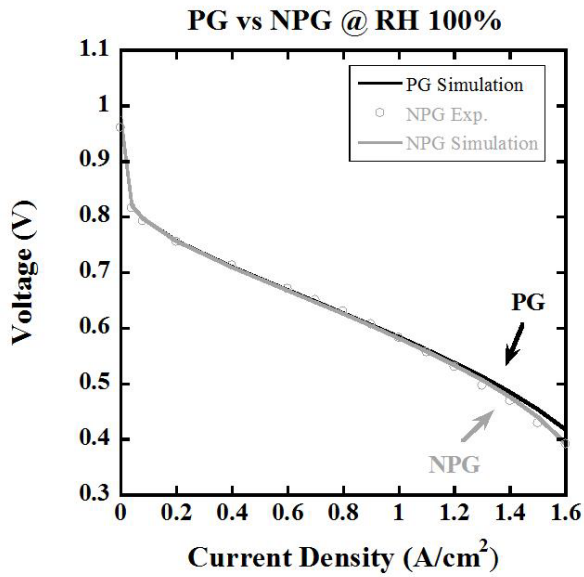
To elucidate reason of the improved activation overvoltage, the liquid water saturation of PG and NPG also analyzed. As shown in Figure 5.4, the liquid water saturation of PG is 23.1% lower than that of NPG at the substrate. Contrary to the results of S8L2 and S2L8 in Chapter 3, the capillary pressure gradient increased continuously through the substrate with the pore size gradient structure. Therefore, the liquid water saturation is decreased compared to normal GDL of NPG. Since the pore size of PG starts at $50 \mu\text{m}$ while that of NPG starts at $44.8 \mu\text{m}$, the MPL porosity of PG is higher than that of NPG. Thus, the liquid water saturation of PG at the MPL is lower than that of NPG.

The results of Figure 5.5 confirmed the increased capillary pressure gradient in the substrate. From substrate 4 to 1 in control volumes, the averaged capillary pressure

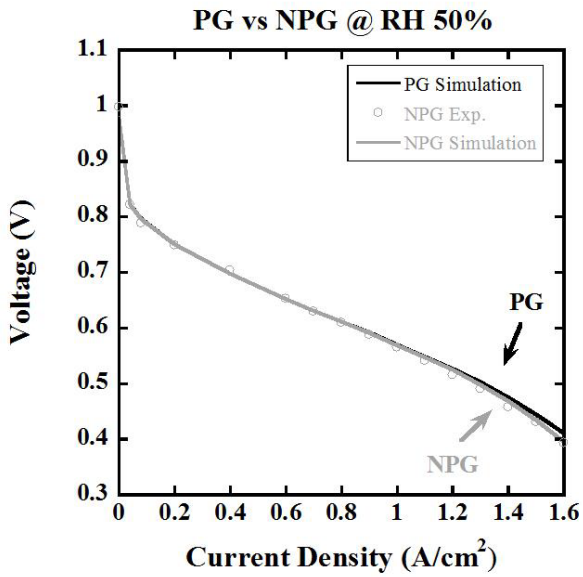
gradient of PG at RH 100% is 68.6% higher than that of NPG. Through improved liquid water removal capability, the mass transport through the GDL is enhanced.

As shown in Figure 5.6, the oxygen concentration of PG is higher than that of NPG in the entire GDL. Thus, smooth supply of oxygen from the channel to the catalyst layer is possible. Notably, the effect is significant at the high-load conditions which have high liquid water saturation and the large amount of reactant gases as shown in Figure 5.7.

From the results, the improved cell performance of PG is due to the enhanced mass transport in both MPL and substrate. To determine the contribution of each improvement, only the pore size gradient effect is simulated and analyzed: the same PG, except for the MPL porosity, with had the same value of NPG. The cell voltage is 0.3960 V at 1.6 A/cm² and RH 100%, while, that of NPG is 0.3923 V and PG is 0.4175 V. Under these conditions, the cell voltage of is improved by 6.4% compared to that of NPG, and the contribution of pore size gradient effect is 15.6% of total improvement. When the pore size gradient structure is applied, both increases in MPL porosity and capillary pressure gradient in the substrate, enhance the cell performance as a consequence.



(a)



(b)

Figure 5.2 Steady-state performance and validation of NPG, and simulation results of PG: (a) at RH 100% and (b) RH 50%

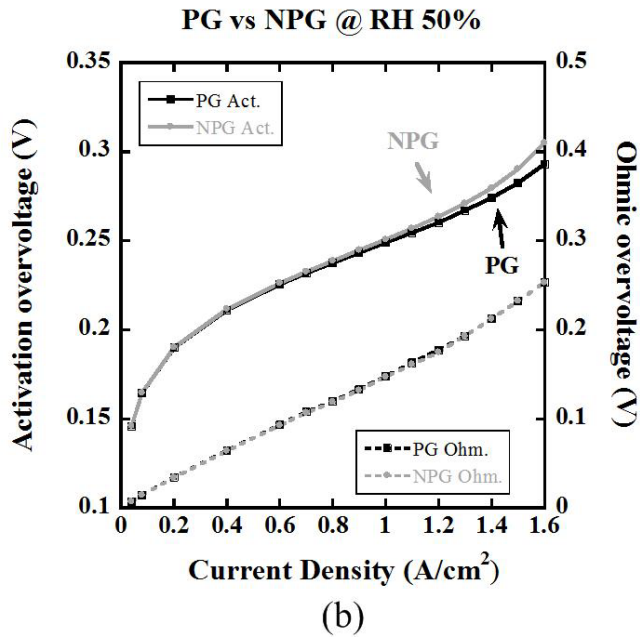
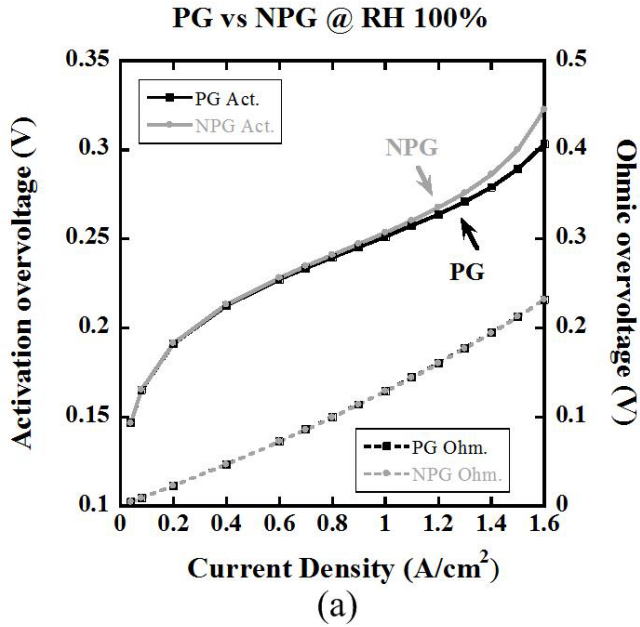
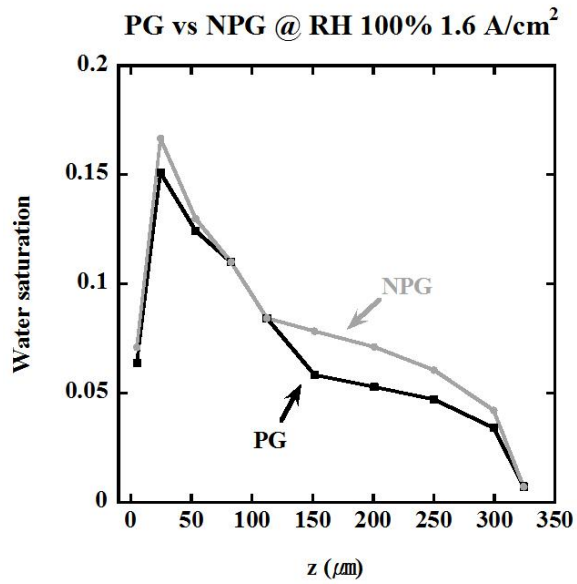
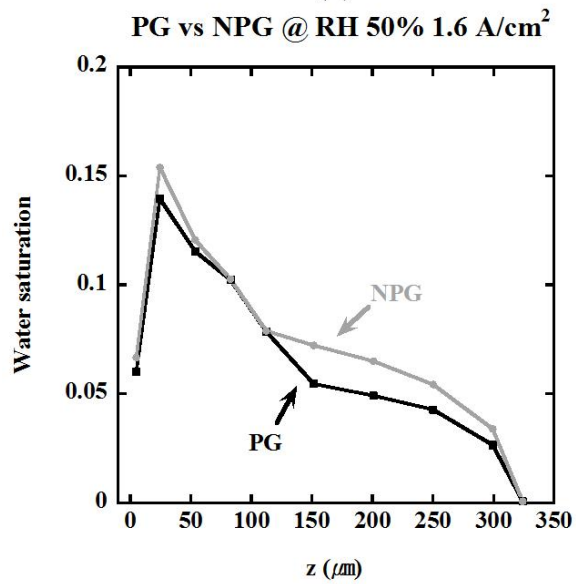


Figure 5.3 Overvoltages of PG and NPG: (a) at RH 100% and (b) at RH 50%



(a)



(b)

Figure 5.4 Liquid water saturation along the GDL thickness of PG and NPG at 1.6 A/cm²: (a) at RH 100% and (b) at RH 50%

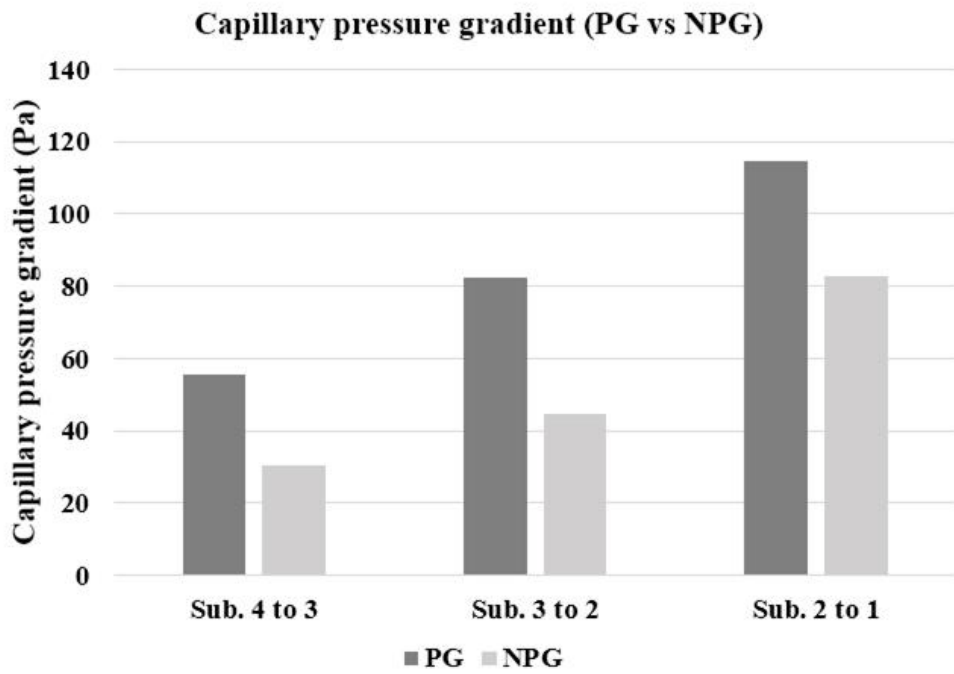


Figure 5.5 Capillary pressure gradient of PG and NPG along the substrate at RH 100%

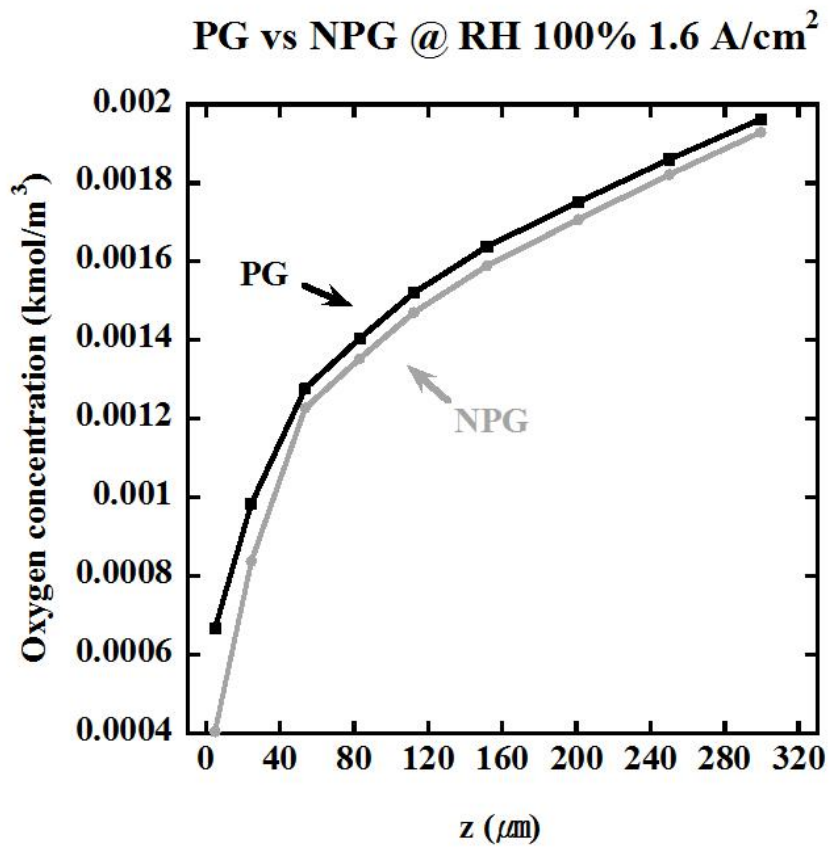


Figure 5.6 Oxygen concentration of PG and NPG along the GDL thickness

PG vs NPG @ RH 100%

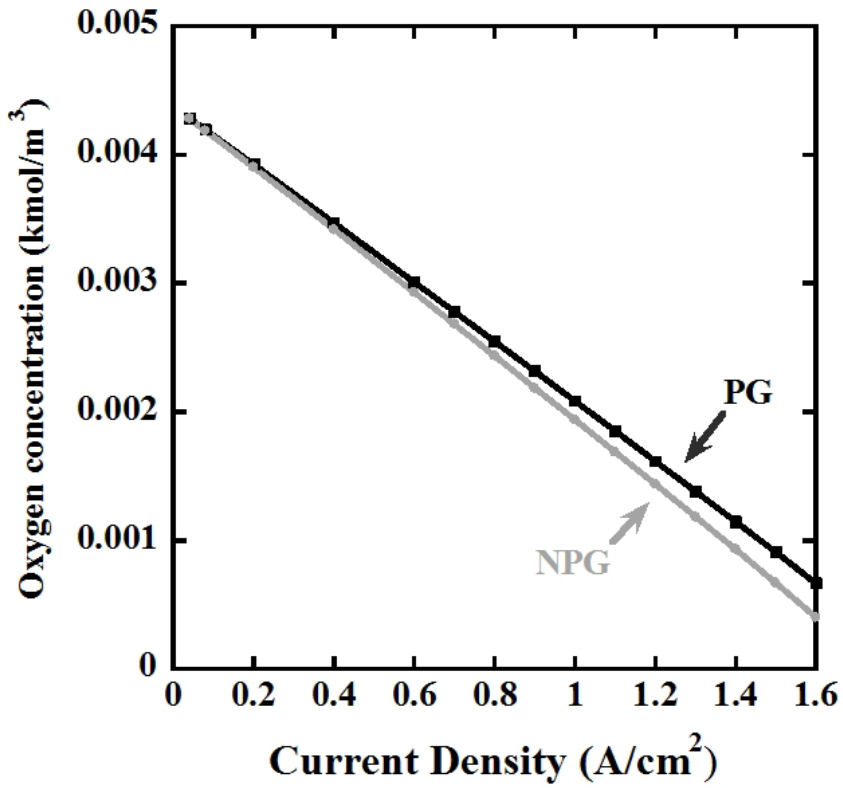


Figure 5.7 Oxygen concentration of PG and NPG according to current density

5.3 Verification of the effect of through-plane structure design with experimental results

Through simulation work, it is found that the through-plane structure design of the GDL has an effect of improved water removal capability and enhanced mass transport through the GDL. As derived, the GDL which has pore size gradient structure in the substrate is fabricated. The basic concept of producing pore size gradient structure is controlling the portion of long (13 mm) and short (6 mm) carbon fibers locally inside the substrate. As described in Chapter 3, the long carbon fibers make relatively large macro-pores and short carbon fibers make the relatively small macro-pores. Therefore, the substrate is designed to have a high portion of short carbon fibers adjacent the MPL, and to have a high portion of long carbon fibers adjacent the channel. Again, as derived, small and large macro-pores coexist in the substrate, with an increasing pore size gradient from the adjacent MPL to the adjacent channel. The fabricated GDL is evaluated by analysis of SEM image, porosimetry, steady-state cell performance, and transient response of voltage.

5.3.1 Analysis with scanning electron microscope

Figure 5.8 shows the surface SEM images of the substrate of PG and NPG. The NPG had the same size of macro-pores on both sides of the substrate. However, the PG has different sizes of macro-pores on each side. As shown in the figure, the one side, in which MPL penetrates to the substrate, had the relatively small macro-pores, while, the other side, which met the channel, had relatively large macro-pores. This variation is also confirmed with the cross-sectional SEM images as shown in Figure 5.9. The NPG has almost the same size of pores throughout the substrate, while, the

pore size increased along the direction from catalyst layer to channel in case of PG. Liquid water transported to channel with increased capillary pressure gradient in this structure.

5.3.2 Analysis with porosimetry

Figure 5.10 shows the pore size distribution of the PG and NPG. As the same MPL slurry is applied to the substrate, and the penetration ratio is the same, the pore size distribution under the pore size of 5 μm is the same in both samples. Over the pore size of 5 μm , there are different pore size distributions between the two samples. The outstanding finding is that the pore size distribution of the PG is moved to the right compared to that of NPG, which is characterized by an increase of pore size in the substrate. The peak pore size is 44.8 μm for the NPG and 54.6 μm for the PG. Additionally, the distribution of the PG had a large breadth between the start and end of the pore sizes. From the start of the distribution at a pore size of 5 μm of both samples, the distribution reaches 74.0 μm for the NPG and 99.3 μm for the PG. For comparison, the results of pore size distribution of the S8L2 and S2L8 in Chapter 3 are also analyzed. From the results, the peak pore size of S8L2 is 36.7 μm , and is moved to the right and corresponds to the peak pore size of S2L8 which is 49.5 μm . However, the distribution reaches 66.8 μm for the S8L2 and 81.6 μm for the S2L8. It means that the whole pore size of the S8L2 is simply increased without variation of the breadth of pore size distribution. Consequently, not only the whole pore size of the substrate is increased but also the variable breadth in pore size is increased when the pore size gradient structure is used in the substrate.

In the PG sample, as evidenced by SEM image and porosimetry analysis the pore size gradient, which increases continuously from adjacent the MPL to adjacent the channel, is consistent with the increase of the capillary pressure gradient.

5.3.3 Steady-state performance

Figure 5.11 shows the steady-state performance of the PG and the NPG at RH 100% and 50%. As predicted by the simulation work, cell performance of PG is enhanced especially at the high-load current region compared to that of NPG at both RH 100% and 50%. The cell voltages of the PG at the load current density of 1.6 A/cm² under RH 100% and 50% are, respectively, 10.8% and 9.8% higher than in the NPG. These results are illustrated by the simulation results for lowered liquid water saturation at the substrate with the increase of capillary pressure gradient inside the substrate resulting in improved mass transport loss of PG.

The results for voltage instability also confirm that the improved cell performance of the PG is due to enhanced mass transport. Figure 5.12 illustrates how the voltage instability in the PG is lower than that of the NPG at the high-load current region under both fully and low humidification. These results also support the enhanced water management from the pore size gradient in the PG structure.

5.3.4 Transient voltage response

Figure 5.13 shows the transient voltage response of the PG and NPG when the step change in current is applied. After the step change in current is applied, both RH 100% and 50% results show that the PG sample had a smaller fluctuation compared to the NPG. The large amount of produced water is efficiently expelled toward the

channel with the PG while the produced water is stagnated with the NPG. Therefore, oxygen diffuses smoothly to the catalyst layer with the PG and the fluctuation of voltage decreases after a sudden increase of the load current.

In this chapter, through predictions from simulation work and verifications from the experimental work, it is determined that the through-plane structure design of the GDL, incorporating the pore size gradient structure in the substrate, facilitates liquid water transport by the sustained increase of capillary pressure gradient in the substrate. Due to this effect, the liquid water is effectively expelled toward the channel, and the mass transport toward the catalyst layer is improved. As a result, the cell performance is increased at both RH 100% and 50%.

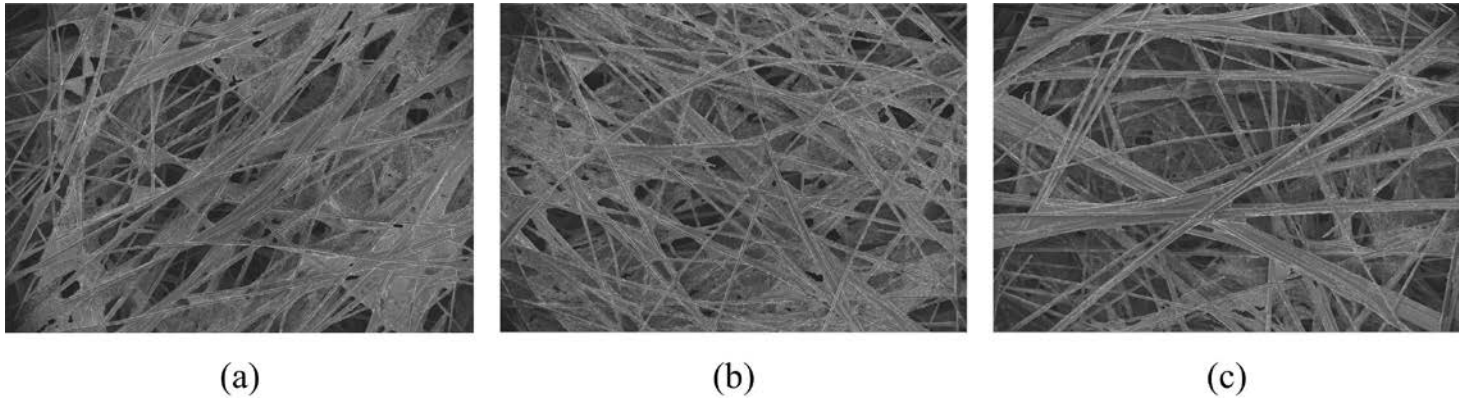


Figure 5.8 Surface images of PG and NPG: (a) NPG, (b) small macro-pores of PG near the MPL, and (c) large macro-pores of PG near the channel

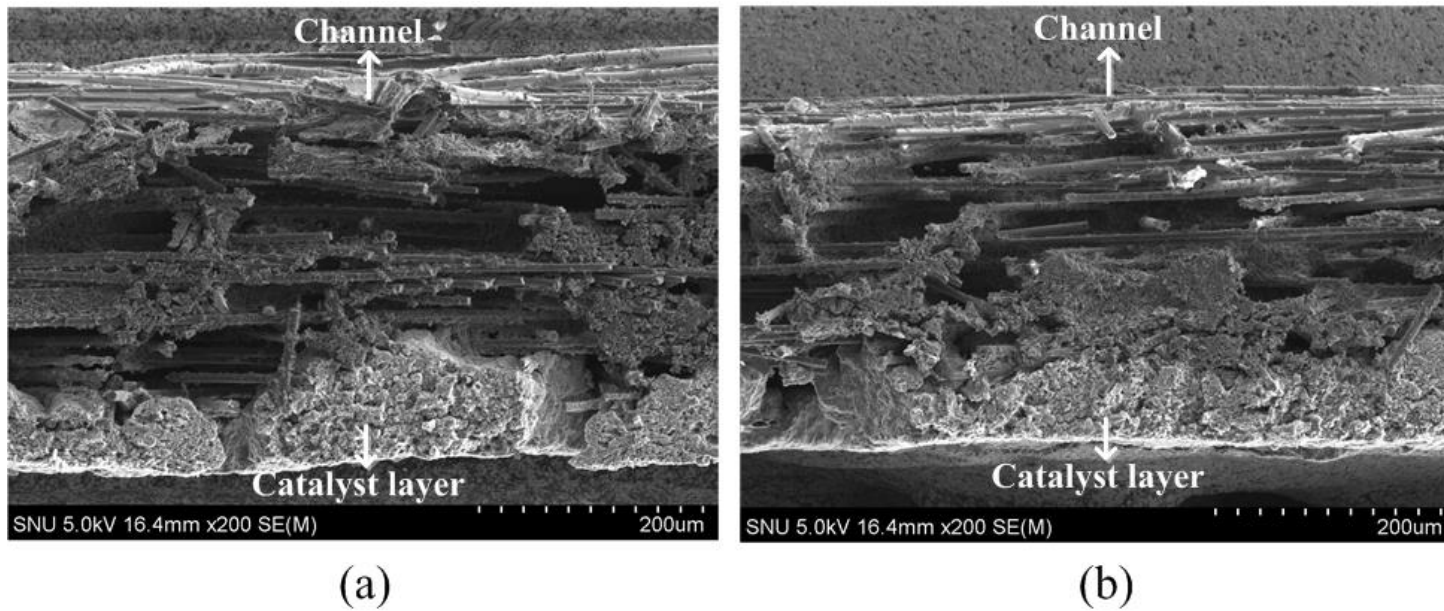


Figure 5.9 Surface image of PG and NPG: (a) PG and (b) NPG

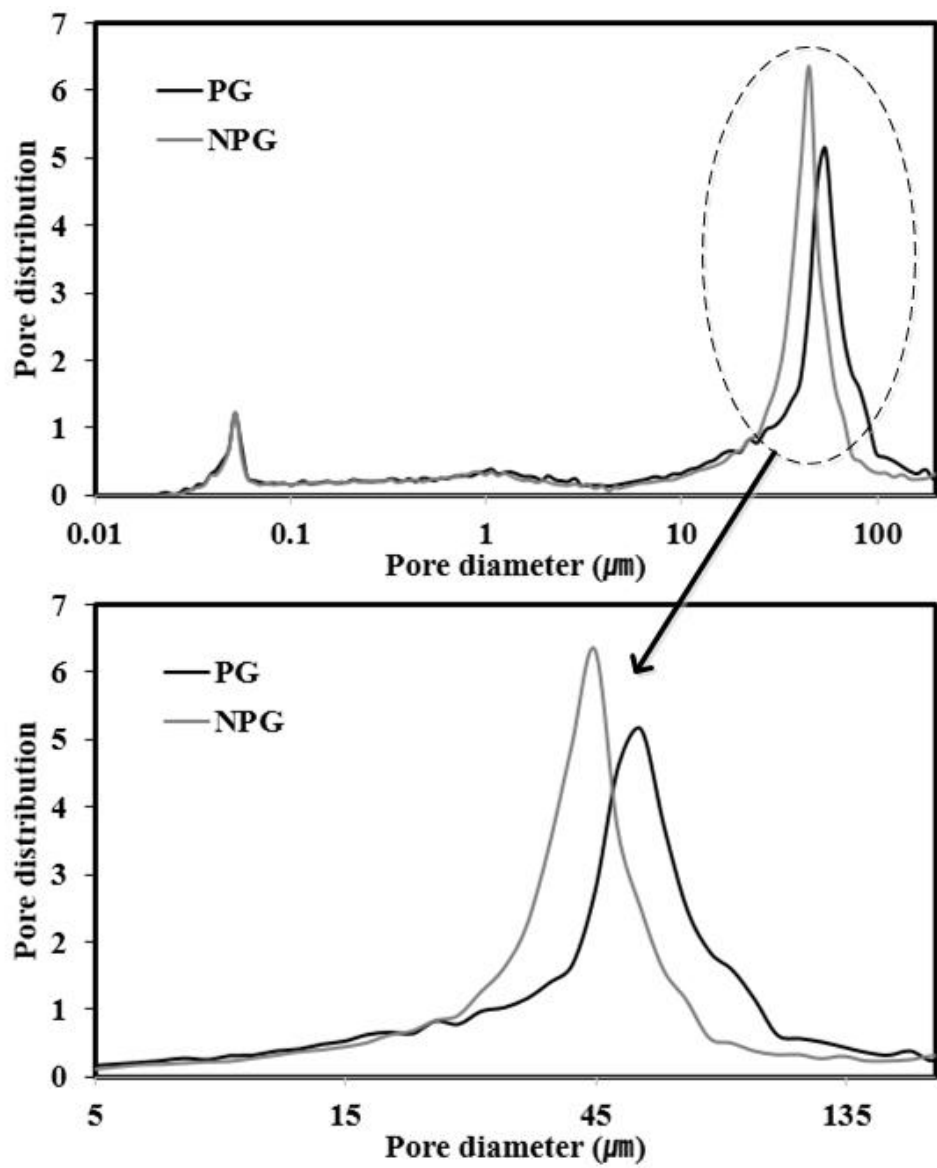
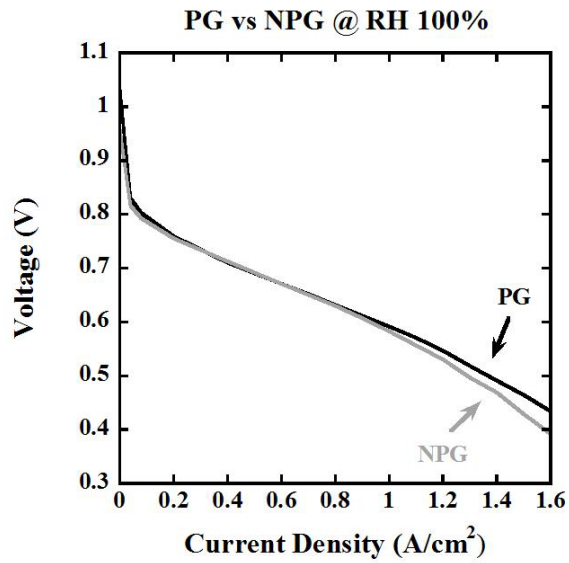
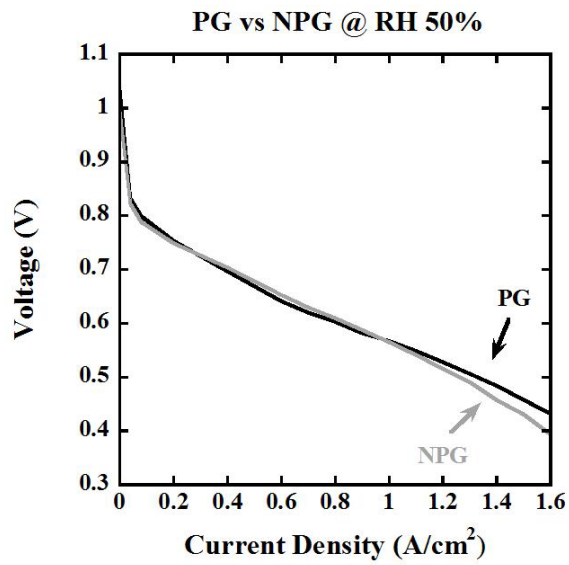


Figure 5.10 Pore size distribution of PG and NPG



(a)



(b)

Figure 5.11 Steady-state performance of the PG and NPG: (a) at RH 100% and (b) at 50%

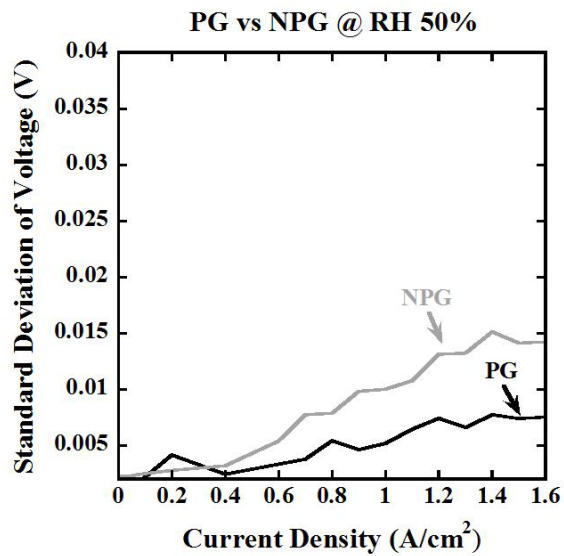
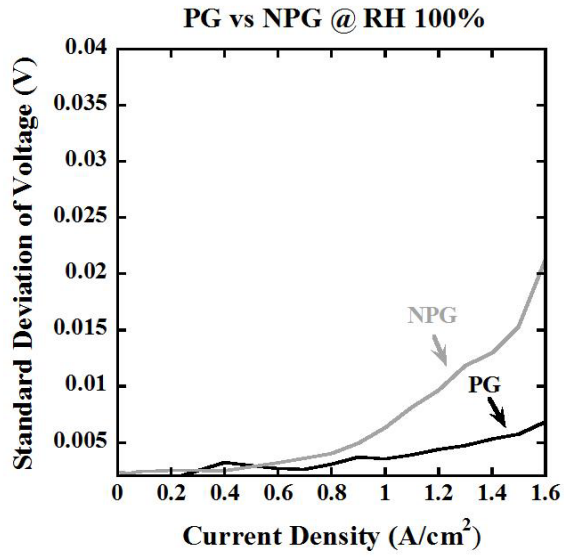
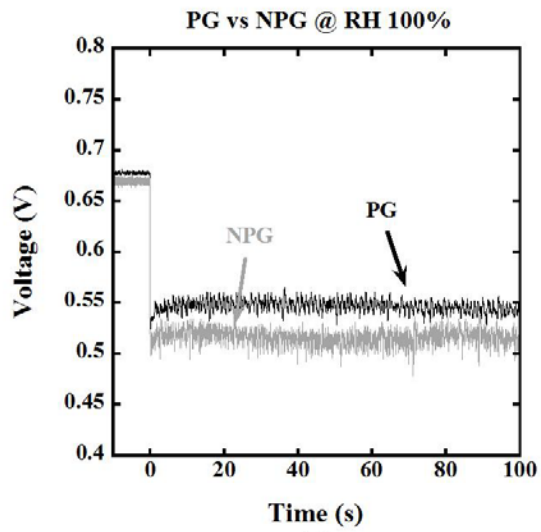
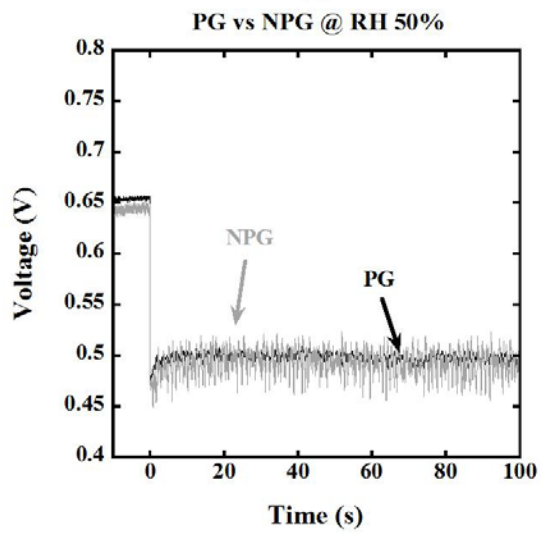


Figure 5.12 Standard deviation of voltage of PG and NPG: (a) at RH 100% and (b) at RH 50%



(a)



(b)

Figure 5.13 Transient response of PG and NPG: (a) at RH 100% and (b) at RH 50%

5.4 Suggestion of the ideal GDL structure design

The pore size gradient structure enhances the liquid water transport in the substrate with continually increased capillary pressure gradient as discussed above. Hence, the structure is suitable for application with the wet area of the cell such as channel outlet. In Chapter 4, discussing the effect of in-plane structure design, arrangement of the GDL which has water removal capability near the channel outlet shows the effective local water management capability. Therefore, enhanced water management capability is predictable when the pore size gradient structure is applied in the in-plane structure design for the wet area where induces mass transport loss.

In this section, the ideal GDL structure design with the integration of in-plane and through-plane structure is suggested. The concept of the ideal GDL structure is illustrated in Figure 5.14. The effect of the design is investigated with the simulation work. With the basic GDL structure which is 2-3 combination in Chapter 4, the pore size gradient structure is applied to the S2L8 which occupy 60% of the area from the channel outlet. The same pore size and porosity of the substrate in the pore size gradient structure in this chapter is applied to the S2L8.

Firstly, the cell voltage, activation overvoltage, and ohmic overvoltage are analyzed. Figure 5.15 shows the results of the cell voltage and overvoltage at RH 100% and 50% conditions. In this simulation work, the current density of 1.6 A/cm² case is investigated without consideration of the whole operating range of the polarization curve. The results show that improved activation overvoltage of the ideal GDL structure compared to the 2-3 combination. With the improvement, the cell voltage of the ideal GDL is 1.4% and 0.9% higher than that of 2-3 at RH 100% and 50%, respectively. This improvement is emphasized when compared to the single GDL of S8L2 and S2L8. The cell voltage of the ideal GDL at RH 100% is 16.3% and 2.1%

higher than S8L2 and S2L8, respectively. The results mean that liquid water and mass transport through the GDL is enhanced when the integration of in-plane and through-plane structure design is applied. It is confirmed by the results of liquid water saturation. The liquid water saturation of the ideal GDL at RH 100% is 15.2% lower than that of 2-3 combination as shown in Figure 5.16. As the decrease in water saturation at the substrate, the mass transport is enhanced resulting in the improvement of the cell performance. Furthermore, applying the pore size gradient structure to the in-plane structure affects the uniformity of the fuel cell characteristics. The standard deviation of the local current density is analyzed as shown in Figure 5.17. In the results, the ideal GDL shows the lowest standard deviation value compared to not only 2-3 combination but also single GDL of S8L2 and S2L8. As discussed in Chapter 4, the in-plane structure design had an effect of making the current density distribution uniformly. Added to this, when the pore size gradient structure is applied to the wet area of the cell, smooth mass transport is possible resulted in more uniform current density distribution compared to the 2-3 combination of Chapter 4.

Although manufacturing the ideal GDL structure is difficult for complexity, the effect of integration of in-plane and through-plane structure design on the water management and cell performance is investigated with the simulation work. As a result, the ideal GDL structure shows more powerful water management capability throughout the cell with increase in the cell performance as well as uniformity of fuel cell characteristics.

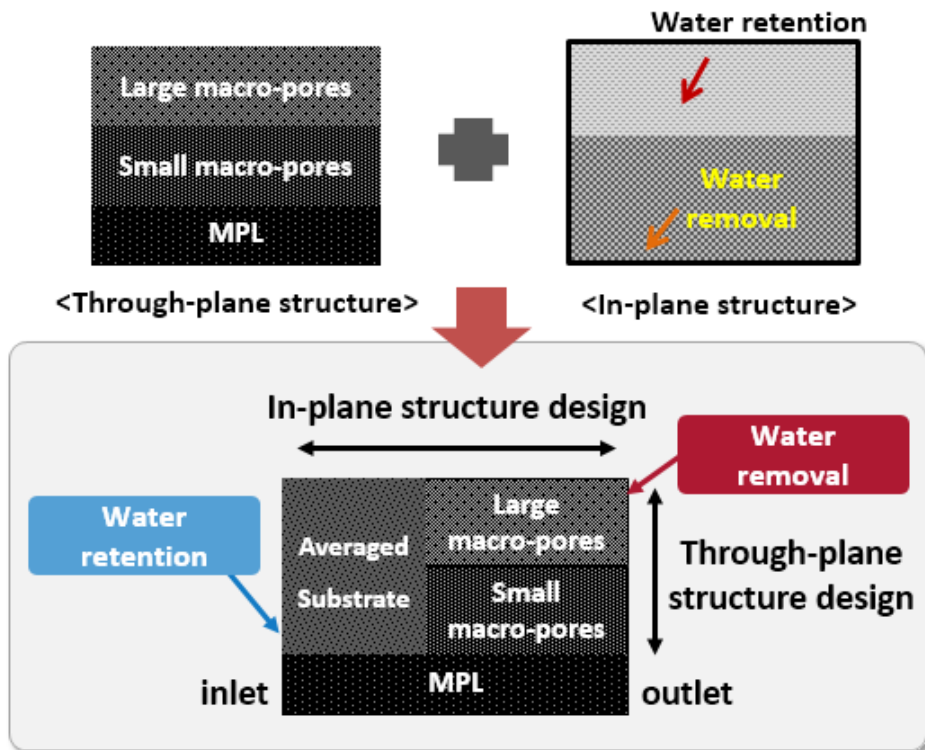
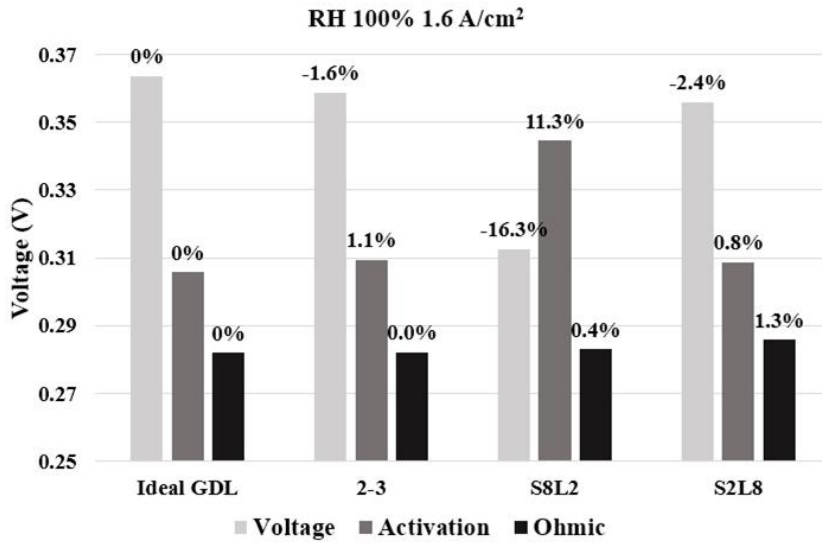
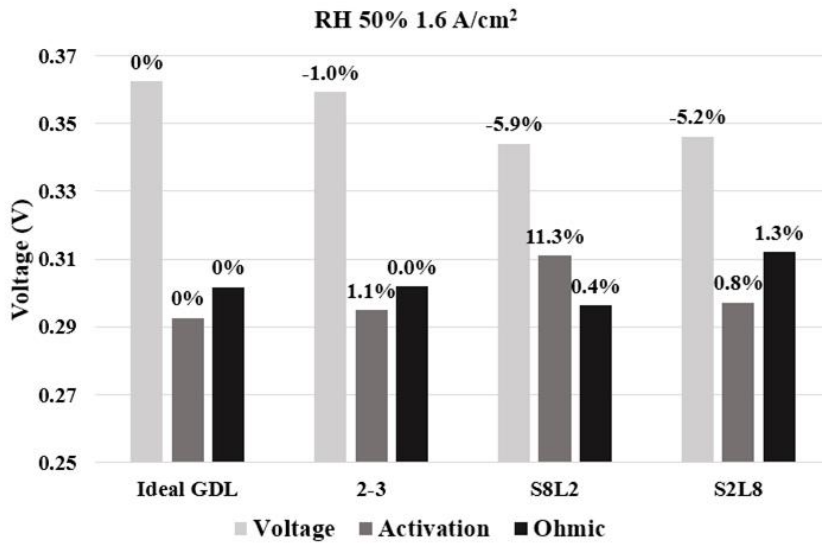


Figure 5.14 Illustration of the concept of the ideal GDL structure

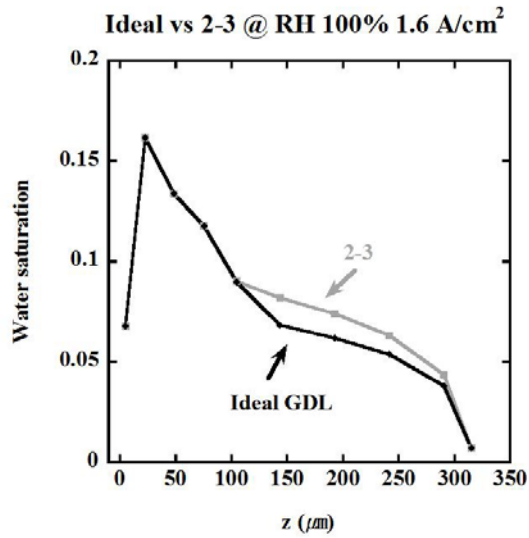


(a)

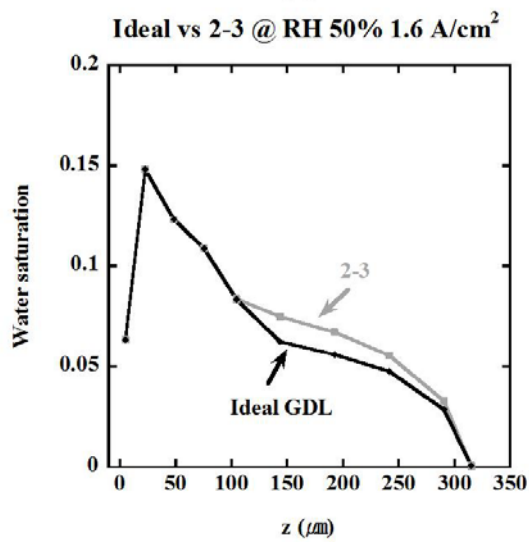


(b)

Figure 5.15 Voltage and overvoltages at 1.6 A/cm² according to GDL structure design: (a) at RH 100% and (b) at RH 50%



(a)



(b)

Figure 5.16 Liquid water saturation of the ideal GDL and 2-3 combination at 1.6 A/cm²: (a) at RH 100% and (b) at RH 50%

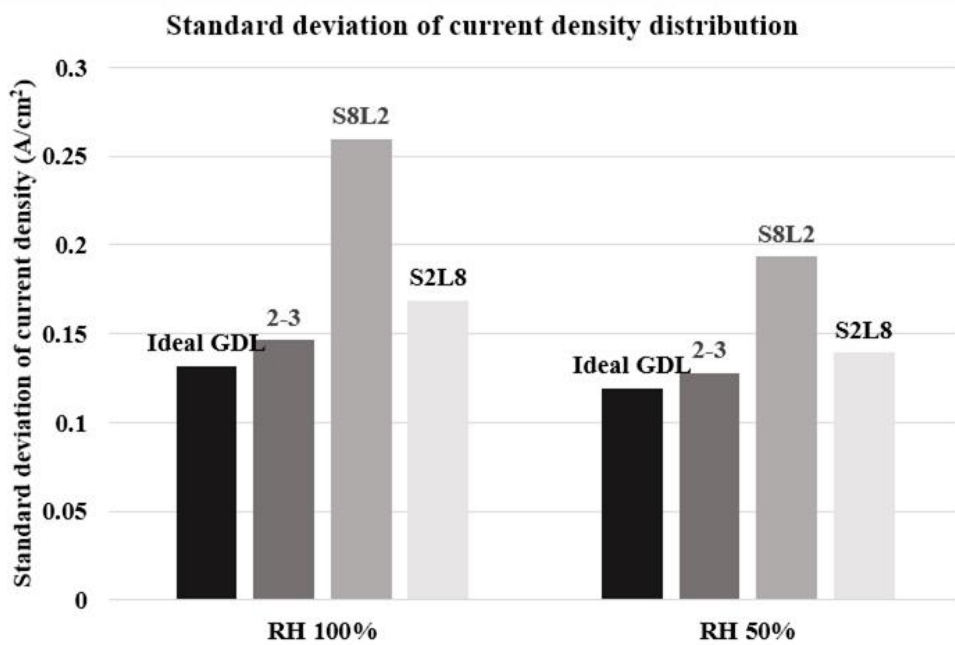


Figure 5.17 Standard deviation of current density distribution of combinations of GDL

Chapter 6. Conclusions

In this study, the structural characteristics of the GDL are investigated using both experimental and simulation work. By iteration between experimental and simulation work, the structural parameters of the GDL from the experimental work are used to refine the developed model. The model can predict the effects of the various structures of the GDL on water management and fuel cell performance.

The model in this study is developed in a quasi-three-dimensional geometry, making it possible to directly simulate the local characteristics of the fuel cell. To reflect the structural characteristics of the GDL, the control volumes are discretized into nine control volumes, which consist of the substrate, MPL penetration, the MPL, and the catalyst layer. In the GDL control volumes, macro-scale two-phase flow, Darcy's law, and the concepts of capillary pressure and relative permeability are considered. In this manner, the liquid water saturation in the GDL is predictive of the water management of the GDL and cell performance. Consequently, various structural design of the GDL can be evaluated, before fabrication, through the developed model and the effects on water management and cell performance can be investigated.

In the substrate, the long carbon fibers formed relatively large macro-pores while the short carbon fibers formed relatively small macro-pores. The variation of the portion of short and long carbon fiber lengths in the substrate affects not only its pore size but also the MPL and MPL penetration structural characteristics such as porosity. Specifically, when the MPL penetrates to the substrate, the MPL and MPL penetration are prone to be dense with relatively small macro-pores in the substrate. Conversely, the relatively large macro-pores of the substrate formed the MPL and MPL penetration more coarsely. Due to the differences between variations in the pore size in the

substrate, the relatively small macro-pores have water retention capability and the relatively large macro-pores have water removal capability.

The uniformity of the cell characteristics is improved with the in-plane structure design of the GDL. Near the channel inlet, the membrane is prone to be dry because the electro-osmotic drag flux is higher than the back diffusion flux. In contrast, the membrane is relatively wetter near the channel outlet due to the accumulation of water along the channel. The in-plane structure design is utilized to improve the uniformity of water management in the cell. Proper water balance in the cell is maintained by the incorporation of the GDL of water retention capability near the channel inlet and water removal capability near the channel outlet. Using the local water management capability, the two-phase mass transport is enhanced and results in improved cell performance with uniformed current density distribution.

To enhance the liquid water removal capability in the GDL, through-plane structure design of the GDL is introduced. Once the liquid water is transferred from the MPL penetration, it is transported to the channel driven by the averaged capillary pressure gradient of the substrate. The effective way to remove the liquid water in the substrate is to use pore size gradient structure that has continuously increased pore diameter from MPL penetration to channel. On the pore size gradient structure, the averaged capillary pressure gradient in the substrate is increased to 68.6% and the liquid water saturation in the substrate is 23.1% lower than that of the normal substrate structure in the simulation results. The liquid water transport is driven by the large capillary pressure gradient between the GDL parts, including; the MPL, MPL penetration, and the substrate. The pore size gradient structure enables smooth liquid water transportation by continuously increased capillary pressure gradient in the substrate. Therefore, enhanced two-phase mass transport can be achieved with the through-plane structure design of the GDL.

This research includes both experimental and simulation studies on various structural characteristics of the GDL, and its effect on water management and fuel cell performance. The measured properties of the GDL are applied to the model, and the model predicts the effects of various GDL structures, which is then verified through the experimental work. Using the iteration between experimental and simulation studies, this study contributes to elucidation and evaluation of the effects of various GDL structures, suggesting the ideal GDL structure, and developing the optimal control strategies under operating conditions.

Bibliography

- [1] Srinivasan S, Mosdale R, Stevens P, Yang C. Fuel cells: reaching the era of clean and efficient power generation in the twenty-first century. *Annual Review of Energy and the Environment*. 1999;24:281-328.
- [2] O'Hayre RP, Cha S-W, Colella W, Prinz FB. *Fuel cell fundamentals*. 2006.
- [3] Larminie J, Dicks A, McDonald MS. *Fuel cell systems explained*: Wiley New York; 2003.
- [4] *Automotive World Car Industry Forecast Report*. Global Insight. 2004.
- [5] Thampan T, Malhotra S, Zhang J, Datta R. PEM fuel cell as a membrane reactor. *Catalysis Today*. 2001;67:15-32.
- [6] Kang S, Min K, Yu S. Dynamic modeling of a proton exchange membrane fuel cell system with a shell-and-tube gas-to-gas membrane humidifier. *International Journal of Hydrogen Energy*. 2012;37:5866-75.
- [7] Ihonen J, Mikkola M, Lindbergh G. Flooding of gas diffusion backing in PEFCs physical and electrochemical characterization. *Journal of the Electrochemical Society*. 2004;151:A1152-A61.
- [8] Ha T. *Study on degradation characteristics in gas diffusion layer of PEM fuel cell*. Seoul National University. 2010.
- [9] Chun JH, Park KT, Jo DH, Lee JY, Kim SG, Lee ES, et al. Determination of the pore size distribution of micro porous layer in PEMFC using pore forming agents under various drying conditions. *international journal of hydrogen energy*. 2010;35:11148-53.
- [10] Cindrella L, Kannan A, Lin J, Saminathan K, Ho Y, Lin C, et al. Gas diffusion layer for proton exchange membrane fuel cells—A review. *Journal of Power Sources*. 2009;194:146-60.
- [11] Su A, Weng F-B, Hsu C-Y, Chen Y-M. Studies on flooding in PEM fuel cell cathode channels. *International Journal of Hydrogen Energy*. 2006;31:1031-9.

- [12] Cho J. Study on transient response characteristics of a PEM fuel cell related with structure and degradation effects of a gas diffusion layer. Seoul National University. 2012.
- [13] Borup R, Davey J, Wood D, Garzon F, Inbody M, Guidry D. PEM fuel cell durability. DOE Hydrogen Program, FY. 2005.
- [14] Wu J, Yuan XZ, Martin JJ, Wang H, Zhang J, Shen J, et al. A review of PEM fuel cell durability: degradation mechanisms and mitigation strategies. *Journal of Power Sources*. 2008;184:104-19.
- [15] Borup RL, Davey JR, Garzon FH, Wood DL, Inbody MA. PEM fuel cell electrocatalyst durability measurements. *Journal of Power Sources*. 2006;163:76-81.
- [16] Lee C, Mérida W. Gas diffusion layer durability under steady-state and freezing conditions. *Journal of power sources*. 2007;164:141-53.
- [17] Lim S-J, Park G-G, Park J-S, Sohn Y-J, Yim S-D, Yang T-H, et al. Investigation of freeze/thaw durability in polymer electrolyte fuel cells. *International Journal of Hydrogen Energy*. 2010;35:13111-7.
- [18] Han K, Hong BK, Kim SH, Ahn BK, Lim TW. Influence of anisotropic bending stiffness of gas diffusion layers on the degradation behavior of polymer electrolyte membrane fuel cells under freezing conditions. *International Journal of Hydrogen Energy*. 2011;36:12452-64.
- [19] Lee Y, Kim B, Kim Y, Li X. Degradation of gas diffusion layers through repetitive freezing. *Applied Energy*. 2011;88:5111-9.
- [20] Lee Y, Kim B, Kim Y, Li X. Effects of a microporous layer on the performance degradation of proton exchange membrane fuel cells through repetitive freezing. *Journal of Power Sources*. 2011;196:1940-7.
- [21] Lee S-Y, Kim H-J, Cho E, Lee K-S, Lim T-H, Hwang IC, et al. Performance degradation and microstructure changes in freeze–thaw cycling for PEMFC MEAs with various initial microstructures. *International journal of hydrogen energy*. 2010;35:12888-96.

- [22] Luo M, Huang C, Liu W, Luo Z, Pan M. Degradation behaviors of polymer electrolyte membrane fuel cell under freeze/thaw cycles. *International Journal of Hydrogen Energy*. 2010;35:2986-93.
- [23] Ha T, Cho J, Park J, Min K, Kim H-S, Lee E, et al. Experimental study on carbon corrosion of the gas diffusion layer in polymer electrolyte membrane fuel cells. *International Journal of Hydrogen Energy*. 2011;36:12436-43.
- [24] Chen G, Zhang H, Ma H, Zhong H. Electrochemical durability of gas diffusion layer under simulated proton exchange membrane fuel cell conditions. *international journal of hydrogen energy*. 2009;34:8185-92.
- [25] Spornjak D, Fairweather J, Mukundan R, Rockward T, Borup RL. Influence of the microporous layer on carbon corrosion in the catalyst layer of a polymer electrolyte membrane fuel cell. *Journal of Power Sources*. 2012;214:386-98.
- [26] Owejan JE, Paul TY, Makharia R. Mitigation of carbon corrosion in microporous layers in PEM fuel cells. *ECS Transactions*. 2007;11:1049-57.
- [27] Fairweather JD, Li B, Mukundan R, Fenton J, Borup RL. In situ and ex situ characterization of carbon corrosion in PEMFCs. *ECS Transactions*. 2010;33:433-46.
- [28] Ha T, Cho J, Park J, Min K, Kim H-S, Lee E, et al. Experimental study of the effect of dissolution on the gas diffusion layer in polymer electrolyte membrane fuel cells. *International Journal of Hydrogen Energy*. 2011;36:12427-35.
- [29] Cho J, Ha T, Park J, Kim H-S, Min K, Lee E, et al. Analysis of transient response of a unit proton-exchange membrane fuel cell with a degraded gas diffusion layer. *International Journal of Hydrogen Energy*. 2011;36:6090-8.
- [30] Wood D, Xie J, Pacheco S, Davey J, Borup R. Durability issues of the PEMFC GDL and MEA under steady-state and drive-cycle operating conditions. Los Alamos National Laboratory; 2004.

- [31] Bevers D, Rogers R, Von Bradke M. Examination of the influence of PTFE coating on the properties of carbon paper in polymer electrolyte fuel cells. *Journal of power sources*. 1996;63:193-201.
- [32] Ioroi T, Oku T, Yasuda K, Kumagai N, Miyazaki Y. Influence of PTFE coating on gas diffusion backing for unitized regenerative polymer electrolyte fuel cells. *Journal of power sources*. 2003;124:385-9.
- [33] Lim C, Wang C. Effects of hydrophobic polymer content in GDL on power performance of a PEM fuel cell. *Electrochimica Acta*. 2004;49:4149-56.
- [34] Park G-G, Sohn Y-J, Yang T-H, Yoon Y-G, Lee W-Y, Kim C-S. Effect of PTFE contents in the gas diffusion media on the performance of PEMFC. *Journal of Power Sources*. 2004;131:182-7.
- [35] Park S, Popov BN. Effect of cathode GDL characteristics on mass transport in PEM fuel cells. *Fuel*. 2009;88:2068-73.
- [36] Park S, Popov BN. Effect of hydrophobicity and pore geometry in cathode GDL on PEM fuel cell performance. *Electrochimica Acta*. 2009;54:3473-9.
- [37] Lin G, Van Nguyen T. Effect of thickness and hydrophobic polymer content of the gas diffusion layer on electrode flooding level in a PEMFC. *Journal of The Electrochemical Society*. 2005;152:A1942-A8.
- [38] Wang Y, Wang C-Y, Chen K. Elucidating differences between carbon paper and carbon cloth in polymer electrolyte fuel cells. *Electrochimica Acta*. 2007;52:3965-75.
- [39] Liu C-H, Ko T-H, Chang E-C, Lyu H-D, Liao Y-K. Effect of carbon fiber paper made from carbon felt with different yard weights on the performance of low temperature proton exchange membrane fuel cells. *Journal of Power Sources*. 2008;180:276-82.
- [40] Park S, Popov BN. Effect of a GDL based on carbon paper or carbon cloth on PEM fuel cell performance. *Fuel*. 2011;90:436-40.
- [41] Tang H, Wang S, Pan M, Yuan R. Porosity-graded micro-porous layers for polymer electrolyte membrane fuel cells. *Journal of power sources*. 2007;166:41-6.

- [42] Weng F-B, Hsu C-Y, Su M-C. Experimental study of micro-porous layers for PEMFC with gradient hydrophobicity under various humidity conditions. *International Journal of Hydrogen Energy*. 2011;36:13708-14.
- [43] Chun JH, Park KT, Jo DH, Lee JY, Kim SG, Park SH, et al. Development of a novel hydrophobic/hydrophilic double micro porous layer for use in a cathode gas diffusion layer in PEMFC. *International Journal of Hydrogen Energy*. 2011;36:8422-8.
- [44] Cho J, Oh H, Park J, Min K, Lee E, Jyoung J-Y. Effect of the micro porous layer design on the dynamic performance of a proton exchange membrane fuel cell. *International Journal of Hydrogen Energy*. 2014;39:459-68.
- [45] Manahan M, Hatzell M, Kumbur E, Mench M. Laser perforated fuel cell diffusion media. Part I: Related changes in performance and water content. *Journal of Power Sources*. 2011;196:5573-82.
- [46] Cho J, Park J, Oh H, Min K, Lee E, Jyoung J-Y. Analysis of the transient response and durability characteristics of a proton exchange membrane fuel cell with different micro-porous layer penetration thicknesses. *Applied Energy*. 2013;111:300-9.
- [47] Zhang F-Y, Advani SG, Prasad AK. Performance of a metallic gas diffusion layer for PEM fuel cells. *Journal of power sources*. 2008;176:293-8.
- [48] Cho J, Oh H, Park J, Min K, Lee E, Jyoung J-Y. Study on the performance of a proton exchange membrane fuel cell related to the structure design of a gas diffusion layer substrate. *International Journal of Hydrogen Energy*. 2014;39:495-504.
- [49] Pekula N, Heller K, Chuang P, Turhan A, Mench M, Brenizer J, et al. Study of water distribution and transport in a polymer electrolyte fuel cell using neutron imaging. *Nuclear Instruments and Methods in Physics Research Section A: Accelerators, Spectrometers, Detectors and Associated Equipment*. 2005;542:134-41.
- [50] Kramer D, Zhang J, Shimoi R, Lehmann E, Wokaun A, Shinohara K, et al. In situ diagnostic of two-phase flow phenomena in polymer electrolyte fuel cells by neutron

- imaging: Part A. Experimental, data treatment, and quantification. *Electrochimica Acta*. 2005;50:2603-14.
- [51] Zhang J, Kramer D, Shimoi R, Ono Y, Lehmann E, Wokaun A, et al. In situ diagnostic of two-phase flow phenomena in polymer electrolyte fuel cells by neutron imaging: Part B. Material variations. *Electrochimica Acta*. 2006;51:2715-27.
- [52] Kowal J, Turhan A, Heller K, Brenizer J, Mench M. Liquid water storage, distribution, and removal from diffusion media in PEFCs. *Journal of the Electrochemical Society*. 2006;153:A1971-A8.
- [53] Trabold T, Owejan J, Jacobson D, Arif M, Huffman P. In situ investigation of water transport in an operating PEM fuel cell using neutron radiography: Part 1—Experimental method and serpentine flow field results. *International Journal of Heat and Mass Transfer*. 2006;49:4712-20.
- [54] Owejan JP, Trabold T, Jacobson D, Baker D, Hussey D, Arif M. In situ investigation of water transport in an operating PEM fuel cell using neutron radiography: Part 2—Transient water accumulation in an interdigitated cathode flow field. *International Journal of Heat and Mass Transfer*. 2006;49:4721-31.
- [55] Turhan A, Heller K, Brenizer J, Mench M. Quantification of liquid water accumulation and distribution in a polymer electrolyte fuel cell using neutron imaging. *Journal of Power Sources*. 2006;160:1195-203.
- [56] Turhan A, Heller K, Brenizer J, Mench M. Passive control of liquid water storage and distribution in a PEFC through flow-field design. *Journal of Power Sources*. 2008;180:773-83.
- [57] Hickner M, Siegel N, Chen K, Hussey D, Jacobson D, Arif M. In situ high-resolution neutron radiography of cross-sectional liquid water profiles in proton exchange membrane fuel cells. *Journal of The Electrochemical Society*. 2008;155:B427-B34.

- [58] Sinha PK, Halleck P, Wang C-Y. Quantification of liquid water saturation in a PEM fuel cell diffusion medium using X-ray microtomography. *Electrochemical and Solid-State Letters*. 2006;9:A344-A8.
- [59] Manke I, Hartnig C, Grünerbel M, Lehnert W, Kardjilov N, Haibel A, et al. Investigation of water evolution and transport in fuel cells with high resolution synchrotron X-ray radiography. *Applied Physics Letters*. 2007;90:174105.
- [60] Mukaide T, Mogi S, Yamamoto J, Morita A, Koji S, Takada K, et al. In situ observation of water distribution and behaviour in a polymer electrolyte fuel cell by synchrotron X-ray imaging. *Journal of synchrotron radiation*. 2008;15:329-34.
- [61] Tüber K, Pócza D, Hebling C. Visualization of water buildup in the cathode of a transparent PEM fuel cell. *Journal of Power Sources*. 2003;124:403-14.
- [62] Yang X, Zhang F, Lubawy A, Wang C. Visualization of liquid water transport in a PEFC. *Electrochemical and Solid-State Letters*. 2004;7:A408-A11.
- [63] Zhang F, Yang X, Wang C. Liquid water removal from a polymer electrolyte fuel cell. *Journal of the Electrochemical Society*. 2006;153:A225-A32.
- [64] Ge S, Wang C-Y. Liquid water formation and transport in the PEFC anode. *Journal of the Electrochemical Society*. 2007;154:B998-B1005.
- [65] Spornjak D, Prasad AK, Advani SG. Experimental investigation of liquid water formation and transport in a transparent single-serpentine PEM fuel cell. *Journal of Power Sources*. 2007;170:334-44.
- [66] Kimball E, Whitaker T, Kevrekidis YG, Benziger JB. Drops, slugs, and flooding in polymer electrolyte membrane fuel cells. *AIChE Journal*. 2008;54:1313-32.
- [67] Gao B, Steenhuis TS, Zevi Y, Parlange J, Carter RN, Trabold TA. Visualization of unstable water flow in a fuel cell gas diffusion layer. *Journal of Power Sources*. 2009;190:493-8.
- [68] Lee K-J, Nam JH, Kim C-J. Pore-network analysis of two-phase water transport in gas diffusion layers of polymer electrolyte membrane fuel cells. *Electrochimica Acta*. 2009;54:1166-76.

- [69] Lee K-J, Nam JH, Kim C-J. Steady saturation distribution in hydrophobic gas-diffusion layers of polymer electrolyte membrane fuel cells: a pore-network study. *Journal of Power Sources*. 2010;195:130-41.
- [70] Luo G, Ji Y, Wang C-Y, Sinha PK. Modeling liquid water transport in gas diffusion layers by topologically equivalent pore network. *Electrochimica Acta*. 2010;55:5332-41.
- [71] Sinha PK, Wang C-Y. Pore-network modeling of liquid water transport in gas diffusion layer of a polymer electrolyte fuel cell. *Electrochimica Acta*. 2007;52:7936-45.
- [72] Wu R, Zhu X, Liao Q, Wang H, Ding Y-d, Li J, et al. A pore network study on the role of micro-porous layer in control of liquid water distribution in gas diffusion layer. *international journal of hydrogen energy*. 2010;35:7588-93.
- [73] Wu R, Zhu X, Liao Q, Wang H, Ding Y-d, Li J, et al. A pore network study on water distribution in bi-layer gas diffusion media: effects of inlet boundary condition and micro-porous layer properties. *international journal of hydrogen energy*. 2010;35:9134-43.
- [74] Pauchet J, Prat M, Schott P, Kuttanikkad SP. Performance loss of proton exchange membrane fuel cell due to hydrophobicity loss in gas diffusion layer: Analysis by multiscale approach combining pore network and performance modelling. *international journal of hydrogen energy*. 2012;37:1628-41.
- [75] Inoue G, Yoshimoto T, Matsukuma Y, Minemoto M. Development of simulated gas diffusion layer of polymer electrolyte fuel cells and evaluation of its structure. *Journal of Power Sources*. 2008;175:145-58.
- [76] Hao L, Cheng P. Lattice Boltzmann simulations of water transport in gas diffusion layer of a polymer electrolyte membrane fuel cell. *Journal of Power Sources*. 2010;195:3870-81.
- [77] Park J, Matsubara M, Li X. Application of lattice Boltzmann method to a micro-scale flow simulation in the porous electrode of a PEM fuel cell. *Journal of Power Sources*. 2007;173:404-14.

- [78] Tabe Y, Lee Y, Chikahisa T, Kozakai M. Numerical simulation of liquid water and gas flow in a channel and a simplified gas diffusion layer model of polymer electrolyte membrane fuel cells using the lattice Boltzmann method. *Journal of Power Sources*. 2009;193:24-31.
- [79] Bazylak A. Liquid water visualization in PEM fuel cells: a review. *International journal of hydrogen energy*. 2009;34:3845-57.
- [80] Kang S. Dynamic modeling of proton exchange membrane fuel cell system for automotive application. Seoul National University. 2010.
- [81] Freunberger SA, Santis M, Schneider IA, Wokaun A, Büchi FN. In-plane effects in large-scale PEMFCs model formulation and validation. *Journal of The Electrochemical Society*. 2006;153:A396-A405.
- [82] Mueller F, Brouwer J, Kang S, Kim H-S, Min K. Quasi-three dimensional dynamic model of a proton exchange membrane fuel cell for system and controls development. *Journal of power sources*. 2007;163:814-29.
- [83] Kang S, Min K, Mueller F, Brouwer J. Configuration effects of air, fuel, and coolant inlets on the performance of a proton exchange membrane fuel cell for automotive applications. *International Journal of Hydrogen Energy*. 2009;34:6749-64.
- [84] Bruggeman VD. Berechnung verschiedener physikalischer Konstanten von heterogenen Substanzen. I. Dielektrizitätskonstanten und Leitfähigkeiten der Mischkörper aus isotropen Substanzen. *Annalen der physik*. 1935;416:636-64.
- [85] Dutta S, Shimpalee S, Van Zee J. Numerical prediction of mass-exchange between cathode and anode channels in a PEM fuel cell. *International Journal of Heat and Mass Transfer*. 2001;44:2029-42.
- [86] Wang Y. Modeling of two-phase transport in the diffusion media of polymer electrolyte fuel cells. *Journal of Power Sources*. 2008;185:261-71.
- [87] Pasaogullari U, Wang C-Y. Two-phase transport and the role of micro-porous layer in polymer electrolyte fuel cells. *Electrochimica Acta*. 2004;49:4359-69.

- [88] Bernardi DM, Verbrugge MW. A Mathematical Model of the Solid-Polymer-Electrolyte Fuel Cell. *Journal of the Electrochemical Society*. 1992;139:2477-91.
- [89] White FM. *Fluid Mechanics*,(2003). McGraw-Hill.
- [90] Nam JH, Kaviany M. Effective diffusivity and water-saturation distribution in single-and two-layer PEMFC diffusion medium. *International Journal of Heat and Mass Transfer*. 2003;46:4595-611.
- [91] Zhou P, Wu C. Numerical study on the compression effect of gas diffusion layer on PEMFC performance. *Journal of Power Sources*. 2007;170:93-100.
- [92] Kitahara T, Konomi T, Nakajima H. Microporous layer coated gas diffusion layers for enhanced performance of polymer electrolyte fuel cells. *Journal of Power Sources*. 2010;195:2202-11.
- [93] Bear J, Bachmat Y. *Introduction to modeling of transport phenomena in porous media*: Springer; 1990.
- [94] Gurau V, Bluemle MJ, De Castro ES, Tsou Y-M, Mann Jr JA, Zawodzinski Jr TA. Characterization of transport properties in gas diffusion layers for proton exchange membrane fuel cells: 1. Wettability (internal contact angle to water and surface energy of GDL fibers). *Journal of Power Sources*. 2006;160:1156-62.
- [95] Cho J, Kim H-S, Min K. Transient response of a unit proton-exchange membrane fuel cell under various operating conditions. *Journal of Power Sources*. 2008;185:118-28.
- [96] Liu Z, Mao Z, Wu B, Wang L, Schmidt VM. Current density distribution in PEFC. *Journal of Power Sources*. 2005;141:205-10.
- [97] Cleghorn S, Derouin C, Wilson M, Gottesfeld S. A printed circuit board approach to measuring current distribution in a fuel cell. *Journal of Applied Electrochemistry*. 1998;28:663-72.
- [98] Dutta S, Shimpalee S, Van Zee J. Three-dimensional numerical simulation of straight channel PEM fuel cells. *Journal of Applied Electrochemistry*. 2000;30:135-46.

- [99] Mench M, Wang C, Ishikawa M. In situ current distribution measurements in polymer electrolyte fuel cells. *Journal of the Electrochemical Society*. 2003;150:A1052-A9.
- [100] Hartnig C, Manke I, Kardjilov N, Hilger A, Grünerbel M, Kaczerowski J, et al. Combined neutron radiography and locally resolved current density measurements of operating PEM fuel cells. *Journal of Power Sources*. 2008;176:452-9.
- [101] Li X, Sabir I. Review of bipolar plates in PEM fuel cells: Flow-field designs. *International Journal of Hydrogen Energy*. 2005;30:359-71.
- [102] Owejan JP, Gagliardo JJ, Sergi JM, Kandlikar SG, Trabold TA. Water management studies in PEM fuel cells, Part I: Fuel cell design and in situ water distributions. *International Journal of Hydrogen Energy*. 2009;34:3436-44.
- [103] Lu Z, Kandlikar S, Rath C, Grimm M, Domigan W, White A, et al. Water management studies in PEM fuel cells, Part II: Ex situ investigation of flow maldistribution, pressure drop and two-phase flow pattern in gas channels. *International Journal of Hydrogen Energy*. 2009;34:3445-56.

국문 초록

기체확산층 (Gas diffusion layer, GDL) 은 고분자 전해질형 연료전지 (Polymer electrolyte membrane fuel cell, PEM fuel cell) 에서 수소와 공기 그리고 물의 이동통로로서의 역할을 하기 때문에 매우 중요한 부분을 차지한다. 이렇게 기체확산층이 연료전지 내부의 물질전달을 결정하는 요소이기 때문에, 연료전지 성능을 향상시키기 위해서 물 관리 능력에 최적화된 기체확산층의 구조적 설계에 대한 연구가 필요하다. 그동안 기체확산층의 구조적 특성을 이해하기 위한 많은 실험적 그리고 계산적 연구들이 시도되었지만 이전 연구 결과들은 GDL 의 구조적 특성이 연료전지 성능에 미치는 영향에 대한 직접적인 분석을 수행하지 못하였다. 따라서 본 연구에서는 기체확산층의 구조적 특성을 반영할 수 있는 모델을 설계하고, 다양한 기체확산층 구조적 특성이 물 관리와 연료전지 성능에 미치는 영향에 대해 분석하고 검증하였다.

첫째로, 기체확산층의 구조적 특성을 반영할 수 있는 MATLAB[®]/Simulink[®] 기반의 준 3 차원의 연료전지 모델을 개발하였다. 개발된 모델의 특징은 간단하면서도 연료전지 내의 국부적 특성을 살펴 볼 수 있다는 점이다. 기체확산층의 구조적 특성을 이해하기 위해 기체확산층의 검사체적은 9개로 나뉘어져 이상유동을 고려하였고, 따라서 기체확산층 내의 이상수송에 대한 예측 및 그에 따른 물 관리 능력과 연료전지 성능에 미치는 영향에 대한 분석을 수행 할 수 있었다.

두 번째로, 기체확산층의 기재 (substrate) 에서의 공극 크기의 변화가 물 관리 능력과 연료전지 성능에 미치는 영향에 대해 분석하였다. 구조적 특성을 이해하기 위해 서로 다른 공극 크기를 갖는 기체확산층을 제작하여 공극률, 공극 크기, 두께, 내부 접촉각을 측정하여 해당 기체확산층을 평가하였다. 또한 측정된 결과를 개발된 모델에 반영하여

기체확산층 내의 물질전달 현상에 대한 분석을 수행하였다. 그 결과 기재 내부의 상대적으로 큰 공극은 미세다공층 (Micro porous layer, MPL) 과 미세다공층 침투층 (MPL penetration) 을 성글게 형성시키며 반대로 상대적으로 작은 공극은 밀집하게 형성시킨다는 사실을 밝혀내었다. 이에 따라서 서로 다른 공극 크기를 갖는 기체확산층은 각각 물을 잘 배출할 수 있는 특성과 물을 잘 함유할 수 있는 특성을 가지고 이러한 특성이 상대습도나 전류 부하에 따른 연료전지 성능에 영향을 미친다는 사실을 밝혀내었다.

세 번째로, 기체확산층의 평면 방향으로의 구조적 특성에 대한 분석을 수행하였다. 평면 방향으로의 구조적 설계는 기본적으로 물 배출과 물 함유 능력을 갖는 두 가지 기체확산층을 조합하여 이루어졌다. 총 네 가지의 기체확산층 조합을 설계하여 모델을 통해 효과를 예측한 결과, 조합된 기체확산층들은 서로 다른 국부적인 물 관리 능력을 갖고 그에 따라 물질전달의 특성 또한 달라지는 것을 확인하였다. 시뮬레이션을 통해 예측한 결과를 바탕으로 도출된 물 관리 능력에 특화된 한 가지 기체확산층 조합을 실험한 결과, 균일한 물질전달 및 전류밀도 분포를 바탕으로 연료전지 성능이 향상되었으며 전압의 안정성 또한 향상되는 것을 확인하였다.

마지막으로 기체확산층의 두께 방향으로의 구조적 특성에 대한 분석을 수행하였다. 미세다공층으로부터 전달된 액상의 물은 기재의 평균적인 모세관압 구배를 통해 채널까지 도달하게 된다. 이 때 기재 내에서 물을 효과적으로 배출하기 위해서는 모세관압 구배를 MPL 침투층으로부터 채널까지 지속적으로 증가시켜야 한다. 따라서 기재 내에서 연속적으로 증가하는 기공 크기를 갖는 기체확산층을 설계하고 시뮬레이션 한 결과, 기재 내에서 물 관리 능력이 향상되는 것을 확인하였다. 이를 바탕으로 실제 기공 크기 구배 구조를 갖는

기체확산층을 제작하고 실험적으로 검증한 결과, 특히 고전밀도 구간에서 물질전달 능력이 향상되어 연료전지 성능이 향상되는 것을 밝혀내었다.

본 연구에서는 실험적 연구와 시뮬레이션 연구를 동시에 진행함으로써, 기체확산층의 구조적 특성과 그에 따른 연료전지 내의 물 관리 능력 및 연료전지 성능에 미치는 영향에 대해 분석하였다. 본 연구는 기체확산층의 구조적 특성에 대한 평가 및 분석, 향상된 물 관리 능력을 갖는 기체확산층의 최적 설계, 그리고 운전조건에 따른 제어 전략을 수립하는데 도움이 될 것이다.

주요어 : 고분자 전해질형 연료전지 (PEM Fuel Cell), 기체확산층 (GDL), 시뮬레이션, 물 관리, 액상수 포화, 구조적 특성

학번 : 2009-20682